สมบัติเชิงเคมีไฟฟ้าของ $LnSr_{3-x}Ca_xFe_{3-y}B_yO_{10}$ (Ln = La, Pr และ Sm; x = 0-1.0; B = Co, Ni และ Cu; y = 0-1.5) สำหรับเซลล์เชื้อเพลิงออกไซด์ของแข็งที่อุณหภูมิปานกลาง

นางสาวณิชารีย์ วงศ์สวัสดิ์กุล

วิทยานิพนธ์นี้เป็นส่วนหนึ่งของการศึกษาตามหลักสูตรปริญญาวิทยาศาสตรดุษฎีบัณฑิต
สาขาวิชาปิโตรเคมี
คณะวิทยาศาสตร์ จุฬาลงกรณ์มหาวิทยาลัย
ปีการศึกษา 2560

ELECTROCHEMICAL PROPERTIES OF $LnSr_{3-x}Ca_xFe_{3-y}B_yO_{10}$ (Ln = La, Pr AND Sm; x = 0-1.0; B = Co, Ni AND Cu; y = 0-1.5) FOR INTERMEDIATE TEMPERATURE SOLID OXIDE FUEL CELLS

Miss Nicharee Wongsawatgul

A Dissertation Submitted in Partial Fulfillment of the Requirements
for the Degree of Doctor of Philosophy Program in Petrochemistry
Faculty of Science
Chulalongkorn University
Academic Year 2017

Thesis Title	ELECTROCHEMICAL PROPERTIES OF $LnSr_{3-x}Ca_xFe_{3-y}B_yO_{10}$ (Ln = La, Pr AND Sm; x = 0-1.0; B = Co, Ni AND Cu; y = 0- 1. 5) FOR INTERMEDIATE TEMPERATURE SOLID OXIDE FUEL CELLS
By	Miss Nicharee Wongsawatgul
Field of Study	Petrochemistry
Thesis Advisor	Assistant Professor Soamwadee Chaiananansutcharit, Ph.D.
Thesis Co-Advisor	Professor Kazunori Sato, Ph.D.

Accepted by the Faculty of Science, Chulalongkorn University in Partial Fulfillment of the Requirements for the Doctoral Degree

.....Dean of the Faculty of Science

(Professor Polkit Sangvanich, Ph.D.)

THESIS COMMITTEE

.....Chairman

(Assistant Professor Warinthorn Chavasiri, Ph.D.)

.....Thesis Advisor

(Assistant Professor Soamwadee Chaiananansutcharit, Ph.D.)

.....Thesis Co-Advisor

(Professor Kazunori Sato, Ph.D.)

.....Examiner

(Associate Professor Rojana Pornprasertsuk, Ph.D.)

.....Examiner

(Assistant Professor Varawut Tangpasuthadol, Ph.D.)

.....External Examiner

(Assistant Professor Jinda Yeyongchaiwat, Ph.D.)

ณิชารีย์ วงศ์สวัสดิ์กุล : สมบัติเชิงเคมีไฟฟ้าของ $LnSr_{3-x}Ca_xFe_{3-y}B_yO_{10}$ (Ln = La, Pr และ Sm; x = 0-1.0; B = Co, Ni และ Cu; y = 0-1.5) สำหรับเซลล์เชื้อเพลิงออกไซด์ของแข็งที่อุณหภูมิปานกลาง (ELECTROCHEMICAL PROPERTIES OF $LnSr_{3-x}Ca_xFe_{3-y}B_yO_{10}$ (Ln = La, Pr AND Sm; x = 0-1.0; B = Co, Ni AND Cu; y = 0-1.5) FOR INTERMEDIATE TEMPERATURE SOLID OXIDE FUEL CELLS) อ.ที่ปรึกษาวิทยานิพนธ์หลัก: ผศ. ดร.โสมวดี ไชยอนันต์สุจริต, อ.ที่ปรึกษาวิทยานิพนธ์ร่วม: ศ. ดร.คาสึโนริ ซาโต้, หน้า.

ศึกษาประสิทธิภาพเชิงไฟฟ้าเคมีของขั้วแคโทดในเซลล์เชื้อเพลิงออกไซด์ของแข็งที่อุณหภูมิปานกลาง จาก $LnSr_{3-x}Ca_xFe_{3-y}B_yO_{10}$ (Ln = La, Pr and Sm; x = 0-1.0; B = Ni, Co, and Cu; y = 0-1.5) ที่มีโครงสร้างเฟส Ruddlesden-Popper (R-P) ซึ่งเตรียมได้จากวิธีเผาไหม้ซิตริกไนเตรต ในช่วงแรกทำการศึกษาผลการเติม Ca ที่ความเข้มข้นต่างๆ ลงในโครงสร้าง $LaSr_{3-x}Ca_xFe_3O_{10-\delta}$ พบว่าวัสดุที่มีความเข้มข้นของ Ca ต่ำให้ค่าความต้านทานเฉพาะของเซลล์ต่อพื้นที่ต่ำลงและให้ประสิทธิภาพทางเคมีไฟฟ้าของเซลล์ที่ดีขึ้น ซึ่งเป็นผลมาจากความสามารถในการนำไฟฟ้าที่เพิ่มขึ้นและค่าสัมประสิทธ์การขยายตัวทางความร้อนที่ลดลง หลังจากนั้นได้ศึกษาผลของการแทนที่ La ด้วย Pr และ Sm พบว่าวัสดุที่แทนที่ด้วย Pr มีประสิทธิภาพทางเคมีไฟฟ้าของเซลล์ที่เพิ่มขึ้นและให้ค่าความต้านทานเฉพาะต่อพื้นที่ที่ลดต่ำลง เนื่องมาจากออกซิเจนไอออนสามารถเคลื่อนที่ผ่านช่องว่างออกซิเจนได้มากขึ้น ร่วมกับการเกิดปฏิกิริยารีดักชันของเหล็ก ในส่วนที่สามศึกษาการแทนที่ของ Ni, Co, และ Cu ที่ตำแหน่ง Fe พบว่าประสิทธิภาพทางไฟฟ้าเคมีของเซลล์ของวัสดุที่แทนที่ด้วยการเติม Co และ Cu มีค่าเพิ่มขึ้น และมีค่าความต้านทานต่อพื้นที่ลดลง ทั้งนี้เนื่องมาจากค่าการนำไฟฟ้าและความสามารถในการเคลื่อนที่ของออกไซด์ไอออนที่เพิ่มมากขึ้น และส่วนสุดท้ายเป็นการศึกษาผลจากปริมาณ Co ที่เติมใน $PrSr_{2.7}Ca_{0.3}Fe_{3-y}Co_yO_{10-\delta}$ พบว่าเมื่อเพิ่มความเข้มข้นของ Co ประสิทธิภาพทางไฟฟ้าเคมีของเซลล์มีค่าลดลง พร้อมทั้งค่าความต้านทานเฉพาะต่อพื้นที่มีค่าสูงขึ้น ซึ่งเป็นผลจากการเคลื่อนที่ของออกซิเจนที่ลดลงและค่าสัมประสิทธิ์การขยายตัวทางความร้อนที่เพิ่มสูงขึ้นอย่างมาก ดังนั้นในงานวิจัยครั้งนี้พบว่า $PrSr_{2.7}Ca_{0.3}Fe_{2.5}Co_{0.5}O_{10-\delta}$ ที่ใช้เป็นแคโทดในเซลล์เดี่ยวแสดงประสิทธิภาพทางไฟฟ้าเคมีในเซลล์เชื้อเพลิงออกไซด์ของแข็งที่อุณหภูมิปานกลางได้สูงที่สุด โดยให้กำลังไฟฟ้าต่อหน่วยที่ 481 $mW \cdot cm^{-2}$ และให้ความต้านทานเฉพาะต่อพื้นที่ที่ 1.18 $\Omega\ cm^2$

สาขาวิชา ปิโตรเคมี	ลายมือชื่อนิสิต .....
ปีการศึกษา 2560	ลายมือชื่อ อ.ที่ปรึกษาหลัก .....
	ลายมือชื่อ อ.ที่ปรึกษาร่วม .....

5572874923 : MAJOR PETROCHEMISTRY
KEYWORDS: SOFC / CATHODE MATERIAL / RUDDLESDEN POPPER / ELECTROCHEMICAL

NICHAREE WONGSAWATGUL: ELECTROCHEMICAL PROPERTIES OF $LnSr_{3-x}Ca_xFe_{3-y}B_yO_{10}$ (Ln = La, Pr AND Sm; x = 0-1.0; B = Co, Ni AND Cu; y = 0-1.5) FOR INTERMEDIATE TEMPERATURE SOLID OXIDE FUEL CELLS. ADVISOR: ASST. PROF. SOAMWADEE CHAIANANSUTCHARIT, Ph. D. , CO- ADVISOR: PROF. KAZUNORI SATO, Ph.D., pp.

To enhance the electrochemical performance of cathode material for intermediate temperature solid oxide fuel cell (IT-SOFC) the Ruddlesden-Popper (RP) phases of $LnSr_{3-x}Ca_xFe_{3-y}B_yO_{10}$ (Ln = La, Pr and Sm; x = 0-1.0; B = Ni, Co, and Cu; y = 0-1.5) was investigated and prepared by citric nitrate combustion method. Firstly, various Ca concentrations were added to the $LaSr_{3-x}Ca_xFe_3O_{10-\delta}$ structure and it was found that the materials contained low Ca concentration provided the lower area specific resistance (ASR) and better electrochemical cell performance due to the enhance in conductivity and reduction of TEC. Secondly, the effect of Pr and Sm replacement for La in $LaSr_{2.7}Ca_{0.3}Fe_3O_{10-\delta}$ was evaluated. The electrochemical cell performance of Pr substituted materials was promoted with the reduction of ASR due to the increase of oxygen migration through the oxygen vacancy and the reduction of Fe. Thirdly, the substitution of Ni, Co and Cu for Fe in $PrSr_{2.7}Ca_{0.3}Fe_{2.5}B_{0.5}O_{10-\delta}$ was studied. The electrochemical performance of Co and Cu substituted materials was enhanced while the ASR was reduced because the conductivity and oxygen diffusivity were increased. Lastly, the effect of Co concentration in $PrSr_{2.7}Ca_{0.3}Fe_{3-y}Co_yO_{10-\delta}$ was evaluated. The increased Co concentration decreased the electrochemical performance with increasing of ASR due to the lowering oxygen mobility, and the TEC was significantly increased. Thus, among the oxides examined in this work, $PrSr_{2.7}Ca_{0.3}Fe_{2.5}Co_{0.5}O_{10-\delta}$ cathode showed the best electrochemical performance of single cell IT-SOFC with the maximum power density of 481 $mW.cm^{-2}$ and the lowest ASR of 1.18 Ω cm^2.

Field of Study: Petrochemistry
Academic Year: 2017

Student's Signature .....
Advisor's Signature .....
Co-Advisor's Signature .....

ACKNOWLEDGEMENTS

First of all, I would like to explicit my profound gratitude to my advisor, Assistance Professor Soamwadee Chaiananansucharit, for giving me the benevolent support, advice, guidance for my research work and great opportunity to study in Japan; for her sympathy and tolerance and for having encouraged me to keep going. I would also express my sincere thanks to my co-advisor, Professor Kazunori Sato, for his unlimited willingness to help, listen, and give me a great deal of advice in scientific and most of all social matters. I would also like to thank my committee members Associate Professor Rojana Pornprasertsuk, Assistant Professor Varawut Tangpasuthadol, and Assistant Professor Jinda Yenyongchaiwat, for their valuable time and thoughtful insight. I wish to thank past and present SOFC laboratory members for their humor and kindness, for his help and for all the interesting discussions we had.

Yet, most of all, I want to thank my parents and sister for their spiritual and financial support, which ensure I can finish my study here.

CONTENTS

Page

THAI ABSTRACT iv

ENGLISH ABSTRACT v

ACKNOWLEDGEMENTS vi

CONTENTS vii

LIST OF FIGURES 1

LIST OF TABLES 1

CHAPTER I INTRODUCTION 1

CHAPTER II BACKGROUND AND THEORY 4

2.1 Fuel cells 4

2.2 Classification of fuel cells 5

2.3 Solid oxide fuel cells (SOFCs) 7

2.3.1 Definition and principle 7

2.3.2 Electrochemical performance of SOFC 9

2.3.3 SOFC materials 10

2.3.3.1 Electrolyte requirement 11

2.3.3.2 Anode requirement 13

2.3.3.3 Cathode requirement 14

2.3.3.4 Cathode review 14

CHAPTER III EXPERIMENTAL 22

3.1 Material preparation 22

3.1.1 Chemicals and reagents 22

3.1.2 Sample preparation 22

Page

3.1.2.1 Cathode preparation 22

3.1.2.2 Electrolyte preparation 24

3.1.2.3 Anode preparation 24

3.2 Physical properties characterization 24

3.2.1 Structural characterization 24

3.2.2 Microstructure characterization 25

3.2.3 Thermogravimetric analysis 25

3.2.4 Thermal expansion measurement 25

3.3 Single cell fabrication and fuel cell set-up consideration 26

3.4 Electrochemical properties 29

3.4.1 Total conductivity 29

3.4.2 Electrochemical performance 30

3.4.3 Electrode resistance characterization 30

CHAPTER IV RESULT AND DISCUSSION 32

4.1 Effect of Ca substitution for Sr in $LaSr_{3-x}Ca_xFe_3O_{10-\delta}$ Ruddlesden-Popper phase 32

4.1.1 Crystal structure and phase identification of $LaSr_{3-x}Ca_xFe_3O_{10-\delta}$ 32

4.1.2 TG analysis of $LaSr_{3-x}Ca_xFe_3O_{10-\delta}$ 37

4.1.3 Total conductivity of $LaSr_{3-x}Ca_xFe_3O_{10-\delta}$ 39

4.1.4 Microstructure of $LaSr_{3-x}Ca_xFe_3O_{10-\delta}$ 40

4.1.5 Thermal expansion behavior of $LaSr_{3-x}Ca_xFe_3O_{10-\delta}$ 42

4.1.6 X–ray Photoelectron Spectroscopy (XPS) of $LaSr_{3-x}Ca_xFe_3O_{10-\delta}$ 44

4.1.6.1 Calcium spectra in $LaSr_{3-x}Ca_xFe_3O_{10-\delta}$ 44

Page

4.1.6.2 Iron spectra in $LaSr_{3-x}Ca_xFe_3O_{10-\delta}$ 45

4.1.7 Electrochemical performance of $LaSr_{3-x}Ca_xFe_3O_{10-\delta}$ 47

4.1.7.1 Single cell performance for $LaSr_{3-x}Ca_xFe_3O_{10-\delta}$ cathode 47

4.1.7.2 Resistance of the single cells for $LaSr_{3-x}Ca_xFe_3O_{10-\delta}$ cathode 51

4.2 Effect of lanthanide ion in $LnSr_{2.7}Ca_{0.3}Fe_3O_{10-\delta}$ (Ln = La, Pr, and Sm) Ruddlesden-Popper phases as Cathodes for Intermediate Temperature Solid Oxide Fuel Cells 55

4.2.1 Crystal structure and phase identification of $LnSr_{2.7}Ca_{0.3}Fe_3O_{10-\delta}$ 55

4.2.2 TG analysis of $LnSr_{2.7}Ca_{0.3}Fe_3O_{10-\delta}$ 59

4.2.3 Thermal expansion behavior of $LnSr_{2.7}Ca_{0.3}Fe_3O_{10-\delta}$ 61

4.2.4 Total conductivity of $LnSr_{2.7}Ca_{0.3}Fe_3O_{10-\delta}$ 63

4.2.5 Microstructure of $LnSr_{3-x}Ca_xFe_3O_{10-\delta}$ 65

4.2.6 X-ray Photoelectron Spectroscopy (XPS) 66

4.2.6.1 Lanthanum spectra for $LaSr_{2.7}Ca_{0.3}Fe_3O_{10-\delta}$ 66

4.2.6.2 Praseodymium spectra for $PrSr_{2.7}Ca_{0.3}Fe_3O_{10-\delta}$ 67

4.2.6.3 Samarium spectra for $SmSr_{2.7}Ca_{0.3}Fe_3O_{10-\delta}$ 69

4.2.6.4 Iron spectra of $LnSr_{2.7}Ca_{0.3}Fe_3O_{10-\delta}$ 70

4.2.7 Electrochemical performance of $LnSr_{2.7}Ca_{0.3}Fe_3O_{10-\delta}$ 72

4.2.7.1 Single cell performance for $LnSr_{2.7}Ca_{0.3}Fe_3O_{10-\delta}$ cathodes 72

4.2.7.2 Resistance of the single cells for $LnSr_{2.7}Ca_{0.3}Fe_3O_{10-\delta}$ cathodes 74

4.3 Effect of transition metal in $PrSr_{2.7}Ca_{0.3}Fe_{2.5}B_{0.5}O_{10-\delta}$ (B = Fe, Ni, Co, and Cu) Ruddlesden-Popper phases as Cathodes for Intermediate Temperature Solid Oxide Fuel Cells 77

Page

4.3.1 Crystal structure and phase identification of $PrSr_{2.7}Ca_{0.3}Fe_{2.5}B_{0.5}O_{10-\delta}$ 77

4.3.2 TG analysis of $PrSr_{2.7}Ca_{0.3}Fe_{2.5}B_{0.5}O_{10-\delta}$ 81

4.3.3 Thermal expansion behavior $PrSr_{2.7}Ca_{0.3}Fe_{2.5}B_{0.5}O_{10-\delta}$ 83

4.3.4 Total conductivity characterization of $PrSr_{2.7}Ca_{0.3}Fe_{2.5}B_{0.5}O_{10-\delta}$ 85

4.3.5 Microstructure of $PrSr_{2.7}Ca_{0.3}Fe_{2.5}B_{0.5}O_{10-\delta}$ (B = Fe, Co and Cu) 86

4.3.6 Electrochemical performance of $PrSr_{2.7}Ca_{0.3}Fe_{2.5}B_{0.5}O_{10-\delta}$ 87

4.3.6.1 Single cell performance for $PrSr_{2.7}Ca_{0.3}Fe_{2.5}B_{0.5}O_{10-\delta}$ cathodes 87

4.3.6.2 Resistance of the single cells 89

4.4 Effect of Co concentration in $PrSr_{2.7}Ca_{0.3}Fe_{3-y}Co_yO_{10-\delta}$ (y = 0.5-1.5) Ruddlesden-Popper phases as Cathodes for Intermediate Temperature Solid Oxide Fuel Cells 91

4.4.1 Crystal structure and phase identification of $PrSr_{2.7}Ca_{0.3}Fe_{3-y}Co_yO_{10-\delta}$ 91

4.4.2 TG analysis $PrSr_{2.7}Ca_{0.3}Fe_{3-y}Co_yO_{10-\delta}$ 94

4.4.3 Thermal expansion behavior $PrSr_{2.7}Ca_{0.3}Fe_{3-y}Co_yO_{10-\delta}$ 95

4.4.4 Total conductivity characterization of $PrSr_{2.7}Ca_{0.3}Fe_{3-y}Co_yO_{10-\delta}$ 97

4.4.5 Microstructure of $PrSr_{2.7}Ca_{0.3}Fe_{3-y}Co_yO_{10-\delta}$ (y = 0.5, and 1.0) 99

4.4.6 Electrochemical performance of $PrSr_{2.7}Ca_{0.3}Fe_{3-y}Co_yO_{10-\delta}$ 100

4.4.6.1 Single cell performance for $PrSr_{2.7}Ca_{0.3}Fe_{3-y}Co_yO_{10-\delta}$ cathodes 100

4.4.6.2 Resistance of the single cells for $PrSr_{2.7}Ca_{0.3}Fe_{3-y}Co_yO_{10-\delta}$ cathodes 102

CHAPTER V CONCLUSION 1

..... 4

REFERENCES 4

APPENDIX 21

Page

VITA..... 25

LIST OF FIGURES

Figure 1-1 World consumption of primary energy by a source in 2015 2

Figure 2-1 Schematic of a solid oxide fuel cell 8

Figure 2-2 Schematic diagram of the triple-phase boundary (TPB) on the cathode..... 8

Figure 2-3 Current-voltage (I-V) curve of a fuel cell and the polarization loss. 10

Figure 2-4 Electrical conductivity of various electrolytes depending on temperature 12

Figure 2-5 Crystal structures of Ruddlesden–Popper phase (a) n=1, (b) n=2 and (c) n=3 16

Figure 2-6 (a) The perovskite structure (ABO_3) , (b) Covalent bonds between anionic p-orbital and d-orbital of *B*-site cation 17

Figure 3-1 A schematic configuration of a single cell27

Figure 3-2 Schematic configuration of the single cell test set-up..... 27

Figure 3-3 SOFC setting schematic..... 28

Figure 3-4 Schematic illustration of the DC four – point probe experiment. 29

Figure 3-5. Cell equivalent circuit 31

Figure 4-1 XRD pattern of $LaSr_{3-x}Ca_xFe_3O_{10-\delta}$ after sintered at 1400°C for 12 h and annealed at 900°C for 30 min with (▼ = $LaSr_{3-x}Ca_xFe_3O_{9.9}$, and **x** = $(La,Sr)FeO_3$; (a) x = 0, (b) x = 0.1, (c) x = 0.3, (d) x = 0.5, (e) x = 0.7, (f) x = 1.0 and (g) x = 1.5 35

Figure 4-2 (a) Lattice parameter a, (b) and lattice parameters c, and (c) unit cell volume of the $LaSr_{3-x}Ca_xFe_3O_{10-\delta}$ (x = 0-1.0) 36

Figure 4-3 TGA plots of $LaSr_{3-x}Ca_xFe_3O_{10-\delta}$ (x = 0-0.7) measured in air at 25-800 °C. .. 38

Figure 4-4 The total conductivity of $LaSr_{3-x}Ca_xFe_3O_{10-\delta}$ (x = 0-0.7) at 200-800 °C in air 40

Figure 4-5 SEM images of crossed section of $LaSr_{3-x}Ca_xFe_3O_{10-\delta}$: (a) x = 0, (b) x = 0.1, (c) x = 0.3, (d) x = 0.5, and (e) x = 0.7 42

Figure 4-6 Thermal expansion ($\Delta L/L_o$) curves of $LaSr_{3-x}Ca_xFe_3O_{10-\delta}$ (x = 0-0.7) in air at 25-800 °C 43

Figure 4-7 XPS spectra of Ca 2p core – level of $LaSr_{3-x}Ca_xFe_3O_{10-\delta}$ (x = 0, 0.3 and 0.5) 44

Figure 4-8 XPS spectra of Fe 2p core – level spectra in $LaSr_{3-x}Ca_xFe_3O_{10-\delta}$ (x = 0, 0.3 and 0.5). 46

Figure 4-9 (a) Terminal voltage and (b) power densities as a function of current density of the $LaSr_{3-x}Ca_xFe_3O_{10-\delta}$ (x = 0-0.7) cathodes at 800 °C. 49

Figure 4-10 Terminal voltage (open symbols) and power densities (closed symbols) as a function of current density of the $LaSr_{2.7}Ca_{0.3}Fe_3O_{10-\delta}$ cathodes at 600-800 °C. 50

Figure 4-11 Impedance spectra of the $LaSr_{3-x}Ca_xFe_3O_{10-\delta}$ (x = 0-0.7) cathodes at 800 °C. 53

Figure 4-12 Impedance spectra of the cell for $LaSr_{2.7}Ca_{0.3}Fe_3O_{10-\delta}$ (x = 0-0.7) cathodes at 600-800 °C. 54

Figure 4-13 XRD pattern of the various $LnSr_{2.7}Ca_{0.3}Fe_3O_{10-\delta}$ after sintered at 1400°C for 12 h and annealed at 900°C for 30 min with (▼ = $LaSr_{3-x}Ca_xFe_3O_{9.9}$, **x** = $SrFeO_3$, and ○ = $(Ln,Sr)FeO_4$); (a) Ln = La, (b) Ln = Pr and (c) Ln = Sm 57

Figure 4-14 (a) Lattice parameter a, (b) and lattice parameters c, and (c) unit cell volume of the $LnSr_{2.7}Ca_{0.3}Fe_3O_{10-\delta}$ (Ln = La, Pr, and Sm) 58

Figure 4-15 TGA plots of the $LnSr_{2.7}Ca_{0.3}Fe_3O_{10-\delta}$ (Ln = La, Pr, and Sm) measured in air at 25-800 °C. 60

Figure 4-16 Thermal expansion ($\Delta L/L_o$) curves of $LnSr_{2.7}Ca_{0.3}Fe_3O_{10-\delta}$ (Ln = La, Pr, and Sm) in air in a temperature range of 25-800 °C compared to LSGM electrolyte 62

Figure 4-17 The total conductivity of $LnSr_{2.7}Ca_{0.3}Fe_3O_{10-\delta}$ (Ln = La, Pr, and Sm) at 200-800 °C in air 64

Figure 4-18 SEM images of crossed section of the $LnSr_{2.7}Ca_{0.3}Fe_3O_{10-\delta}$ samples: (a) Ln = La, (b) Ln = Pr, and (c) Ln = Sm 65

Figure 4-19 XPS spectra of La 3*d* core–level of $LaSr_{2.7}Ca_{0.3}Fe_3O_{10-\delta}$ 66

Figure 4-20 XPS spectra of Pr 3*d* core – level of $PrSr_{2.7}Ca_{0.3}Fe_3O_{10-\delta}$ 67

Figure 4-21 XPS spectra of Sm 3*d* core – level of $SmSr_{2.7}Ca_{0.3}Fe_3O_{10-\delta}$ 69

Figure 4-22 XPS spectra of Fe 2p core – level spectra in $LnSr_{2.7}Ca_{0.3}Fe_3O_{10-\delta}$ (Ln = La, Pr, and Sm) 71

Figure 4-23. (a) Terminal voltage and (b) power densities as a function of current density of the $LnSr_{2.7}Ca_{0.3}Fe_3O_{10-\delta}$ (Ln = La, Pr, and Sm) cathodes at 800 °C. 73

Figure 4-24 ASR of the $LnSr_{2.7}Ca_{0.3}Fe_3O_{10-\delta}$ (Ln = La, Pr, and Sm) cathodes at 800 °C. 76

Figure 4-25 XRD pattern of the various $PrSr_{2.7}Ca_{0.3}Fe_{2.5}B_{0.5}O_{10-\delta}$ (B = Fe, Ni, Co, and Cu) after annealed at 900°C for 30 min with (▼ = $LnSr_3Fe_3O_{10-\delta}$, × = $(Ln,Sr)FeO_3$, ○ = $(Ln,Sr)FeO_4$, and ? = unknown); (a) B = Fe, (b) B = Co, (c) B = Cu, and (d) B = Ni 80

Figure 4-26 TGA plots of the $PrSr_{2.7}Ca_{0.3}Fe_{2.5}B_{0.5}O_{10-\delta}$ (B = Fe, Co, and Cu) samples measured in air at the temperature range of 25-800 °C. 82

Figure 4-27 Thermal expansion ($\Delta L/L_o$) curves of $PrSr_{2.7}Ca_{0.3}Fe_{2.5}B_{0.5}O_{10-\delta}$ (B = Fe, Co, and Cu) in air at a temperature range of 25-800 °C compared to LSGM electrolyte .. 84

Figure 4-28 The total conductivity of $PrSr_{2.7}Ca_{0.3}Fe_{2.5}B_{0.5}O_{10-\delta}$ (B = Fe, Co and Cu) at 200-800 °C in air 85

Figure 4-29 SEM images of crossed section of the $PrSr_{2.7}Ca_{0.3}Fe_{2.5}B_{0.5}O_{10-\delta}$: (a) B = Fe, (b) B = Cu, and (c) B= Co 86

Figure 4-30 (a) Terminal voltage and (b) power densities as a function of current density of the cell for $PrSr_{2.7}Ca_{0.3}Fe_{2.5}B_{0.5}O_{10-\delta}$ (B = Fe, Co, and Cu) cathodes at 800 °C. 88

Figure 4-31 ASR of the cell for $PrSr_{2.7}Ca_{0.3}Fe_{2.5}B_{0.5}O_{10-\delta}$ (B = Fe, Co and Cu) cathodes at 800 °C 90

Figure 4-32 XRD pattern of $PrSr_{2.7}Ca_{0.3}Fe_{3-y}Co_yO_{10-\delta}$ (y = 0.5-1.5) after annealed at 900°C for 30 min with (▼ = $PrSr_{2.7}Ca_{0.3}Fe_{3-y}Co_yO_{10-\delta}$, **x** = perovskite, ○ = $(Pr,Sr,Ca)_2(Fe,Co)O_4$, □ = $(Pr,Sr,Ca)_3(Fe,Co)_2O_7$, Δ = Fe_3O_4, ■ = SrO, and **?** = unknown); (a) y = 0.5, (b) y = 1.0, and (c) y =1.5. 93

Figure 4-33 TGA plots of the $PrSr_{2.7}Ca_{0.3}Fe_{3-y}Co_yO_{10-\delta}$ (y = 0.5, and 1.0) samples measured in air at 25-800 °C 95

Figure 4-34 Thermal expansion ($\Delta L/L_o$) curves of $PrSr_{2.7}Ca_{0.3}Fe_{3-y}Co_yO_{10-\delta}$ (y = 0.5, and 1.0) in air with a temperature range of 25-800 °C compared to LSGM electrolyte..... 96

Figure 4-35 The total conductivity of $PrSr_{2.7}Ca_{0.3}Fe_{3-y}Co_yO_{10-\delta}$ (y = 0.5, and 1.0) at 200-800 °C in air 98

Figure 4-36 SEM images of crossed section of the $PrSr_{2.7}Ca_{0.3}Fe_{3-y}Co_yO_{10-\delta}$ cathodes; (a) y = 0.5, and (b) y = 1.0. 99

Figure 4-37 (a) Terminal voltage and (b) power density as a function of current density of the cell for $PrSr_{2.7}Ca_{0.3}Fe_{3-y}Co_yO_{10-\delta}$ (y = 0.5, and 1.0) cathodes at 800 °C..... 101

Figure 4-38 ASR of the cell for $PrSr_{2.7}Ca_{0.3}Fe_{3-y}Co_yO_{10-\delta}$ (y = 0.5, and 1.0) cathodes at 800 °C 103

LIST OF TABLES

Table 2-1 Summary of the different fuel cell types 6

Table 2-2 Ionic conductivity of ceria-based electrolytes 12

Table 3-1 Chemicals and reagents in this research 23

Table 4-1 Peak area and perovskite to RP ratio in $LaSr_{3-x}Ca_xFe_3O_{10-\delta}$ (x = 0-1.0) 33

Table 4- 2 Average TECs of $LaSr_{3-x}Ca_xFe_3O_{10-\delta}$ (x = 0-0.7) in air at 25–800 °C 43

Table 4- 3 Percentage for each chemical state of Fe 2p in $LaSr_{3-x}Ca_xFe_3O_{10-\delta}$ (x = 0, 0.3 and 0.5). 47

Table 4- 4 The maximum power density of the single cells for the $LaSr_{3-x}Ca_xFe_3O_{10-\delta}$ cathodes (x = 0-0.7) at 600-800 °C in H_2 fuel. 50

Table 4- 5ASR of the single cells for the $LaSr_{3-x}Ca_xFe_3O_{10-\delta}$ cathodes (x = 0-0.7) at 600-800 °C in H_2 fuel. 54

Table 4- 6 Peak area and impurity to RP ratio in $LnSr_{2.7}Ca_{0.3}Fe_3O_{10-\delta}$ (Ln = La, Pr, and Sm) 56

Table 4-7 TECs of $LnSr_{2.7}Ca_{0.3}Fe_3O_{10-\delta}$ (Ln = La, Pr, and Sm) samples 62

Table 4-8 Chemical states of Pr 3*d* for $PrSr_{2.7}Ca_{0.3}Fe_3O_{10-\delta}$. 68

Table 4-9 Percentage for each chemical state of Fe 2*p* in $LnSr_{2.7}Ca_{0.3}Fe_3O_{10-\delta}$ δ (Ln = La, Pr, and Sm) 72

Table 4- 10 The maximum power density of the single cells for the $LnSr_{2.7}Ca_{0.3}Fe_3O_{10-\delta}$ (Ln = La, Pr, and Sm) cathodes at the temperature range of 600-800 °C in H_2 fuel. 74

Table 4-11 ASR of the single cells for the $LnSr_{2.7}Ca_{0.3}Fe_3O_{10-\delta}$ (Ln = La, Pr, and Sm) cathodes at 600-800 °C in H_2 fuel. 76

Table 4-12 Peak area and impurity to RP ratio in $PrSr_{2.7}Ca_{0.3}Fe_{2.5}B_{0.5}O_{10-\delta}$ (B = Fe, Ni, Co, and Cu) 78

Table 4- 13 Average TECs of $PrSr_{2.7}Ca_{0.3}Fe_{2.5}B_{0.5}O_{10-\delta}$ (B = Fe, Co, and Cu) samples at 25–800 °C 84

Table 4-14 The maximum power density of the single cells for the $PrSr_{2.7}Ca_{0.3}Fe_{2.5}B_{0.5}O_{10-\delta}$ (B = Fe, Co, and Cu) cathode at 600-800 °C in H_2 fuel. 89

Table 4-15 ASR of the single cells for the $PrSr_{2.7}Ca_{0.3}Fe_{2.5}B_{0.5}O_{10-\delta}$ (B = Fe, Co and Cu) cathodes at 600-800 °C in H_2 fuel 90

Table 4-16 Average TECs values of $PrSr_{2.7}Ca_{0.3}Fe_{3-y}Co_yO_{10-\delta}$ (y = 0.5, and 1.0) samples recorded in air at 25-800 °C 96

Table 4-17 The maximum power density of the single cells for the $PrSr_{2.7}Ca_{0.3}Fe_{3-y}Co_yO_{10-\delta}$ (y = 0.5, and 1.0) cathodes at the temperature range of 600-800 °C in H_2 fuel. 102

Table 4-18 ASR of the single cells for the $PrSr_{2.7}Ca_{0.3}Fe_{3-y}Co_yO_{10-\delta}$ (y = 0.5, and 1.0) cathodes at 600-800 °C in H_2 fuel 103

Table A-1 Ionic radius of related metal ions with their corresponding coordination numbers 22

Table A-2 Relative density of $LnSr_{3-x}Ca_xFe_{3-y}B_yO_{10-\delta}$ (x = 0-0.7; Ln = La, Pr, and Sm; B = Co, Cu and y = 0-1.0) 23

Table A-3 Peak area of Pr 3*d* for $PrSr_{2.7}Ca_{0.3}Fe_3O_{10-\delta}$. 23

Table A-4 Summary of peak areas for each chemical state of Fe 2*p* in $LnSr_{2.7}Ca_{0.3}Fe_3O_{10-\delta}$ (Ln = La, Pr, and Sm). 24

CHAPTER I

INTRODUCTION

In the 21st century, electricity and transportation are important for the modern life. These sectors are really related to the energy consumption. Figure 1-1 illustrated the energy source of the world consumption in 2015 and fossil fuels are considered the major source as 86% of the world energy usage. While the global energy demand is rising, two major problems have been concerned. Firstly, the reproducibility of fossil fuel is limited. Secondly, fossil fuel combustion causes CO_2 emission and pollutants, NO_x and SO_x, which relates to a greenhouse effect, global warming, and acid rain. Moreover, to convert fossil fuel to energy, this process requires the conversion of fuel to heat, then to mechanical energy and consequently to electrical energy, which is limited by the Carnot-efficiency (~30% efficiency). To decline these problems, the different way to produce energy with high efficiency and cleanliness is important. Fuel cells are an alternative way to use as the energy devices, which directly convert chemical fuel to electricity through the electrochemical reaction of fuel and oxidant without any intermediate physical conversion step and attain high energy conversion efficiency with significantly lower pollutant emission than conventional internal-combustion engines. Therefore, the main feature of fuel cell is the efficiency, which is not limited by the Carnot-cycle.

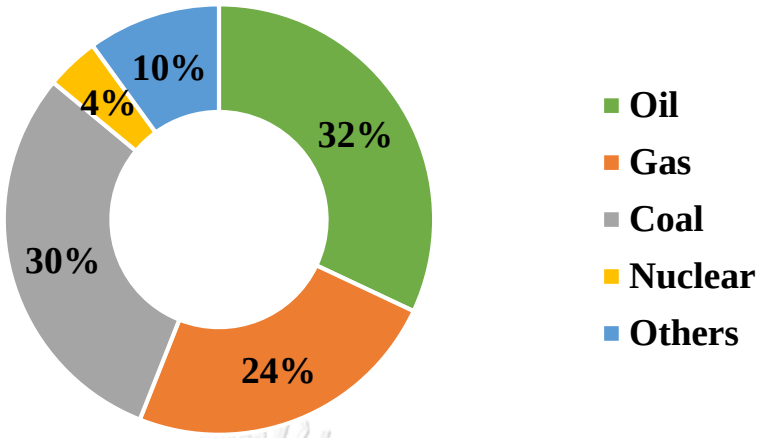

Figure 1-1 World consumption of primary energy by a source in 2015 [1]

In fuel cell technology, the electrochemical combination of oxidant (oxygen in air) and fuel (hydrogen from several sources) across an ionic membrane is the main function. Although fuel cells are not a new technology, their potential in transportation recently causes a huge attention to the world. [2]

There are many types of fuel cells classified by the type of electrolyte. Among them, solid oxide fuel cells (SOFCs) have strongly gained attention in a couple decades as a stationary power source due to their several advantages. [3-8] Fuel flexibility and high-efficiency generation (~50-60% efficiency) are major preferences of SOFCs.

SOFCs compose of cathode, electrolyte, and anode under a feeding of hydrogen and oxygen source to cathode and anode as fuel and oxidant, respectively, at a high operating temperature (around 900-1000 °C) to achieve the satisfied oxygen fluxes. [7, 9, 10] However, the high operating temperature causes some problems affecting the fuel cell performance, for example, reaction occurs between electrode and electrolyte. [11] A conventional SOFC cathode, $La_{1-x}Sr_xMnO_3$, reacted with a conventional yttria-stabilized zirconia electrolyte and formed an insulating phase of $La_2Zr_2O_7$ at 1000 °C, which reduced the conductivity of the cell. [12] Moreover, the thermal expansion coefficient (TEC) of each

component at high temperature is different and incompatible, resulting in delamination between the component. For these reasons, the development of each component to operate at lower temperature has been attempted.

The required properties for cathode material are the mixed ionic and electronic conductivity (MIEC) as well as the well-matched thermal expansion coefficient (TEC) with other components to provide good performance and durability. The electronic conduction process performs through the electron transportation between metal and oxygen in the structure while the ionic conduction occurs by jumping of the occupied oxide ion in the lattice to a vacancy. [7] Perovskites and -perovskite-related structure materials have been intensively studied because they have mixed ionic and electronic conductive property. However, the low operating temperature obstructed oxygen reaction at the cathode. Thus, the development of these materials to use as a cathode for low operating temperature is a challenge.

Among perovskite-related structures, Ruddlesden-Popper (RP) phase had been discovered by Ruddlesden-Popper in 1957. [13, 14] This structure consists of *n* perovskite layers separated by a rock salt layer. The first discovery of this phase was $Sr_3Ti_2O_7$, however, the derivative of this material by substitution of several different cations for both Sr and Ti sites as well as the increase in number of perovskite layers to achieve the desired properties, such as $A_{n+1}M_nO_{3n+1}$ (A = Sr, La, Nd and Sm; M = Al, Ga, Co, Fe, and Mn), had been studied. [15-20] However, these materials had poor electronic conductivity compared to perovskite. Thus, the development of RP structure to use as cathode material is interested. In this regard, this research was aimed to develop alternative material with sufficient catalytic activity and acceptable TEC, which are major issues of the cathode in SOFC at low operating temperature (600-800 °C). With this purpose, the investigation of Ruddlesden-Popper perovskite-related oxide $LnSr_{3-x}Ca_xFe_{3-y}B_yO_{10-\delta}$ (Ln = La, Pr and Sm; x = 0-1.0; B = Co, Ni and Cu; y = 0-1.5) has been focused in order to achieve a potential material which has proper thermal expansion coefficient closed to the electrolyte and good conductivity and electrochemical performance, to be used in intermediate temperature SOFC.

CHAPTER II
BACKGROUND AND THEORY

2.1 Fuel cells

Fuel cells are energy conversion device which generates electricity and heat from an electrochemical reaction between a fuel (typically H_2 from a variety of source) and oxidant (typically O_2 from the air), as equation (2-1). This function is similar to a battery with the external fuel supply. The basic components of fuel cells comprise an electrolyte, a porous cathode, and a porous anode as any other electrochemical cell.

$$H_2 + O_2 \longrightarrow H_2O + \text{electrical power} + \text{heat} \qquad (2\text{-}1)$$

Recently, the fuel cells have been received much attention, although their concept was initiated since the 19th century by Sir William Grove, who successfully operated the hydrogen-oxygen cell in 1839 and when the electrolysis of water was investigated. Glove found a little flow of electrical current in the reverse direction, which supposed to be the flow of electron from the electrolysis of water when the current was not applied. Glove confirmed this by feeding hydrogen and oxygen to each side of the platinum electrode and found the current flow and water generation. This discovery is a beginning of fuel cell history. [21]

The development of ceramic or solid fuel cells commenced in the late of the 19th century with the discovery of Nernst who found that zirconia (ZrO_2) can conduct the ion at high temperature (above 600°C) even though it has a huge resistance at room temperature. Its electrical resistance also could be reduced with the addition of other elements such as magnesia, yttria, and calcia. Surprisingly, the combination of yttria (Y_2O_3) with zirconia is the most promising mixture and has been widely used as electrolyte material in Solid Oxide Fuel Cells (SOFCs). [22]

In 1937, Baur and Preis investigated the first working tubular SOFC by using 10 % w/w MgO and 10 % w/w Y_2O_3 doped ZrO_2 as the electrolyte, while iron or carbon and

magnetite (Fe_3O_4) were used as the anode and cathode, respectively. Even the electrochemical performance of the SOFC cell was evaluated, the current density was really poor (approximately 0.3mA·cm^{-2}) to be used for practical work. Moreover, the fuel reaction was not clearly understood [23]. In the early 1960s, the development of electrolyte and electrode in SOFC, especially the increase of electrolyte conductivity, has been intensively considered with the main purpose as new energy device for military, space, and transport. The research was subsequently studied with several fuels on the alkaline fuel cell system for the project of NASA Apollo space program from 1960 to 1965 by space-technology sector. [24]. The research activities in fuel cell technology have been continuously focused until today.

2.2 Classification of fuel cells

Fuel cells are classified into five different categories according to the type of electrolytes as listed in Table 2-1. The electrolyte, operating temperature, fuel composition and charge carrier of each type are compared. The type of fuel cells is normally classified by the nature of electrolyte, which controls the type of transferred ions and their transportation. In addition, each electrolyte also requires different ranges of operating temperature. Molten Carbonate Fuel Cells (MCFC) and Solid Oxide Fuel Cell (SOFC) requires high operating temperatures, while Alkaline Fuel Cells (AFC), Polymer Electrolyte Membrane Fuel Cells (PEMFC) and Phosphoric Acid Fuel Cells (PAFC) can be operated in much lower operating temperature.

Table 2-1. Summary of the different fuel cell types [25, 26]

Fuel cell type	Abbreviation	Operating temperature [°C]	Fuel	Charge carrier	Electrolyte
Alkaline Fuel Cell	AFC	100	Highly pure H_2	OH^-	KOH aqueous
Solid Polymer or Polymer Electrolyte Membrane Fuel Cell	SPFC/PEMFC	80-110	Pure H_2	H^+	PFS* acid membrane
Phosphoric acid Fuel Cell	PAFC	150-210	CO-free H_2	H^+	H_3PO_4
Molten Carbonate Fuel Cell	MCFC	550-650	H_2, CH_4, CO	CO_3^{2-}	Molten Li_2CO_3-K_2CO_3
Solid Oxide Fuel Cell	SOFC	600-1000	Hydrocarbon, H_2, CO	O^{2-}	Solid YSZ**

*PFS = Perfluorosulfonic

**YSZ = Y_2O_3-stabilized ZrO_2

Among fuel cell technologies, PEMFC and SOFC show high potential to achieve the target efficiency and cost because the high operating temperature of PEMFC and SOFC provides good efficiency and low sensitivity to the composition of the fuel. However, the precious metals, an anode in PEMFCs system, are poisoned by sulfur- or CO-contained compound, even in a low concentration level, a pure H_2 fuel stream is therefore required in PEMFCs system. Thus, Solid Oxide Fuel Cells (SOFCs) are an attractive system due to excellent fuel flexibility such as hydrocarbon, biogas, and hydrogen without employing precious metals as the anode. [27-29]

2.3 Solid oxide fuel cells (SOFCs)

2.3.1 Definition and principle

A SOFC fuel cell, which a solid ceramic, dense metal oxides, is used as an electrolyte. This electrolyte is an oxide ion (O^{2-}) conductors, which have negligible electronic conductivity and impenetrable to gas flow. A high operating temperature (typically in the temperature of 800-1000°C) is required for the solid oxide electrolytes to provide an appropriate conductive.[3] The electrolyte also separates anode and cathode, which are exposed to fuel and oxygen, respectively.

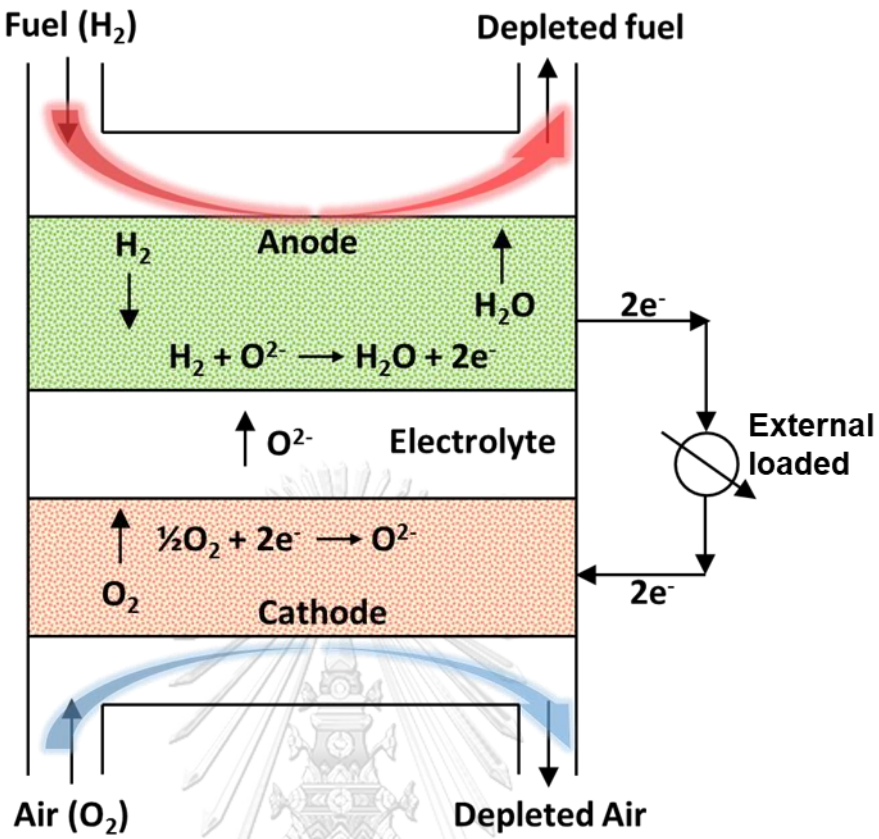

Figure 2-1 Schematic of a solid oxide fuel cell

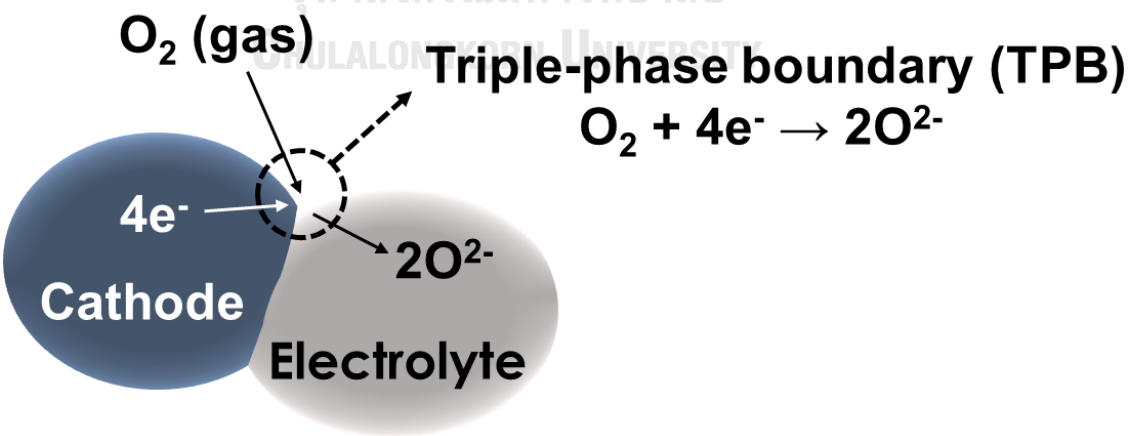

Figure 2-2 Schematic diagram of the triple-phase boundary (TPB) on the cathode.

The principle of conventional SOFC operation is demonstrated in Figure 2-1. At the cathode, oxygen is dissociated and electrochemically reduced (oxygen reduction reaction, ORR) to oxide ions (O^{2-}) by charge transfer reaction with electron consumption from the external circuit at the cathode-electrolyte-gas interface, as described in equation (2-2). The generated oxide ions migrate through an electrolyte with a vacancy hoping mechanism to the anode-electrolyte-fuel interface and then react with the hydrogen or fuels at the anode through electrochemical oxidation reaction to liberate electrons and form water as the by-product as described in equation (2-3). [30, 31] The reactions of oxygen reduction and fuel oxidation occur at the interfacial area between electrode, electrolyte and gaseous phase, which is called triple-phase boundary (TPB), as demonstrated in Figure 2-2. [32] The overall electrochemical reaction occurred at TPB can be written as equations (2-4).

Cathode $\frac{1}{2} O_{2,c} + 2e^- \rightleftharpoons O^{2-}_e$ (2-2)

Anode $H_{2,a} + \frac{1}{2} O^{2-}_e \rightleftharpoons H_2O_a + 2e^-$ (2-3)

Overall reaction $H_{2,a} + \frac{1}{2} O_{2,c} \rightleftharpoons H_2O_a$ (2-4)

where *a*, *c*, and *e* subscript are species located at the anode, cathode, and electrolyte respectively.

Electrical circuit generation is started from the oxidation of fuel on the anode to release electrons, which are conducted through the external circuit, performed work, and returned to the SOFC system at the cathode. The difference in oxygen activity between fuel at the anode and oxidant at the cathode is the driving force for transporting oxide ions through the electrolyte,

2.3.2 Electrochemical performance of SOFC

The performance of a single cell is related to the current-voltage curve (*I-V*), as illustrated in Figure 2-3. The I-V curve consists of main polarizations, which are the open circuit voltage (OCV) (lower than the theoretical value), the initial rapid decrease in voltage at low current density region or activation polarization, the slowly

decrease in voltage at intermediate current density region or ohmic polarization and the rapid decrease in voltage at high current density region or concentration polarization. The difference in voltage which is deviated from the theoretical value is influenced from several factors, for example, the thickness of electrolyte, operating temperature, properties and microstructure of electrode and electrolyte, and gas flow rate. The activation polarization is related to the kinetic reactions on the electrodes. The ohmic polarization concerns on the resistance from the charge carrier, electrons, and ions. The concentration polarization is related to the limitation of mass transfer of electrode.

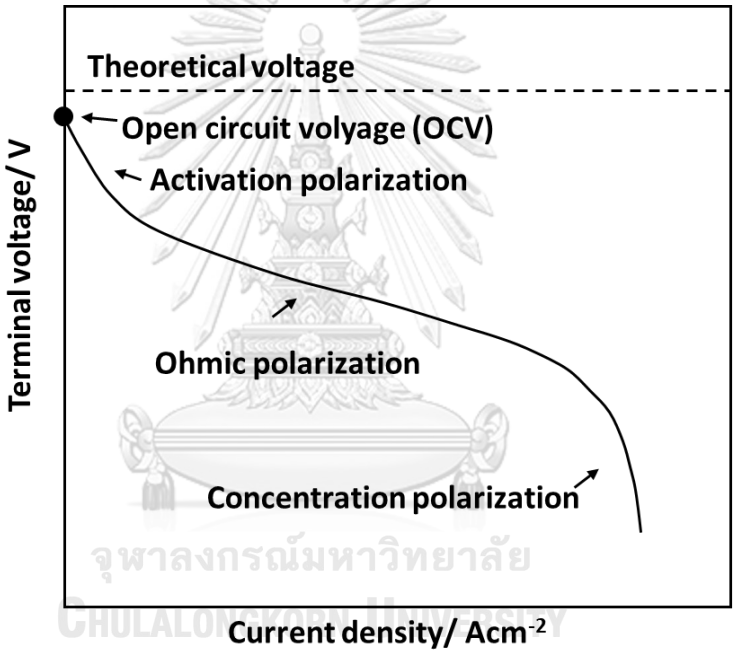

Figure 2-3 Current-voltage *(I-V)* curve of a fuel cell and the polarization loss.

2.3.3 SOFC materials

SOFCs consist of electrolyte, anode, and cathode as the basic components. Each component has to achieve its function for minimizing the energy loss. The requirements of each component include good stability in chemical, phase and morphological under oxidizing and/or reducing atmosphere, chemical

compatibility with other components as well as a proper conductivity. Both electrodes, anode, and cathode, require a porous structure to allow gas diffusion to the reaction site, while the dense electrolyte is needed to separate the oxidant and fuel gases. The requirement of electrolyte, cathode, and anode are described as follows

2.3.3.1 Electrolyte requirement

The electrolyte material for SOFC is an oxide-ion conductor, that transfers the ionic charge from the cathode to the anode. It is also used as a physical barrier to separate between the oxidant and fuel; the electrolyte thus needs to be thin enough to minimize ohmic losses and also be stable and compatible with both electrodes at high operating temperatures. The materials for SOFC electrolyte require not only high oxide-ion conductivity (> 0.05 S cm^{-1} at operating temperature) with no or barely electronic conductivity but also an excellent mechanical strength with fracture strength > 400 MPa at room temperature as well as proper phase and thermal stability in a wide range of temperature. [33]

Zirconia-based oxide (ZrO_2), a cubic fluorite structure, has commonly been used as the conventional electrolyte for SOFCs, especially yttria-stabilized zirconia, $(Y_2O_3)_{0.08}$-$(ZrO_2)_{0.92}$ or YSZ, because it shows a pure ionic conductivity over a wide range of oxygen partial pressures at high temperature (900-1000 °C). [3, 34] Although the substitution of a trivalent cation such as $Y^{3+}$for Zr^{4+} improved the deficiency of ionic conductivity of ZrO_2 by creating a high concentration of oxygen vacancy in the crystal lattice, which provides channels for oxide-ion conduction, stabilizes the fluorite structure at room temperature and reduces the phase transition problem. YSZ showed low oxide-ion conductivity at intermediate temperatures (500–800 °C).

Ceria-based oxides have been considered as an alternative electrolyte because it provides high ionic conductivity at intermediate temperatures, as shown in Figure 2-4 [35-37]. The substitution of Gd^{3+} or Sm^{3+} for Ce^{4+} in CeO_2 is able to increase the ionic conductivity of CeO_2, as shown in Table 2-2. However, the

reduction of Ce^{4+} to Ce^{3+} ions at the low oxygen partial pressure of ceria-based electrolytes is the main drawback because it creates the electronic conduction in ceria which consequently decreases the cell efficiency [38]. Even the YSZ thin film (functional layer) has been used between the anode and ceria electrolyte [39, 40], impurity phases, which have low oxide-ion conductivity, are formed at the interface between YSZ and GDC [41, 42].

Table 2-2 Ionic conductivity of ceria-based electrolytes[43]

Dopant	Concentration (Mol %)	Conductivity ($S \cdot cm^{-1}$)		Activation energy ($kJ \cdot mol^{-1}$)
		700 °C	500 °C	
Sm_2O_3	10	3.5 × 10-2	2.9 × 10-3	68
Gd_2O_3	10	3.6 × 10-2	3.8 × 10-3	70
Y_2O_3	10	1.0 × 10-2	2.1 × 10-3	95
CaO	5	2.0 × 10-2	1.5 × 10-2	80

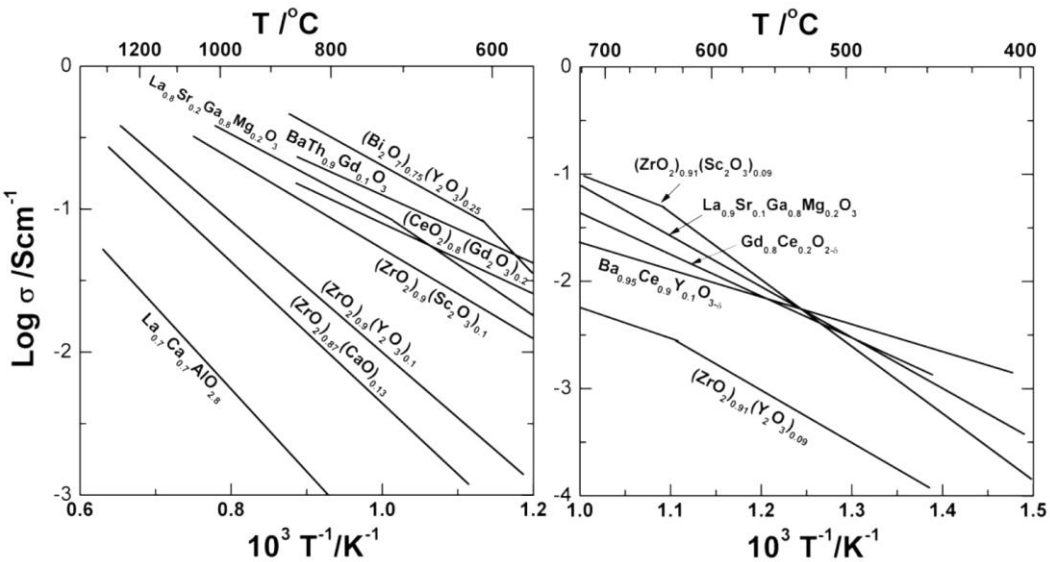

Figure 2-4 Electrical conductivity of various electrolytes depending on temperature [36]

$LaGaO_3$ perovskite has also been investigated as an alternative electrolyte, especially $La_{1-x}Sr_xGa_{1-y}MgyO_3$ (LSGM). The composition of $0.1 \leq x \leq 0.2$ and $0.15 \leq y \leq 0.2$ had been widely studied [44] because it not only provides high ionic conductivity similar to that of YSZ at 1000°C (> 0.1 S cm^{-1} at 800 °C), as shown in Figure 1.5, but also shows the chemical stability over a wide range of temperatures and oxygen partial pressures [45-47]. Moreover, LSGM shows higher stability in reducing atmosphere compared to the ceria-based electrolyte. Even La in LSGM can react with Ni anode and produces undesired $LaNiO_3$ or $La2NiO_4$ phases, which are drastically decreased the ionic conductivity of LSGM, [48] the preparation of the cell at low temperature possibly reduced this problem. Therefore, LSGM is chosen as an electrolyte in this research.

2.3.3.2 Anode requirement

Anode material is a catalyst for the fuel oxidation reaction at the operating temperature. Therefore, the anode material must have good electronic conductivity to release electrons which can be utilized as current, catalytically active for fuel oxidation and internal hydrocarbon reforming, and sufficient porosity to transport fuel to the active site as well as for water vapor to exit. The anode material should also tolerate the contamination and deactivation by impurity in fuel. As the similar reason as a cathode, the anode materials should have good thermoelectrical under reducing environments, chemical stability, compatibility and TEC matching with electrolyte and other cell components. [6, 49-51]

In the past, nickel metal (Ni) is one of the materials which is used as anode materials for SOFC because it tolerates in the reducing atmosphere and high temperature. Even noble metals, such as platinum and gold, is also possible to use as anode materials, the high cost of these materials is not suitable for the commercialization. Moreover, as considerate in term of chemical stability, catalytic activity, volatility, and cost, Ni can be the best candidate. Ni acts as electronic conducting phase, which transports the electrons from the reaction site to the current

collector. However, at high operating temperature, Ni particles are easy to aggregate and then block pores leading to gas transportation limit.

To moderate these issues without decreasing the anodic activity, the secondary metal had been alloyed in pure Ni and provided a synergistic effect. The partial addition of Fe, Cu, and Co into Ni decreased the polarization resistance and improved the cell performance of nickel, especially for Fe [52-55]. The addition of Fe in Ni-cermet improved performance of the Ni-cermet anodes [52, 56-58]. Therefore, The Ni-Fe alloy is used as anode material in this research.

2.3.3.3 Cathode requirement

The cathode material is a catalyst for oxygen reduction reaction (ORR) at high operating temperature. The materials require an adequate catalytic activity to decrease the electrode polarization for ORR and thermodynamical stability under oxidizing atmospheres at high operating temperatures. The cathode materials should also provide the sufficient electronic and oxide ion conductivity higher than 100 $S{\cdot}cm^{-1}$ and 0.1 $S{\cdot}cm^{-1}$, respectively, at the operating temperatures. Moreover, the chemical stability and compatibility with the electrolyte at high temperatures, the adequate porosity for gas transportation to the reactive sites, and good matching of the thermal expansion coefficients (TEC) with those of other components of the cell to avoid cracking and delamination. [6, 50, 59]

2.3.3.4 Cathode review

The Sr-doped lanthanum manganite ($La_{1-x}Sr_xMnO_3$ (LSM) with $0.15 \leq x \leq 0.30$), a traditional cathode material for SOFCs, has a perovskite structure and good electrochemical activity for ORR at high temperatures (800-1000°C). LSM shows low TEC of $11 \times 10^{-6} - 13 \times 10^{-6}$ °C^{-1} in the temperature range of 35-1000°C, which is compatible with that of YSZ. [60, 61] Although LSM shows acceptable electronic conductivity, it is poor ionic conductivity because Mn^{4+} is stable and it is difficult to generate the oxygen vacancies in the LSM structure, resulting in almost oxygen-stoichiometric materials. [62-64] To approach high ionic conductivity materials,

materials with the same structure or element as an electrolyte are chosen to make a composite with LSM. For example, LSM reacts with YSZ to forms $La_2Zr_2O_7$, which is an insulating phase at high temperature [65], but it can be operated at intermediate temperature (600-800°C) However, LSM remains intrinsically poor ionic conductivity and insufficient catalytic activity at intermediate operating temperature. [43, 62, 66-68] The alternative materials, which give a good mixed ionic and electronic conductivity (MIEC) and high catalytic activity for ORR, for intermediate operating temperature SOFC is intensively developed in order to replace LSM. Sr-doped lanthanum cobaltite ($La_{1-x}Sr_xCoO_3$: LSC) has been introduced because it maintains good electronic conductivity (>1300 Scm^{-1}) at intermediate temperature range [69, 70] However, the large oxygen loss from lattice and the transition of Co^{3+} $3d^6$ ion between high- and low-spin states causes the unacceptable-high TEC value of 20×10^{-6} K^{-1} that relates to the delamination of the cell. [66, 71-73]. The substituted Fe for Co in LSC, forming $La_{1-x}Sr_xCo_{1-y}Fe_yO_{3-\delta}$ (LSCF), can decrease this problem. $La_{0.6}Sr_{0.4}Co_{0.8}Fe_{0.2}O_{3-\delta}$ is a common composition with high electronic conductivity of 250 Scm^{-1} at 800 °C [74] and sufficient ionic conductivity (>10^{-2} Scm^{-1}) at 800 °C. [75] However, the decreasing of Co content in LSFC needs to be traded-off between the decrease in catalytic activity and the decreasing of TEC which promotes its long-term stability for practical application. [19, 76] Researchers are thus interested to look away from the perovskite oxide to a new cathode material with good catalytic activity and low TEC for intermediate temperature SOFC.

Among the variety of new structure materials, the Ruddlesden-Popper (R-P) oxides have been received much attention because of their flexibility in terms of oxygen content that can improve oxide-ion conductivity. The RP structure ($A_{n+1}B_nO_{3n+1}$) consists of rock-salt (AO) layers sandwiched with the (ABO_3) perovskite n layers along the *c* axis [77, 78] When n = ∞, the structure can be regarded as a perovskite. The RP structures are shown in Figure 2-5.

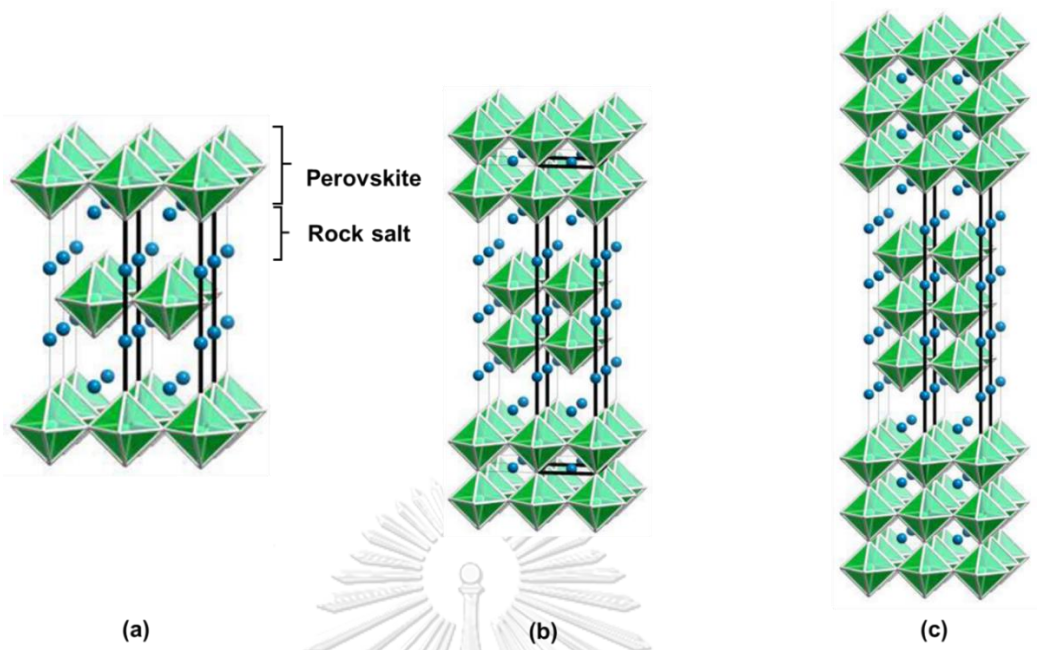

Figure 2-5 Crystal structures of Ruddlesden–Popper phase *(a)* n=1, *(b)* n=2 and *(c)* n=3 [13]

The RP phase is interesting because it provides the flexibility in terms of oxygen content, which improves oxide-ion conductivity at an intermediate temperature, particularly in the RP (n = 1) with the general formula of A_2BO_4 due to the transportable of excess oxygen in its structure. [79] The ionic conductivity of RP (n = 1), such as $La_2NiO_{4-\delta}$ (0.02 $S.cm^{-1}$), was found significantly higher than LSCF perovskite structure (0.003 $S.cm^{-1}$) at 700 °C. [79, 80] because of the localization of excess oxide ions in the tetrahedral interstitial sites of the adjacent rock-salt LaO layers, though the electronic conductivity of $La_2NiO_{4-\delta}$ structure was lower than LSCF. [19, 81-84]

Velinov *et al.* [84] reported the conductivity of the Ruddlesden-Poper phase of $(LaSr)_{n+1}Fe_nO_{3n+1}$ (n = 1, 2 and 3) synthesized by a nitrate-citric method. As increasing of *n*, the lattice parameters *a* and *c* and the unit cell volume increased. $LaSrFeO_4$ (n=1) was formed at 900°C without the additional phase. $La_2SrFe_2O_{7-\delta}$ (n=2) was prepared at 1400°C with the $LaSrFeO_4$ and perovskite co-exist phases. While $LaSr_3Fe_3O_{10-\delta}$ (n=3) needed a higher temperature over 1100°C to generate the phase but $LaSrFeO_{4-\delta}$, $La_2SrFe_2O_{7-\delta}$ and perovskite are co-existed phases. The electronic

conductivity of $LaSr_3Fe_3O_{10-\delta}$ was significantly higher than $La_2SrFe_2O_{7-\delta}$ and $LaSrFeO_{4-\delta}$ at temperature over 140°C.

The increasing of the number of perovskite layer, *n*, leads to the increase in electronic conductivity because the electron can localize through the BO_6 octahedral in the perovskite structure (Figure 2-6(a)).[85] The *d*-orbital of *B*-site overlaps with *p*-orbital of oxygen (Figure 2-6(b)), resulting in localization of electron in the perovskite structure. Thus, the increasing of the number of perovskite layer supports an increase in the O-B-O interaction along the *c* axis and subsequently increases electronic conductivity. However, the thermal expansion coefficient (TEC) of RP n = 3 was higher than that of RP n = 1. $Sr_4Fe_3O_{10-\delta}$ provides the TEC approximately $17x10^{-6}$ while $Sr_2FeO_{4+\delta}$ was approximately $13x10^{-6}$. [86] Moreover, the thermal degradation of RP n =3 was concerned.[87]

Figure 2-6 (a) The perovskite structure (ABO_3) [87], (b) Covalent bonds between anionic p-orbital and d-orbital of *B*-site cation

Fossdal *et al.* [87] studied the thermal stability of $Sr_2FeO_{4+\delta}$ and $Sr_4Fe_3O_{10-\delta}$ phases. The samples were prepared by a solid-state reaction method. The degradation of these samples was investigated by powder x-ray diffraction and in-situ high-temperature X-ray diffraction (HTXRD) techniques at 800-1000 °C. The $Sr_2FeO_{4+\delta}$ and $Sr_4Fe_3O_{10-\delta}$ showed the thermal degradation at 930 °C and 850 °C in air, respectively. With decreasing of oxygen partial pressure (pO_2), the decomposition

temperatures of both $Sr_2FeO_{4+\delta}$ and $Sr_4Fe_3O_{10-\delta}$ were decreased. $Sr_4Fe_3O_{10-\delta}$ also showed higher oxygen vacancies than $Sr_2FeO_{4+\delta}$ in both atmospheres, air, and N_2. However, the effect of pO_2 had a lower influence on $Sr_4Fe_3O_{10-\delta}$ compared to $Sr_2FeO_{4+\delta}$. The concentration of oxygen vacancies in the structure was concerned to be the main factor for the difference in thermal stability between the materials.

Lee *et al.* [88] reported that a partial substitution of La for Sr stabilizes the $Sr_4Fe_3O_{10-\delta}$ phase. The amount of oxygen vacancy affected the structure degradation and no phase degradation was observed in $LaSr_2Fe_3O_{10-\delta}$ ($0.1<\delta<0.8$). The stoichiometry of oxygen in the structure varied in air as a function of temperature. With increasing temperature from 100 to 900°C, the oxygen content decreased from 9.88 to 9.45, which corresponds to the linearly decreasing of the value of *c*-axis parameter. The oxygen vacancies were found at the apical oxygen joining of the octahedral sites and they localized on the central FeO_6 octahedral with three sequential FeO_6 octahedral along the *c* axis.

The substitution of trivalent metal for Sr in RP structure was not only affected the thermal stability but also TEC and conductivity. Kim *et al.* [18] investigated the effect of ionic radius of lanthanide metal substituted for Sr in $Sr_{0.7}Ln_{0.3}Fe_{1.4}Co_{0.6}O_{7-\delta}$ (Ln = La, Nd, Sm and Gd), RP n = 2, as cathode materials for SOFC. No structural degradation in air was found by the substitution of La, Nd, Sm for Sr, except the substitution of Gd due to the different size between Sr^{2+} and Gd^{3+}. The TEC value was reduced by reducing Ln^{3+} size. However, the electrical conductivity and the fuel cell performance decreased with the decreasing size of Ln^{3+} ions from La^{3+} to Nd^{3+} and Gd^{3+} due to the increase of oxygen vacancy concentration. Kim *et al.* [89] also investigated the effect of ionic radius of lanthanide metal substituted for Sr in $LnSr_3Fe_3O_{10-\delta}$ (Ln = La, Nd, and Gd), RP n = 3. Even the oxygen content in the structure and the conductivity showed the similar trend as RP n = 2, which were decreased with the decreasing size of Ln^{3+} ions from La^{3+} to Nd^{3+} to Gd^{3+}, the electrochemical performance of $NdSr_3Fe_3O_{10-\delta}$ was improved while the $GdSr_3Fe_3O_{10-\delta}$ showed the lowest performance. The improvement in electrochemical performance of

$NdSr_3Fe_3O_{10-\delta}$ was described as it had high surface oxygen exchange kinetics due to the high oxygen vacancies and total electrical conductivity. However, the result was different from the electrochemical performance of RP n = 2.

The size of ionic radii of *A*-site ion significantly affects the RP structure. Tang *et al.* [90] investigated the solubility limit of the divalent ion on $La_{2-x}A_xNiO_4$ (A = Ca, Sr, Ba) and found that the substitution of the cation with a different size from the host leads to the stress in the structure. The solubility limits in a mole ratio of Ca, Sr, and Ba cations were reported as 0.6, 1.5, and 1.1, respectively. The samples with composition of x<0.3 presented an excess oxygen content whereas x>0.3 samples provided the oxygen vacancies in the following order Ca > Ba > Sr. Even Ca has small ionic radii and provided more compressive stress in the metal-O bond comparing to Sr^{2+}, Ca^{2+} preferred the 8-fold coordination and favored oxygen vacancies in the structure more than the excess oxygen. On the other hand, Ba^{2+} substitution had a lower tensile stress in the metal-O bond because it has larger ionic radii compared to Sr^{2+}, but it generated the oxygen vacancies.

The research of isovalent substitution for rare-earth metal in RP structure is limited, especially Ca substitution for Sr, however the substitution of divalent for Sr^{2+} and Ba^{2+} on double perovskite was studied. Choi *et al.* [91] studied the effect of Sr^{2+} substituted for Ba^{2+} in $LaBa_{1-x}Sr_xCo_2O_{5+\delta}$ (x = 0 and 0.5) and found that the conductivity increased due to the decreasing of oxygen vacancies. Yoo *et al.* [92] investigated $NdBa_{1-x}Sr_xCo_2O_{5+\delta}$ (x = 0, 0.25, 0.5, 0.75, and 1.0) and found that the Sr substitution enhanced the conductivity by reducing oxygen vacancy in the $NdBaCo_2O_{5+\delta}$ structure. With increasing of Sr concentration, the conductivity increased by the increase of electronic holes associated with oxygen content. However, Wang *et al.* [93] reported that the Ca substitution for Ba, $SmBa_{1-x}Ca_xCoCuO_{5+\delta}$ (x = 0-0.3), showed the decrease in oxygen content with increasing of Ca concentration and oxygen vacancy in the structure, which was opposed to the work report by Choi *et al.* [91] and Yoo *et al.* [92]. The decrease in oxygen vacancy reduced the area specific resistance (ASR) of the material and enhanced the sing cell performance for Ni-

YSZ|YSZ|GDC| $SmBa_{1-x}Ca_xCoCuO_{5+\delta}$ (x = 0-0.3). Zheng et al. [94] studied the substitution of Ca for Ba in $SmBa_{1-x}Ca_xCo_2O_{5+\delta}$ (x = 0 and 0.25) and found that the oxygen content in $SmBaCo_2O_{5+\delta}$ increased by Ca substitution. On the contrary, the conductivity of $SmBa_{0.75}Ca_{0.25}Co_2O_{5+\delta}$ was lower than the Ca-free sample. However, the effect of small ionic radii of rare-earth metal on oxygen vacancies and conductivity of double perovskite materials was not clearly understood. Moreover, the variation of Ca for Sr in the RP structure was also limited. Therefore, the effect of Ca substitution for Sr in $LaSr_3Fe_3O_{10-\delta}$ was investigated in this research.

Among the various compositions of the RP structure investigated, $La_{n+1}Ni_nO_{3n+1}$ was extensively investigated due to its high oxygen diffusion compared to LSCF perovskite and the TEC compatible with those of standard electrolytes [95]. However, it provided poor electronic conductivity similar to the $Sr_{n+1}Fe_nO_{3n+1}$ series. Amow et al. [19] investigated the substitution of Co for Ni in $La_4Ni_{3-x}Co_xO_{10\pm\delta}$ (x = 0-2) and found that the structure of $La_4Ni_{3-x}Co_xO_{10\pm\delta}$ transferred from orthorhombic *Bmab* to *Fmmm* under different Co concentration. The *Bmab* structure was detected for x = 0-0.2 and 0.8-1.8, while the *Fmmm* structure was observed at x = 0.4-0.6. The conductivity of $La_4Ni_{3-x}Co_xO_{10\pm\delta}$ was decreased with the increasing of Co concentration due to the reduction in oxygen content in the structure. However, the ASR was decreased by Co addition, which was associated with amounts of the Co^{2+}/Co^{3+} ions. Ferkhi *et al.* [96] evaluated the electrochemical performance of $La_2Ni_{1-x}Cu_xO_{4+\delta}$ (x=0-0.1) and found that doping of Cu decreased the total resistance and improved the electrochemical performance. However, with x > 0.01, $La_2Ni_{1-x}Cu_xO_{4+\delta}$ reacted with YSZ electrolyte and generated $La_2Zr_2O_7$ and unidentified phase because Cu diffused to the cathode-electrolyte interface. Mogni *et al.* [97] investigated the oxygen content of $Sr_3FeMO_{6+\delta}$ (M = Fe, Co, Ni) RP structure and found that the oxygen-vacancy concentration decreased with decreasing size of substituent M in the order of $Sr_3FeNiO_{6+\delta}$ > $Sr_3FeCoO_{6+\delta}$ > $Sr_3Fe_2O_{6+\delta}$. They also suggested that the ionic conductivity should increase in the order of $Sr_3FeNiO_{6+\delta}$ > $Sr_3FeCoO_{6+\delta}$ > $Sr_3Fe_2O_{6+\delta}$. Armstrong *et al.* [83] studied the Co substitution for Fe in $LaSr_3Fe_{3-x}Co_xO_{10-\delta}$ (x = 0-1.5)

and found that the conductivity was increased with the increase in Co addition due to the increasing of covalence in the (Fe, Co)-O bond and the reduction of oxygen vacancy in the structure. The oxygen permeation flux also increased with increasing of Co content, suggesting the ORR of $LaSr_3Fe_3O_{10-\delta}$ was promoted by the Co addition. Lee et al. [98] evaluated the electronic conductivity and TEC value of $LaSr_3Fe_{3-x}Co_xO_{10-\delta}$ (x = 0-1.5) and found that the conductivity of samples increased with increasing of Co concentration. This result was in agreement with the work reported by Armstrong *et al.*, who explained the increasing of conductivity by the increase in the covalent interaction between the O-(Fe,Co)-O bond. However, the TEC was dramatically increased by the Co addition because of the transition of Co^{3+} from low-spin to high-spin and the reduction in the electrostatic attractive forces between the cations and anions, which resulted in a decrease of oxygen vacancy in the structure and the increase of TEC. Therefore, the substitution of Ni, Cu, and Co for Fe in the RP structure of Ca-substituted $LaSr_3Fe_3O_{10-\delta}$ was also investigated.

From literature survey in other perovskite and perovskite-related oxides, the substitution of Ni and Cu for B cation can provide a large number of oxygen vacancies and increases electrochemical performance. The substitution of Ca for A cation and the decreasing of A cation size can decrease TEC and improve the conductivity. Furthermore, $(Sr_{1-x}Ln_x)_{n+1}(Fe_{1-y}M_y)_nO_{3n+1}$ with n=3 (M = transition metal) has been investigated a much lower extent compared to the perovskites and RP structure with n=2. Therefore, the aim of this work is to investigate the thermal expansion behavior and electrochemical properties, *e.g.* conductivity, fuel cell performance of $LnSr_{3-x}Ca_xFe_{3-y}B_yO_{10-\delta}$ (Ln = La, Pr and Sm; x = 0-1.0; B = Co, Ni and Cu; y = 0-1.5) for intermediate-temperature SOFC (IT-SOFC) based on the hypothesis that the substitution of smaller Ln and Ca for Sr will decrease the TEC value and increase the oxygen vacancy, while the substitution of Co and Ni for Fe increases conductivity.

CHAPTER III
EXPERIMENTAL

3.1 Material preparation

3.1.1 Chemicals and reagents

The cathode, electrolyte, and anode materials used in this research were synthesized by a citric nitrate combustion method, a conventional solid-state method, and an impregnation method, respectively. The chemicals were listed in Table 3-1.

3.1.2 Sample preparation

3.1.2.1 Cathode preparation

The $LnSr_{3-x}Ca_xFe_{3-y}Ca_yO_{10-\delta}$ with x = 0-1.5; Ln = La, Pr, Sm; B = Ni, Co, Cu; and y = 0-1.5 cathode materials were synthesized by dissolving an appropriate molar ratios of metal nitrate as metal precursors into distilled water at room temperature, then this solution was mixed with citric acid to produce a solution which has a citric acid to metal ion molar ratio of 2 to 1. Subsequently, the obtained solution was stirred for 2 h and dehydrated by heating at 180 °C on a hot plate with continuous stirring until the solution finally became a viscous dark gel. The temperature was raised up to 250 °C to make a complete combustion of the viscous gel until a loose dark ash was formed. The ash was transferred to a box furnace and calcined at 800 °C for 5 h with a heating rate of 200 °C/h in air to remove the remaining hydrocarbon residues and obtain the metal oxide powders. The calcined powders were then manually ground in ethanol and subsequently sintered at 1400 °C for 12 h in air. The sintered powders were re-ground and annealed at 900 °C for 30 min to obtain the high oxygen content in their structure.[99-101]

Table 3-1 Chemicals and reagents in this research

Chemicals and Reagents	Molecular Weight (g/mol)	Purity (%)	Manufacturer
$La(NO_3)_3 \cdot 6H_2O$	433.01	99.9	Nacalai Tesque
$Pr(NO_3)_3 \cdot 6H_2O$	435.01	99.9	Nacalai Tesque
$Sm(NO_3)_2$	444.47	99.5	Wako Pure Chemical
$Sr(NO_3)_2$	211.63	>98	Strem Chemical Incorporated
$Ca(NO_3)_2 \cdot 4H_2O$	236.15	99.99	Nacalai Tesque
$Fe(NO_3)_3 \cdot 9H_2O$	404.00	99	Nacalai Tesque
$Ni(NO_3)_3 \cdot 6H_2O$	290.79	99.95	Wako Pure Chemical
$Co(NO_3)_3 \cdot 6H_2O$	291.03	99	Nacalai Tesque
$Cu(NO_3)_2 \cdot 3H_2O$	241.60	99	Nacalai Tesque
$C_6H_8O_7 \cdot H_2O$	210.14	99.5	Aldrich
La_2O_3	325.81	99.99	Wako
Ga_2O_3	187.44	≥ 99.99	Aldrich
MgO	40.3	≥ 98.0	Fluka
Sm_2O_3	348.70	99.9	Aldrich
NiO	74.69	99	American Elements
NH_4OH	35.05	30	Aldrich

3.1.2.2 Electrolyte preparation

The appropriate molar ratios of La_2O_3, Ga_2O_3, $SrCO_3$, and MgO was homogenously ground and calcined at 1000 °C for 5 hours in air with heating and cooling rate of 200 °C/h. [102] The calcined powder was ground and then uniaxially pressed into a pellet with a diameter of 20 mm by a cold isostatic pressing (CIP) method under pressure of 325 MPa for 30 minutes. The pellets were sintered at 1500 °C for 5 h with a heating rate of 200 °C/h to obtain dense pellets. After cooled down, the sintered pellet was polished and trimmed down to the thickness of 0.3 mm using a diamond grinding machine.

3.1.2.3 Anode preparation

NiO-Fe_2O_3 used as anode material in this research was prepared by an impregnation method. The stoichiometric amount of NiO and $Fe(NO_3)_3 \cdot 9H_2O$ solutions were mixed in the molar ratio of Ni to Fe at 9 to 1. The mixture was stirred for 2 h at room temperature and heated at 180 °C to dryness and then fired at 400 °C for 2 h to eliminate the hydrocarbon. The fired powder was calcined at 1200 °C for 2 h in air with heating and cooling rate of 200 °C/h.

3.2 Physical properties characterization

3.2.1 Structural characterization

All samples were structurally characterized by powder X-ray diffraction (XRD) technique. This measurement was carried out in an X-ray diffractometer (RINT-2200HF, Rigaku) with a monochromated Cu Kα radiation, λ(Kα) = 1.54056 Å, which operated at 40 kV and 30 mA. Diffraction patterns were recorded in the 2θ range of 20° to 90°, with a sampling step of 0.02° and a scan speed of 2°/min under continuous scan mode. The samples were ground into a fine powder before measuring. The diffraction patterns, crystal structures and unit cell parameter (*a* and *c*) of the samples were determined by matching the measured patterns with the database of the

International Centre for Diffraction Data (ICDD) using the MDI/JADE7 software and the results were also used to calculate lattice parameters by Bragg's diffraction law, as equation (3-1).

$$n\lambda = 2d_{hkl}\sin(\theta) \qquad (3\text{-}1)$$

where *n* is 1,2,3... (order of diffraction), d_{hkl} is a distance between adjacent reflection planes (*hkl*) and θ is the angle that X-ray beam hit the reflection plan.

3.2.2 Microstructure characterization

The microstructure of $LnSr_{3-x}Ca_xFe_{3-y}B_yO_{10-\delta}$ (x = 0-1.5; Ln = La, Pr, Sm; B = Ni, Co, Cu; and y = 0-1.5) were observed by a scanning electron microscope (SEM, TM3000 Miniscope, Hitachi) with the acceleration voltage of 15 kV. The Pt was sputtered on the 30-mm thick samples by an auto fine coater (JFC-1600, JEOL) under the applied current of 30 mA for 40 s for 30 min in order to collect the secondary electron that emitted from the sample. The particle sizes of the samples were also roughly analyzed by this technique.

3.2.3 Thermogravimetric analysis

The variation of weight of $LnSr_{3-x}Ca_xFe_{3-y}B_yO_{10-\delta}$ samples during heating and cooling temperature of 30-800 °C, in air were recorded on the thermogravimetric analyzer (Mettler Toledo TGA, SDTA 851).

3.2.4 Thermal expansion measurement

Dilatometer (NETZSCH, DIL 402 PC) was used to measure the thermal expansion behavior of $LnSr_{3-x}Ca_xFe_{3-y}B_yO_{10-\delta}$ samples. A bar-shaped sample with a height of > 2 mm was heated in the temperature range of 25-800 °C in air with a heating rate of 20 °C/min then the change in length along the Z-axis was recorded and compared to the original position. Thermal expansion coefficient (TEC) value of the samples was calculated as equation (3-2).

$$\alpha = \frac{\Delta L}{L_0} \times \frac{1}{T_2 - T_1} \qquad (3\text{-}2)$$

where α represents the TEC value, L_0 represents the length of the sample at an initial temperature, ΔL is a change in sample length at a final temperature, and T_1, T_2 are initial and final temperatures.

3.3 Single cell fabrication and fuel cell set-up consideration

A slurry of $LnSr_{3-x}Ca_xFe_{3-y}B_yO_{10-\delta}$ was prepared by mixing its fired powder with glycerol and several organic additives, such as solvent, dispersing agents, binder, and softener until a homogeneous slurry was obtained. The slurry was then painted as a circle on one face of the LSGM disk, which was used as the electrolyte, by tape casting method to form a thin and flat layer with controlled thicknesses. The Pt mesh and Pt wire as a current collector were welded by a spot welder (USUTANI, mini WELDER UH-1001) and then attached to the top of the painted cathode. This set was heated at 1000 °C for 30 min in air to secure the attachment between the current collector and the cell.

The $NiO-Fe_2O_3$ powder used as an anode was similarly prepared into a slurry as that of $LnSr_{3-x}Ca_xFe_{3-y}B_yO_{10-\delta}$ cathode. The $NiO-Fe_2O_3$ slurry was then painted to another face of the LSGM disk. Another set of welded Pt mesh and Pt wire was also attached to the top of the anode surface and then fired at 1000 °C for 30 min in air. The geometrical area of both anode and cathode was ~0.28 cm^2, as a schematic configuration of the test single cell illustrated in Figure 3-1. Sealing between the single cell and the alumina tube was achieved with a Pyrex glass ring. A setting up of the cell in a furnace and the gas flow system are shown in Figure 3-2 and Figure 3-3, respectively.

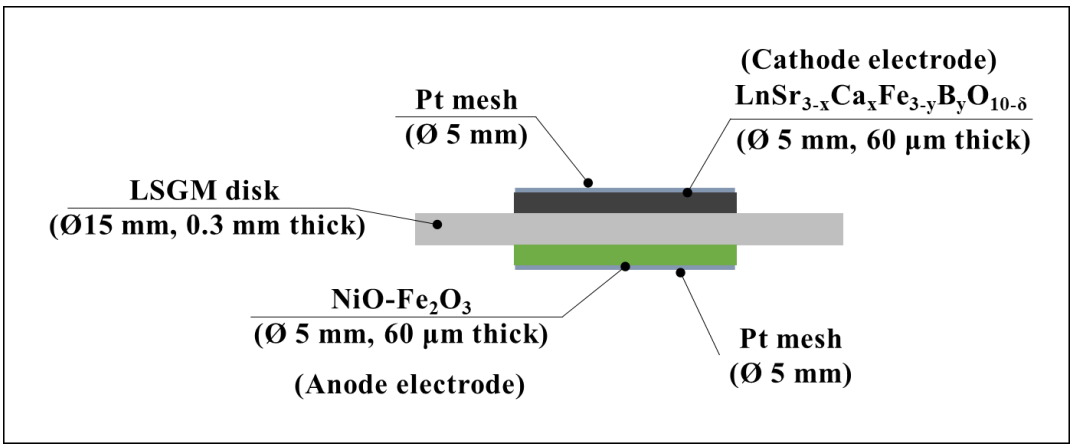

Figure 3-1 A schematic configuration of a single cell

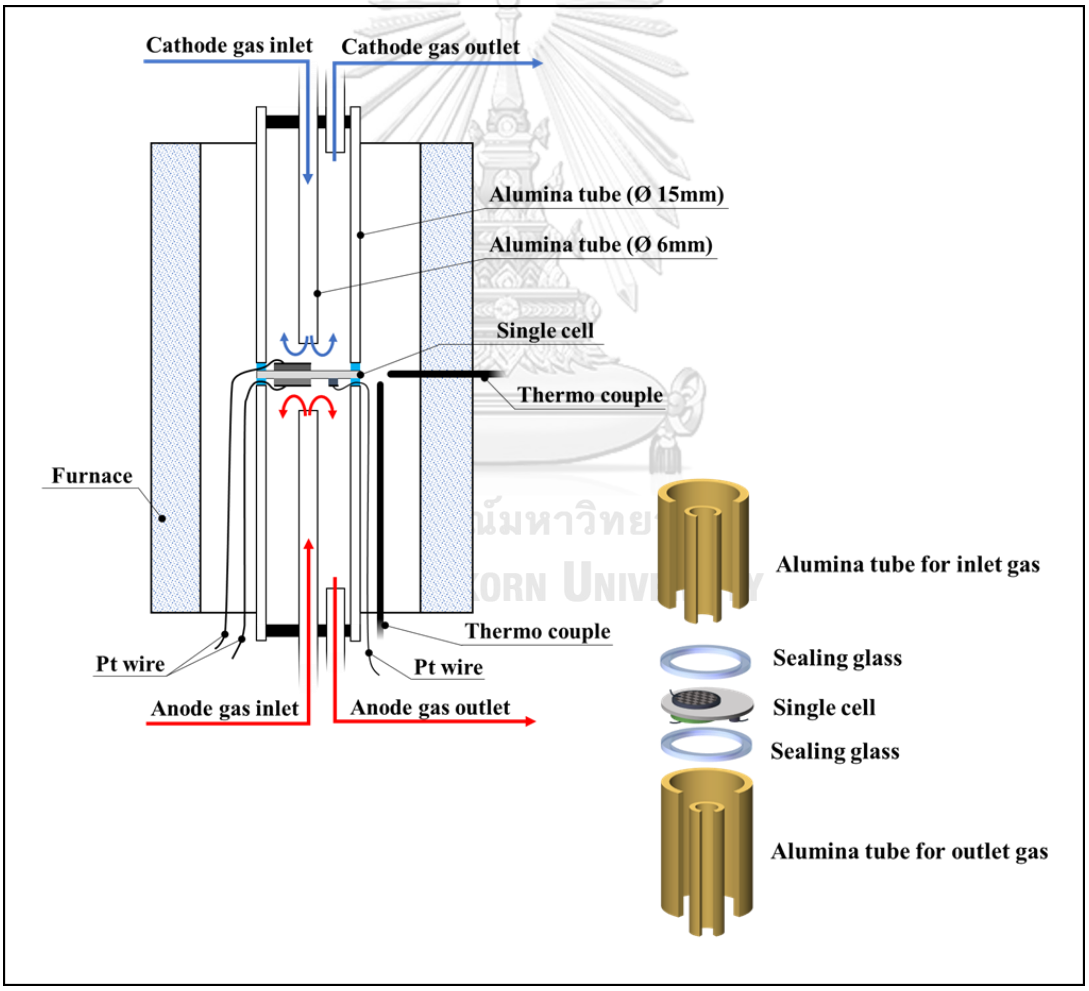

Figure 3-2 Schematic configuration of the single cell test set-up

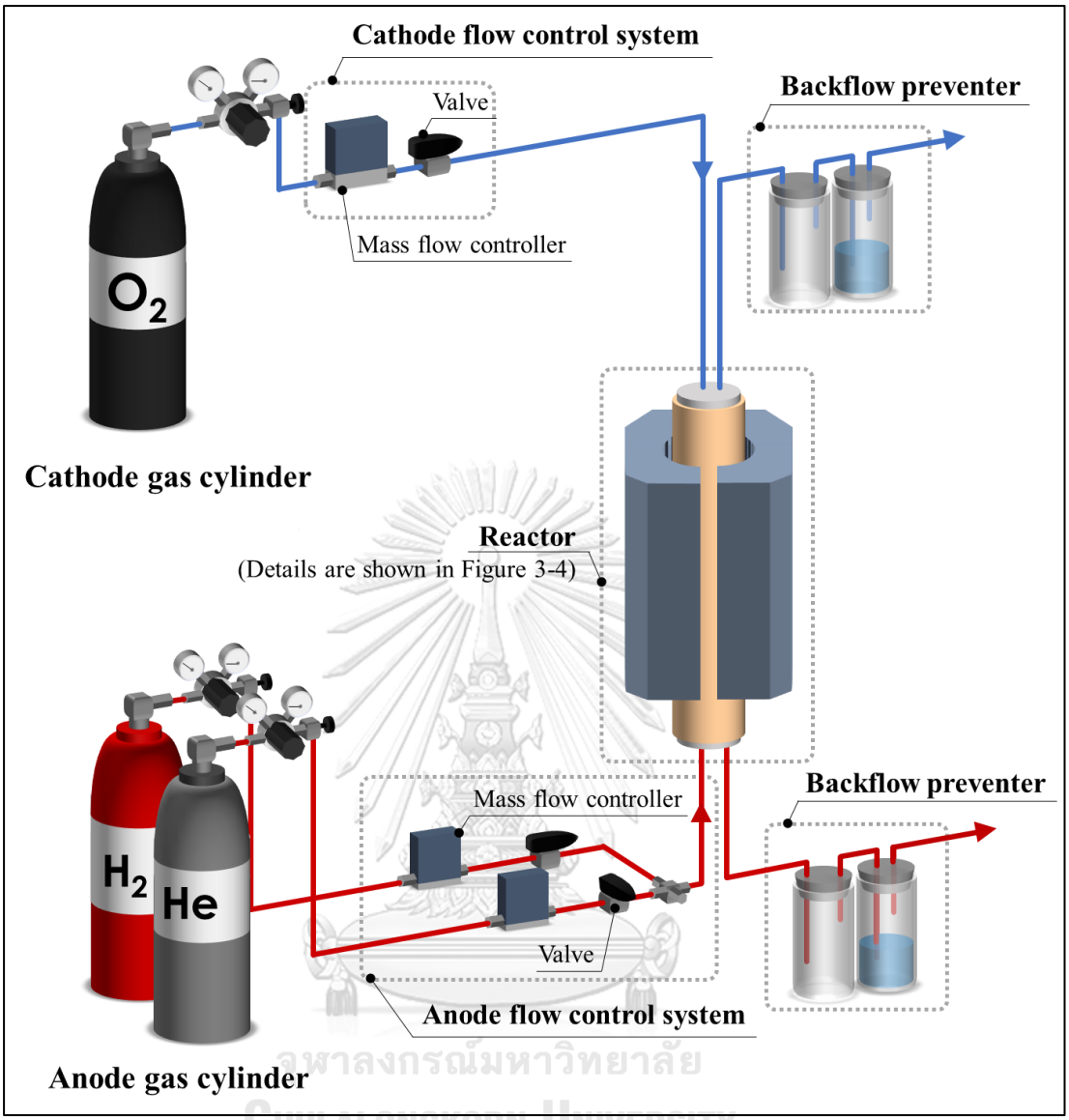

Figure 3-3 SOFC setting schematic

3.4 Electrochemical properties

3.4.1 Total conductivity

Total conductivity measurement was performed with a 4-probe DC method using an Autolab PGSTAT302N potentiostat/galvanostat at 200-800 °C with heating and cooling rate of 200 °C/h in air. The schematic of bar-shape $LnSr_{3-x}Ca_xFe_{3-y}B_yO_{10-\delta}$ samples was shown in Figure 3.4. The total conductivity of the samples was calculated as equation (3-3)

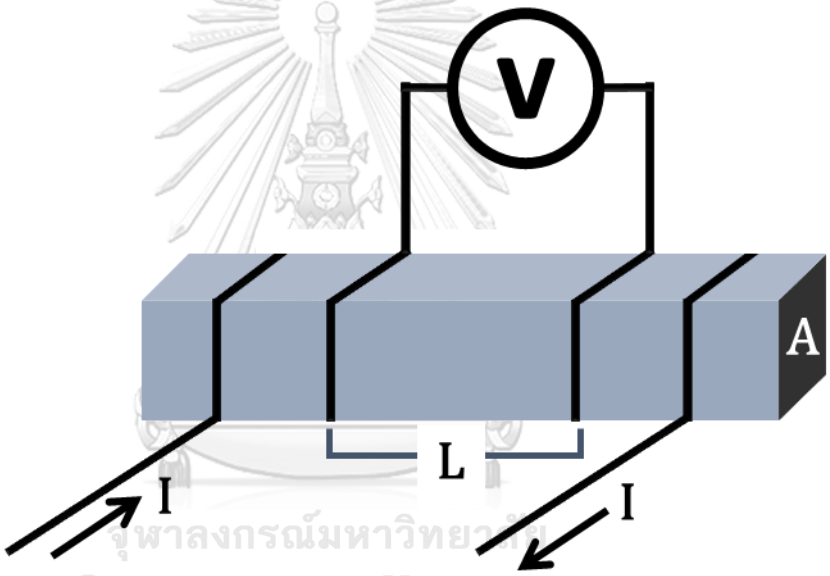

Figure 3-4 Schematic illustration of the DC four – point probe experiment.

$$\sigma = \frac{I}{V} \times \frac{L}{A} \qquad (3\text{-}3)$$

where σ is the total conductivity (S cm^{-1}), I is the applied DC current (A), L is length between voltage probe, and A is the cross-sectional area of the bar-shape sample. The relative density of all sample was larger than 90%, as shown in Appendix, which was high enough for the conductivity test.

3.4.2 Electrochemical performance

The electrochemical performance of the cells for $LnSr_{3-x}Ca_xFe_{3-y}B_yO_{10-\delta}$ cathodes was evaluated from the Current-Voltage (*I-V*) measurement which was carried out with the voltage between the cathode and anode, as shown in Figure 3-5. The cells were sealed to the aluminum tube using a Pyrex glass ring at the sealing temperature of 800 °C. The H_2 and O_2 were supplied to the anode and the cathode component, respectively, at the flow rate of 20 cm^3min^{-1}. Before measuring the cell performance, the $NiO-Fe_2O_3$ anode was reduced to Ni-Fe at this temperature for 1 h and the cell was consequently activated preliminary by passing a certain amount of electric current (preloading) at the load which provided the cell voltage about 0.2 V for 30 min. The cell performance measurement was performed at the operating temperatures of 600-800 °C. During the measurement, the current was applied to the cell by a current pulse generator (NIIKO KEISOKU, NCPG-101) and the voltage was collected by a multimeter mobile corder (YOKOKAWA, MV1000)

3.4.3 Electrode resistance characterization

The area specific resistance (ASR) of the cell was measured at 600-800 °C using a frequency response analyzer (FRA5097) in the frequency range of 0.1 mHz to 1MHz. The results were plotted as Nyquist plot by Frequency Respond Analysis Data Display program.

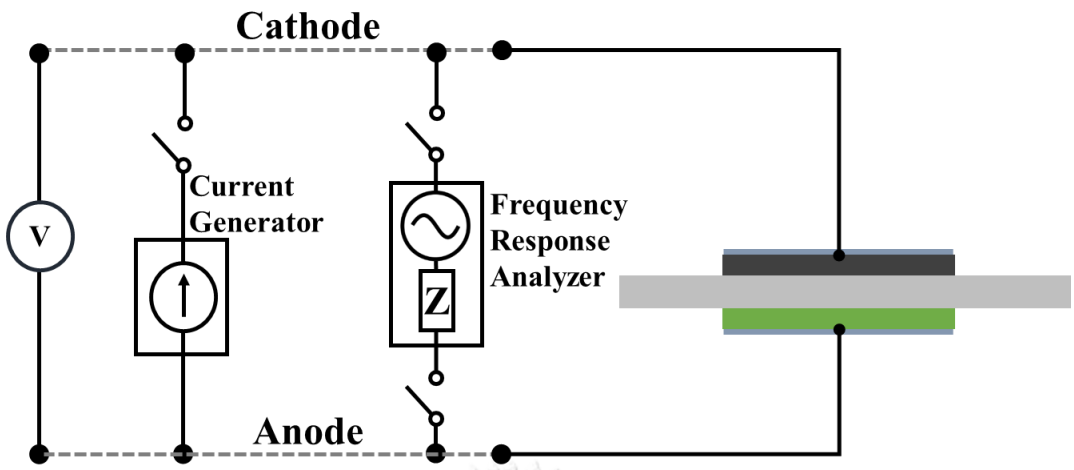

Figure 3-5. Cell equivalent circuit

CHAPTER IV
RESULT AND DISCUSSION

4.1 Effect of Ca substitution for Sr in $LaSr_{3-x}Ca_xFe_3O_{10-\delta}$ Ruddlesden-Popper phase

4.1.1 Crystal structure and phase identification of $LaSr_{3-x}Ca_xFe_3O_{10-\delta}$

XRD patterns of $LaSr_{3-x}Ca_xFe_3O_{10-\delta}$ (x = 0-1.5) after fired at 900 °C were illustrated in Figure 4-1. The XRD patterns of $LaSr_3Fe_3O_{10-\delta}$, Figure 4-1(a), was refined on the basis of tetragonal structure with space group *I4/mmm* phase, which corresponded to $LaSr_3Fe_3O_{9.9}$ (JCPDS no. 81-1234). A small amount of perovskite co-exisiting phase (La,Sr)FeO_3 observed at 2θ of 40.5 degree was corresponded to $La_{0.3}Sr_{0.7}FeO_3$ (JCPDS no. 82-1964). The formation of the co-existing phase was caused by the structural instability of $LaSr_3Fe_3O_{9.9}$ which can decompose to (La,Sr)FeO_3 and (La,Sr)FeO_4 at high temperature (T > 850 °C), according to equation (4-2).[87] However, the phase of (La,Sr)FeO_4 was not found in this study.

$$(La,Sr)_4Fe_3O_{10-\delta_1}(s) \rightarrow (La,Sr)_2FeO_{4-\delta_2}(s) + 2(La,Sr)FeO_{3-\delta_3}(s) + \left(\frac{\delta_2+2\delta_3-\delta_1}{2}\right)O_2\,(g) \qquad (4\text{-}2)$$

With Ca substitution at x = 0-1.0, the RP structure of $LaSr_3Fe_3O_{9.9}$ phase and the perovskite co-existing phase were remained. The ratio of perovskite to the RP structure was calculated using the peak area of 202 lattice plane of perovskite structure and that of 118 lattice plane of RP structure, as shown in Table 4-1. These planes were used for calculation instead of the main diffraction peak of each structure because the main lattice plane of perovskite, 110, was overlapped with the lattice plane of RP, 110. As the result, the amount of perovskite was approximately ~7% in $LaSr_{3-x}Ca_xFe_3O_{10-\delta}$ for x = 0-0.7, whereas the amount of perovskite phase was dramatically increased approximately ~20%, for x = 1.0, suggesting the phase transformation of RP structure. Since the amount of impurity was low for x = 0-0.7, the effect of impurity was possibly

negligible. At the composition of x = 1.5, the diffraction intensity of $LaSr_3Fe_3O_{9.9}$ phase was diminished and the pure perovskite phase only exist, suggesting the RP structure was completely transformed to the perovskite structure. Thus, the limitation of Ca substitution for Sr in $LaSr_3Fe_3O_{10-\delta}$ in this study was approximately x = 0.7. The phase equilibria system of La-Sr-Fe-O reported that the stability of $LaSr_3Fe_3O_{10-\delta}$ depended upon the oxygen loss in the structure which might relate to the material preparation conditions.[84, 88, 103] Thus, the substitution of Ca for Sr in the RP structure would influence the oxygen concentration and instability of $LaSr_{3-x}Ca_xFe_3O_{10-\delta}$.

Table 4-1 Peak area and perovskite to RP ratio in $LaSr_{3-x}Ca_xFe_3O_{10-\delta}$ (x = 0-1.0)

x in $LaSr_{3-x}Ca_xFe_3O_{10-\delta}$	Peak area		Perovskite to RP ratio
	2 0 2 of perovskite	2 1 7 of RP	
0	273	5797	0.05
0.1	465	5639	0.08
0.3	65	4496	0.01
0.5	308	5933	0.05
0.7	401	5360	0.07
1.0	1262	4874	0.26

Upon the increasing of Ca concentration, the diffraction pattern of the RP phase was shifted to the higher angle, Figure 4-1(inset), indicating the contraction of unit cell parameters and the distortion of the RP structure. The lattice parameters, *a* and *c*, and the unit cell volume of $LaSr_{3-x}Ca_xFe_3O_{10-\delta}$ at the composition of x = 0-1.0 were calculated from the lattice plane of 107 using a Scherrer equation, as shown in Figure 4-2(a)-(c). Since $LaSr_{1.5}Ca_{1.5}Fe_3O_{10-\delta}$ (x = 1.5) had the perovskite structure, its

lattice parameters and unit cell volume were not included. The parameter *a* was not significantly different while the parameter *c* and the unit cell volume were decreased with increasing the Ca concentration for $0 \leq x \leq 0.7$, which was due to the small ionic radius of Ca^{2+} (1.34 Å) [104] compared with that of Sr^{2+} (1.44 Å).[104] As a consequence, the bond length between (La, Sr, Ca)–O was decreased, leading to the unit cell distortion along the *a*- or *c*-axis. On the other hand, the increase in parameter *c* in $LaSr_{3-x}Ca_xFe_3O_{10-\delta}$ for x = 1.0 was a result of the phase transformation from the RP structure to perovskite. [105] Since the Ca substituted concentration was limited at x = 0.7, the $LaSr_{3-x}Ca_xFe_3O_{10-\delta}$ with x = 0-0.7 was further investigated.

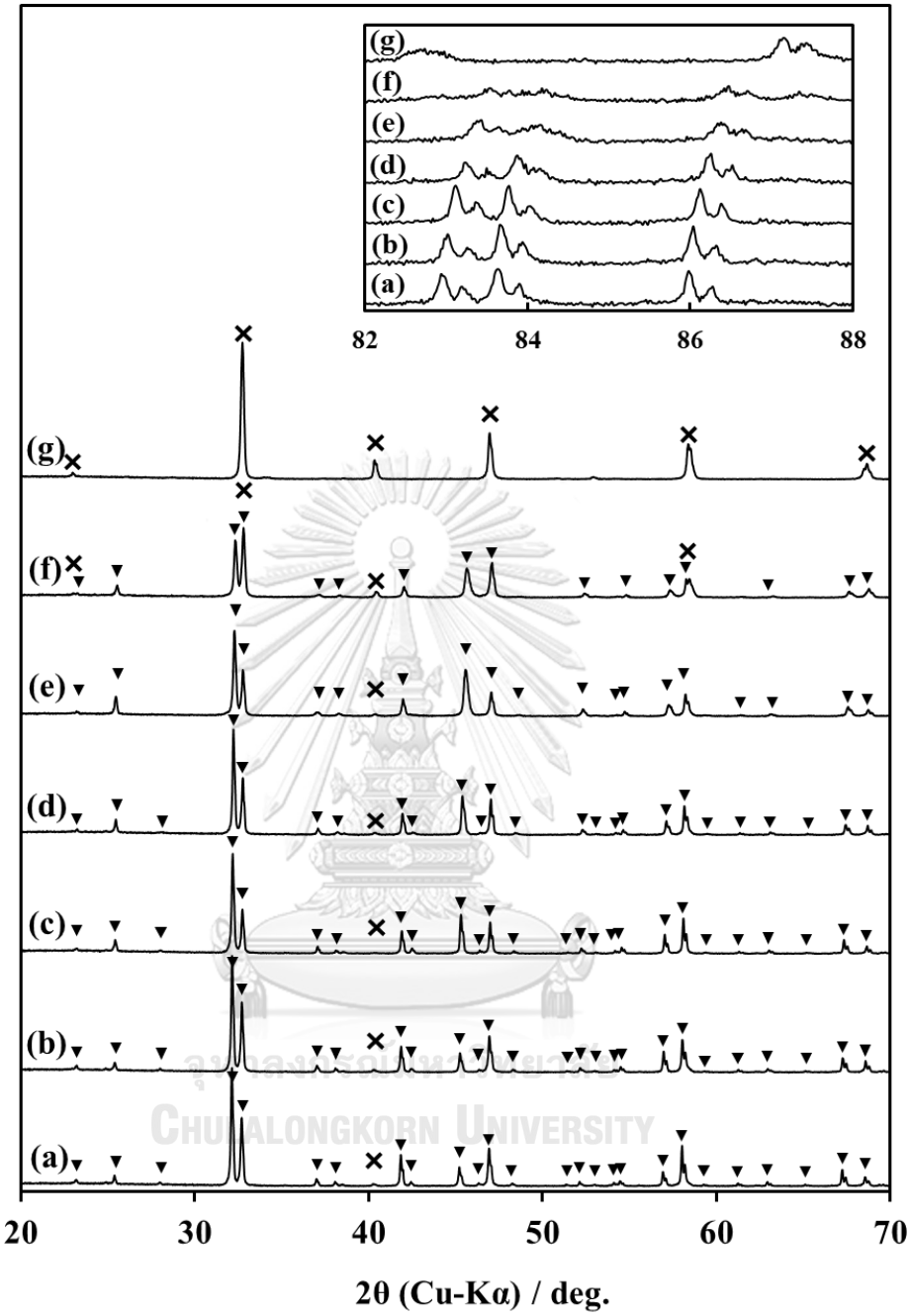

Figure 4-1 XRD pattern of $LaSr_{3-x}Ca_xFe_3O_{10-\delta}$ after sintered at 1400°C for 12 h and annealed at 900°C for 30 min with (▼ = $LaSr_{3-x}Ca_xFe_3O_{9.9}$, and **x** = $(La,Sr)FeO_3$; (a) x = 0, (b) x = 0.1, (c) x = 0.3, (d) x = 0.5, (e) x = 0.7, (f) x = 1.0 and (g) x = 1.5

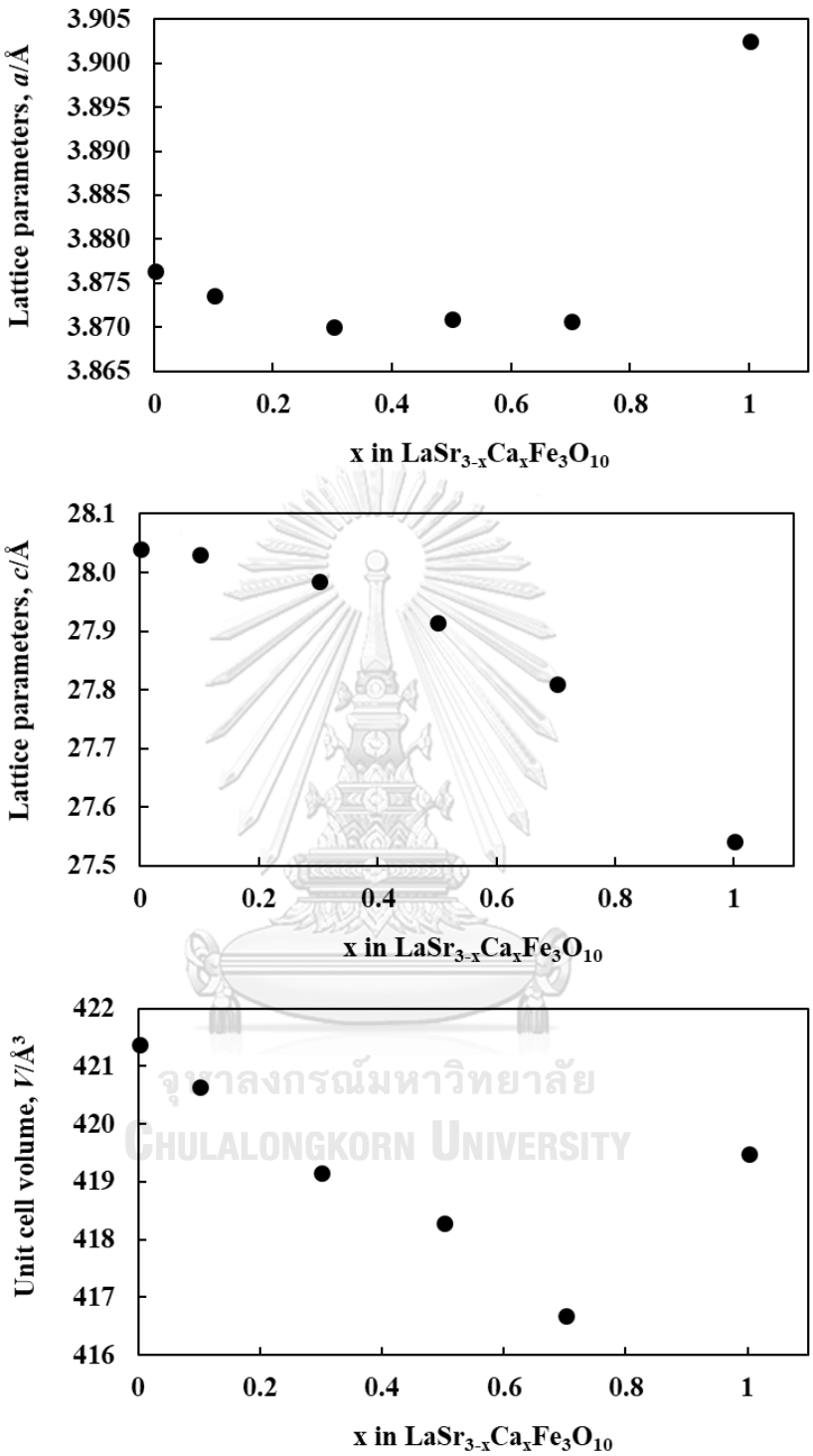

Figure 4-2 (a) Lattice parameter a, (b) and lattice parameters c, and (c) unit cell volume of the $LaSr_{3-x}Ca_xFe_3O_{10-\delta}$ (x = 0-1.0)

4.1.2 TG analysis of $LaSr_{3-x}Ca_xFe_3O_{10-\delta}$

The oxygen losses of $LaSr_{3-x}Ca_xFe_3O_{10-\delta}$ (x = 0-0.7) samples were recorded using a thermal gravimetric analyzer in air at 25-800 °C as presented in Figure 4-3. All samples showed a similar trend of thermogram in the variation of weight decreasing with increasing temperature. The loss in humidity was found in the samples in the temperatures between 100-200 °C and the weight continuously decreased as increasing temperature from 200-400 °C which corresponded to the loss of surface oxygen. Above 400 °C, a drastically decreasing of weight loss was assigned to the oxygen loss from the bulk of the structure.[106] The total weight loss of each sample was approximately 2% which was similar to the weight loss of $LaSr_3Fe_3O_{10-\delta}$ report by Kim *et al.*,.[89]

At low Ca concentration (x = 0-0.3), the weight loss was decreased with increasing Ca concentration,while at higher Ca concentration (x ≥ 0.5), the weight loss turned to increase.. This result implied that the low concentration of Casubstitution reduced the oxygen vacancy in the $LaSr_3Fe_3O_{10-\delta}$ structure. Generally, the substitution of the same valence state ion had no effect on the charge of the composition. However, in this case, since Ca had small ionic radii and caused the contraction of the unit cell, the interaction between metal and oxygen bond was possibly strenghten, resulted in a decrease of oxygen loss, similar to the work reported by Choi *et al.* [107], who investigated the effect of Ca doped for Sr in $PrBa_{0.5}Sr_{0.5-x}Ca_xCo_2O_{5+\delta}$ layered perovskite oxides. They found that Ca substitution increased oxygen concentration and enhanced the conductivity of $PrBa_{0.5}Sr_{0.5}Co_2O_{5+\delta}$ because the difference in size between Ca^{2+} and Pr^{3+} was smaller than that between Sr^{2+} and Pr^{3+}, resulting in a stronger interaction between the metal-O bond and consequently leading to the decreasing of oxygen loss. For higher Ca content (x ≥ 0.5), $LaSr_{2.5}Ca_{0.5}Fe_3O_{10-\delta}$ provided higher weight loss than $LaSr_{2.7}Ca_{0.3}Fe_3O_{10-\delta}$, because the unit cell was highly distorted by the moderated Ca addition which caused the weak interaction between metal-O bond and create more oxygen loss. Manthiram *et al*. also reported the effect of *A*-site size of $Ln_{1-x}Sr_xCoO_{3-\delta}$ (Ln = La, Pr, Nd, Sm, and Gd) perovskite and found that with

decreasing ionic radius from La^{3+} to Gd^{3+}, the O-Co-O bond angle was more lowerthan 180° and the elimination of oxygen in the structure was increased.[108]

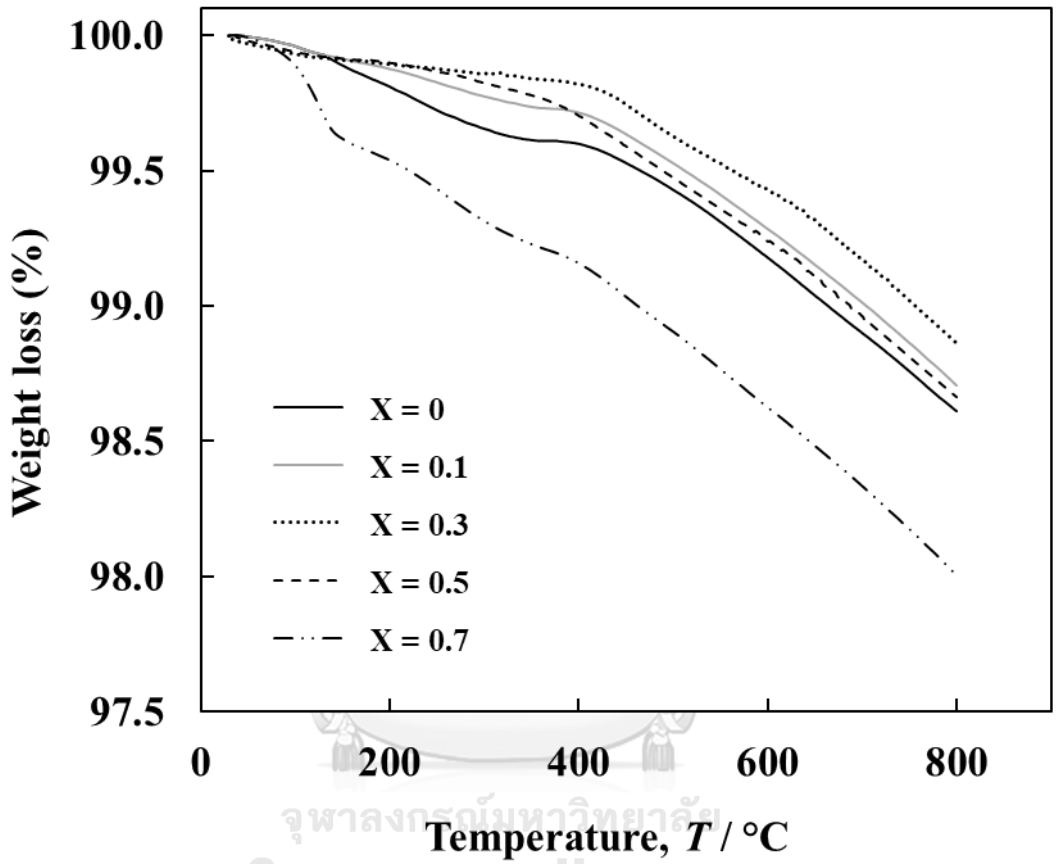

Figure 4-3 TGA plots of $LaSr_{3-x}Ca_xFe_3O_{10-\delta}$ *(x = 0-0.7)* measured in air at 25-800 °C.

4.1.3 Total conductivity of $LaSr_{3-x}Ca_xFe_3O_{10-\delta}$

The total conductivities of $LaSr_{3-x}Ca_xFe_3O_{10-\delta}$ (x = 0 - 0.7) samples were investigated in air at 200-800 °C. At low temperature (T ≤ 400 °C), the conductivities of all samples shown in Figure 4-4 were increased gradually with increasing temperature, which indicated a semiconducting behavior. At high temperature (T > 400 °C), the conductivity was decreased with increasing temperature due to the oxygen loss generated in the structure. The oxygen vacancies generated would decrease the charge carrier concentration and perturb the electron localization between Fe-O-Fe, resulting in a drop of conductivity.[98, 106, 109]

At low Ca content (x = 0-0.3), the conductivity was promoted with increasing the Ca concentration in $LaSr_{3-x}Ca_xFe_3O_{10-\delta}$ and the highest total conductivity was achieved at the composition of $LaSr_{2.7}Ca_{0.3}Fe_3O_{10-\delta}$ (180 Scm^{-1} at 400 °C). In the RP structure, the electronic conductivity was generally explained by the mechanism of small-polaron hoping in the perovskite layer along the Fe^{4+}-O-Fe^{3+} bonds, which Fe^{4+} acted as the charge carrier with electron holes. The substitution of Ca decreased the metal–O bond length, increased the interaction between metal–O bond and possibly reduced the formation of oxygen vacancies in the RP structure, as the TGA result. Thus, the conductivity was promoted by the small amount of Ca substitution.

Conversely, the conductivity turned to decrease with a high Ca content of x ≥ 0.5 because the high amount of Ca substitution caused highly distortion of the unit cell structure, which was possibly undesirable for the overlapping between the metal-O bond and thus provided an adverse effect on the electronic transportation between the Fe-O-Fe bond.[85] In addition, to maintain the RP structure, the oxygen atoms were eliminated and oxygen vacancies were formed. These oxygen vacancies possibly reduced Fe^{4+} to Fe^{3+}, resulting in a decrease of charge-carrier concentration and subsequently reduced the electronic conductivity.[109] These conductivity results were well-agreement with the weight loss from the TGA studied

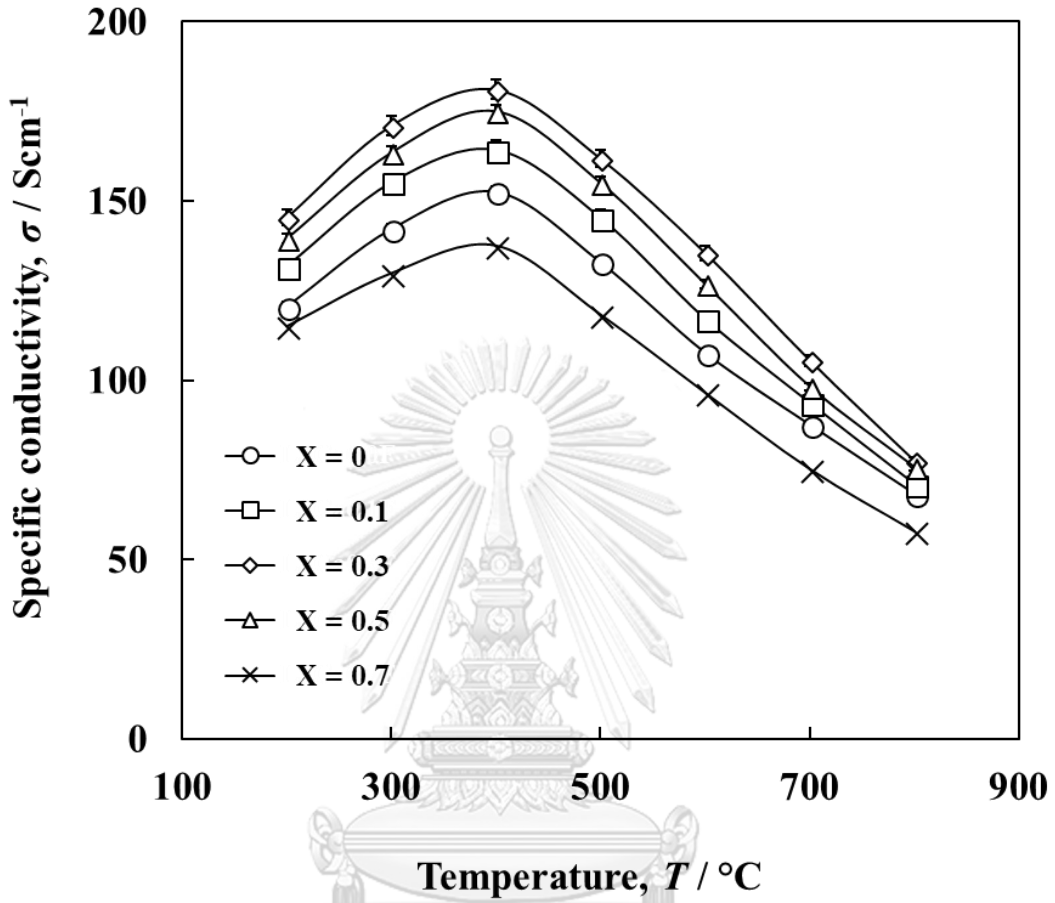

Figure 4-4 The total conductivity of $LaSr_{3-x}Ca_xFe_3O_{10-\delta}$ (x = 0-0.7) at 200-800 °C in air

4.1.4 Microstructure of $LaSr_{3-x}Ca_xFe_3O_{10-\delta}$

The microstructure of $LaSr_{3-x}Ca_xFe_3O_{10-\delta}$ (x = 0-0.7) after coating on the LSGM electrolyte and firing at 1000 °C in air was observed. The SEM images of crossed section of $LaSr_{3-x}Ca_xFe_3O_{10-\delta}$ cathodes were illustrated in Figure 4-5. The bottom part of the micrographs represented a dense area of LSGM electrolyte while the upper

portion showed the porous area of $LaSr_{3-x}Ca_xFe_3O_{10-\delta}$ cathode and a well-coated cathode on electrolyte without delamination along the interlayer. All sample showed no significantly difference in microstructure and particle size of each sample. The samples were homogeneous and the average particle size was approximately 5-7 μm., Thus, the electrochemical performance of the cell was not affected by the microstructure of materials.

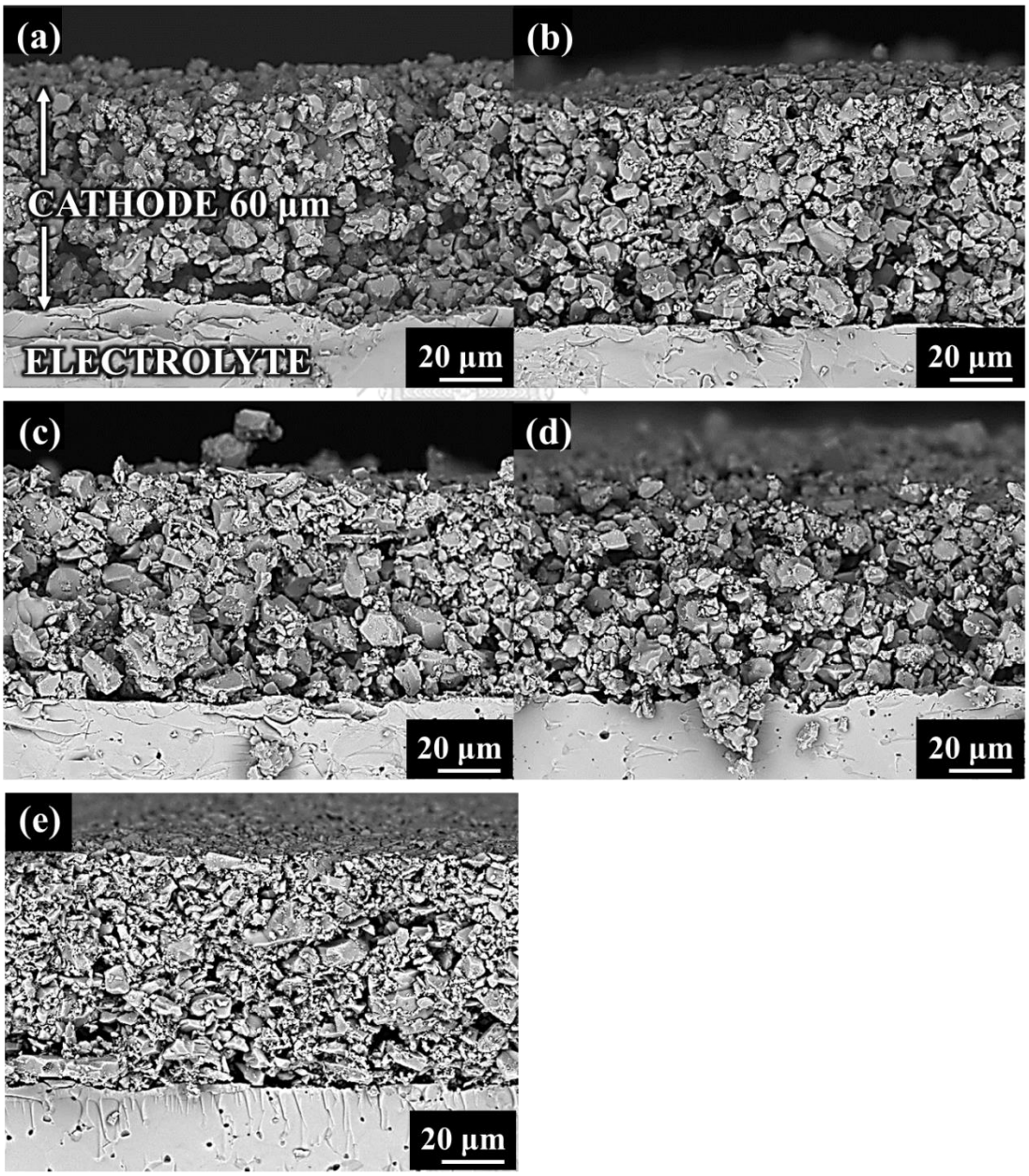

Figure 4-5 SEM images of crossed section of $LaSr_{3-x}Ca_xFe_3O_{10-\delta}$: *(a)* x = 0, *(b)* x = 0.1, *(c)* x = 0.3, *(d)* x = 0.5, and (e) x = 0.7

4.1.5 Thermal expansion behavior of $LaSr_{3-x}Ca_xFe_3O_{10-\delta}$

Figure 4-6 exhibited thermal expansion behaviors of the $LaSr_{3-x}Ca_xFe_3O_{10-\delta}$ (x = 0-0.7) specimens investigated in the temperature range of 25-800 °C in air. All samples showed a linear degree of thermal expansion ($\Delta L/L_0$) at temperature lower than 400 °C, which indicates the oxygen loss was negligible.[110] At higher temperature (T>400 °C), the slopes were non-linearly increased due to the loss of oxygen atomes from the lattice.[98] When the temperature increased, the bond energy was increased and caused the increasing of bond length between Ln-O and Fe-O bond, which resulted the reduction in the bond interaction between metal and oxygen. With weaker bond interaction, the oxygen was easily eliminated and the lattice was easily expanded.[111] Table 4-2 showed the calculated average thermal expansion coefficient (TEC) values of $LaSr_{3-x}Ca_xFe_3O_{10-\delta}$ (x = 0-0.7) at two different temperature ranges, 25-400 °C (low temperature) and 400–800 °C (high temperature). At both temperature ranges, the TEC value of $LaCaSr_3Fe_3O_{10-\delta}$ was decreased and provided the lowest value at the composition of x = 0.3, which was closed to that of LSGM electrolyte (18.82 x $10^{-6}K^{-1}$ at 25-800 °C). The lower in TEC value could be explained by the lower in oxygen loss of Ca-doped samples compared to the undoped sample. Thus, the structure was tightly bonded and not much expanded compared to the loosely bonded structure. In addition, the shorter the bond length, the higher the bonding energy was, which could be lowering the TEC value.[112] As a consequence, the smaller unit cell of Ca addition provided the high bond energy and the low TEC value. However, the TEC value was increased with the Ca addition at x ≥ 0.5, which was due to the greater amount of oxygen loss in the structure of composition x ≥ 0.5. The increasing of oxygen vacancy caused the decrease in total negative charge of the

lattice, resulting that the Fe was oxidized from 3+ to 4+ and/or 3+ to 2+ to compensate the charge and caused the lowering of electrostatic attraction of Fe-O bond, resulting in increased the TEC value.[98]

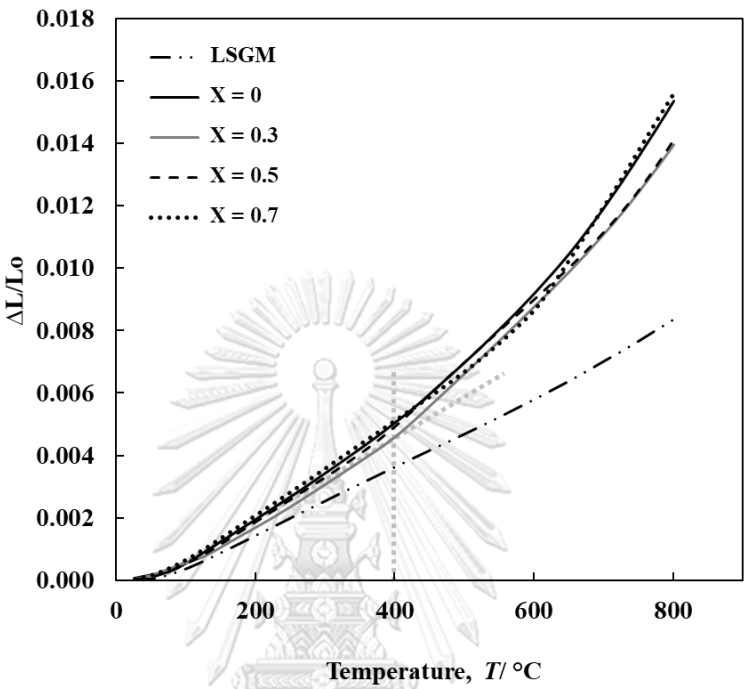

Figure 4-6 Thermal expansion ($\Delta L/L_o$) curves of $LaSr_{3-x}Ca_xFe_3O_{10-\delta}$ (x = 0-0.7) in air at 25-800 °C

Table 4- 2 Average TECs of $LaSr_{3-x}Ca_xFe_3O_{10-\delta}$ (x = 0-0.7) in air at 25–800 °C

x in $LaSr_{3-x}Ca_xFe_3O_{10-\delta}$	TEC^a ($10^{-6}K^{-1}$)	
	25-400 °C	400-800 °C
0	13.47	38.44
0.3	12.24	34.92
0.5	13.19	35.59
0.7	13.66	44.66

4.1.6 X–ray Photoelectron Spectroscopy (XPS) of $LaSr_{3-x}Ca_xFe_3O_{10-\delta}$

4.1.6.1 Calcium spectra in $LaSr_{3-x}Ca_xFe_3O_{10-\delta}$

The deconvolution of Ca 2*p* core level of $LaSr_{3-x}Ca_xFe_3O_{10-\delta}$ (x = 0, 0.3 and 0.5) samples was exhibited in Figure 4-7. The band spectra of 2*p* core level was splitting into two peaks at the binding energies of 345.7 eV and 349.2 eV, which were assigned to Ca 2*p* 1/2 and Ca 2*p* 3/2, respectively. The splitting was the effect of spin-orbit splitting, which showed the energy separation approximately 3.5 eV.[113, 114] The peak area was increased with the increasing of Ca concentration.

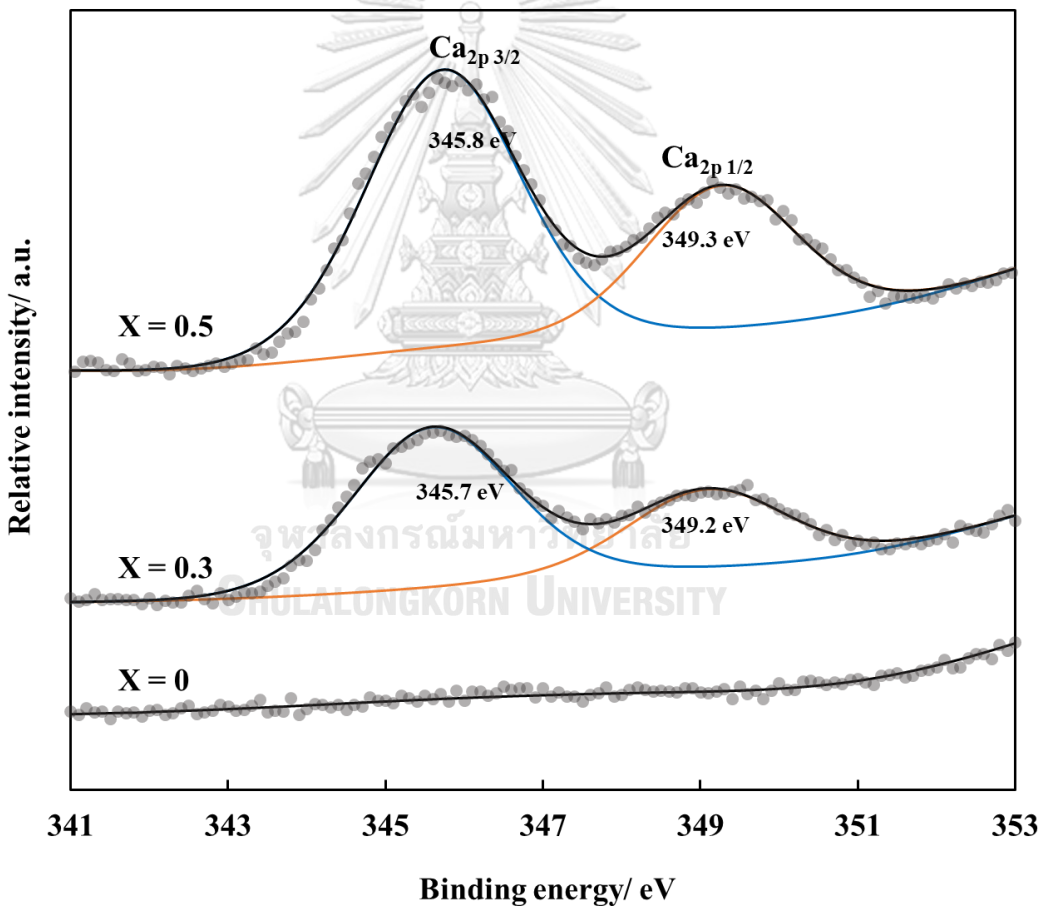

Figure 4-7 XPS spectra of Ca 2p core – level of $LaSr_{3-x}Ca_xFe_3O_{10-\delta}$ *(x = 0, 0.3 and 0.5)*

4.1.6.2 Iron spectra in $LaSr_{3-x}Ca_xFe_3O_{10-\delta}$

The deconvolution of Fe 2*p* core level of $LaSr_{3-x}Ca_xFe_3O_{10-\delta}$ (x = 0, 0.3 and 0.5) samples were split into two peaks of 2*p* 3/2 and 2*p* 1/2, as illustrated in Figure 4-8. Both peaks were shifted to higher binding energy with increasing of Ca concentration, indicating the strong interaction between the Fe-O bond. The deconvolution of each 2*p* core level showed three main signals assigned to Fe^{2+}, Fe^{3+}, and Fe^{4+}. The peaks with the binding energy of ~708, ~709.2 and ~711.5 eV were associated with Fe^{2+} 2*p* 3/2, Fe^{3+} 2*p* 3/2 and Fe^{4+} 2*p* 3/2 while the peaks at binding energy about ~721.5, ~722.6 and 723.9 eV were associated with Fe^{2+} 2*p* 1/2, Fe^{3+} 2*p* 1/2 and Fe^{4+} 2*p* 1/2, respectively.[115-117] The oxidation state of Fe ion in $LaSr_{3-x}Ca_xFe_3O_{10-\delta}$ was mixed valence state of Fe^{3+} and Fe^{4+}, and the Fe^{2+} ion was formed due to the defect of oxygen vacancy in the structure which induced the reduction of Fe.[98, 107, 118, 119] The formation of oxygen vacancies and the reduction of Fe ion in $LaSr_{3-x}Ca_xFe_3O_{10-\delta}$ can be written based on Kröger-Vink notation as follows:[120, 121]

$$2Fe_{Fe}^{\cdot} + O_O^{\times} \leftrightarrow 2Fe_{Fe}^{\times} + V_O^{\cdot\cdot} + \frac{1}{2}O_2 \qquad (4\text{-}1)$$

where $V_O^{\cdot\cdot}$ was the oxygen vacancy and $O_O^{\times}$ was the oxygen in lattice.

The percentage for each chemical state of Fe 2*p* in $LaSr_{3-x}Ca_xFe_3O_{10-\delta}$ was calculated from the peak area and summarized in Table 4-3, Upon increasing the Ca concentration, the percentage of Fe^{2+} was slightly decreased but Fe^{3+} was slightly increased, while that of Fe^{4+} was almost constant. This result implied that the reduction of Fe^{3+} to Fe^{2+} was increased due to the charge compensate caused by the increase of oxygen concentration in the structure.

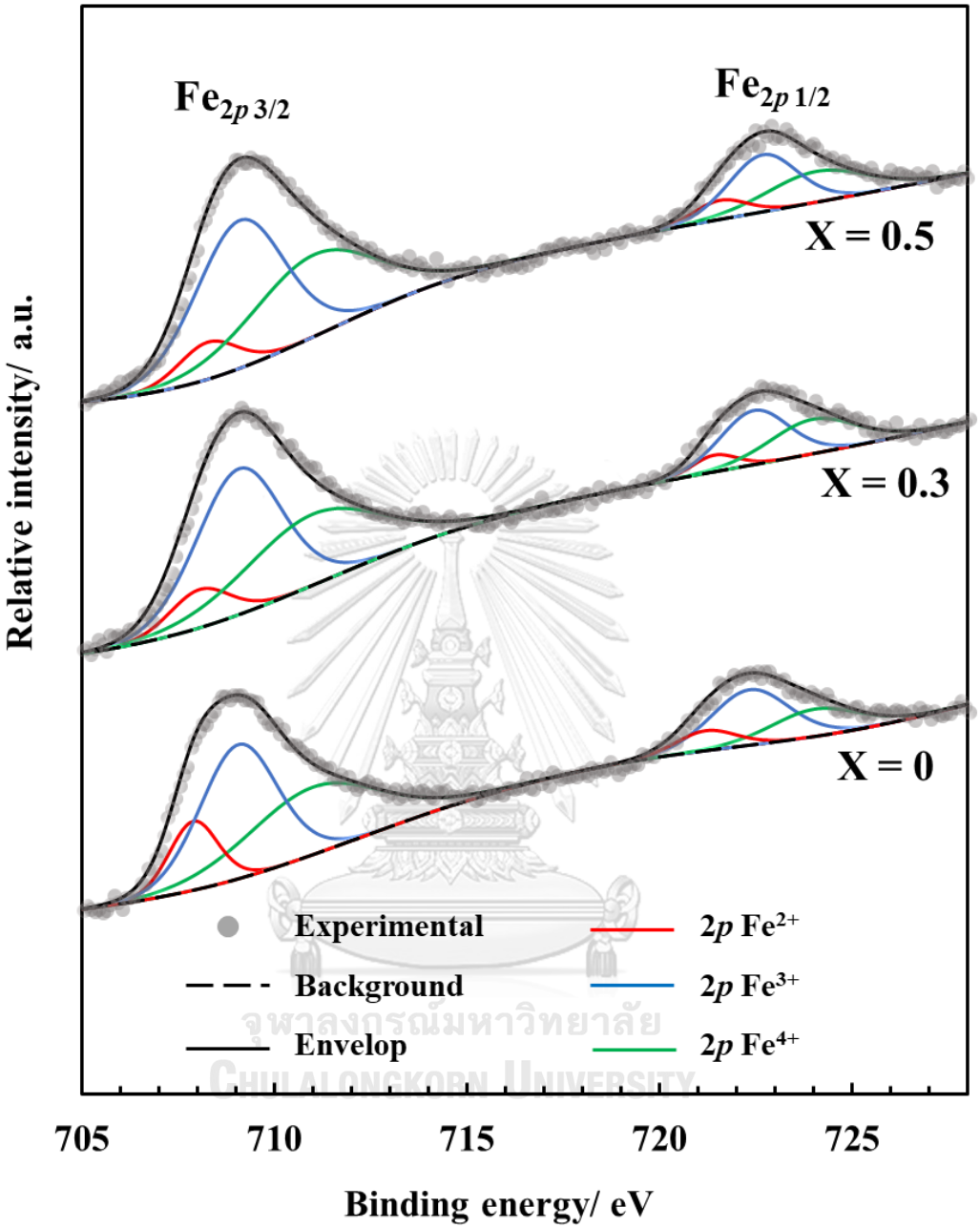

Figure 4-8 XPS spectra of Fe 2p core – level spectra in $LaSr_{3-x}Ca_xFe_3O_{10-\delta}$ (x = 0, 0.3 and 0.5).

Table 4- 3 Percentage for each chemical state of Fe 2p in $LaSr_{3-x}Ca_xFe_3O_{10-\delta}$ *(x = 0, 0.3 and 0.5).*

Oxidation State	x in $LaSr_{3-x}Ca_xFe_3O_{10-\delta}$		
	0	**0.3**	**0.5**
Fe^{2+}	14.75	9.63	10.67
Fe^{3+}	45.82	50.82	49.91
Fe^{4+}	39.43	39.55	39.41

4.1.7 Electrochemical performance of $LaSr_{3-x}Ca_xFe_3O_{10-\delta}$

4.1.7.1 Single cell performance for $LaSr_{3-x}Ca_xFe_3O_{10-\delta}$ cathode

The electrochemical performance of cells using $LaSr_{3-x}Ca_xFe_3O_{10-\delta}$ (x = 0-0.7) cathodes were performed in 3% humidified H_2 fuel. The terminal voltage and power density as a function of current density (*I-V-P* curve) were collected using a potentiostatic measurement at 600-800 °C. As considering *I-V* curve (Figure 4-9(a)), all cells exhibited the distinction between the activation polarization range at a low current density (below 10 $mA \cdot cm^{-2}$) and the ohmic polarization range at medium to high current density (above 10 $mA \cdot cm^{-2}$) while the concentration polarization was not observed.

With increasing of Ca addition, the slope of activation polarization (Figure 4-9(a) (inset)) and ohmic polarization of $LaSr_{3-x}Ca_xFe_3O_{10-\delta}$ (Figure 4-9(a)) were slightly decreased, suggested that the kinetics of the electrochemical reaction and the electrical and ionic transportation of the cells increased by the Ca addition. Since the single cell fabrication was identically prepared and the electrolyte and anode polarization resistances of the cell were assumed to be constant, the resistances of the cells were dominated from the cathodes. Thus, it could be

concluded that the Ca substitution improved the catalytic activity of the $LaSr_3Fe_3O_{10-\delta}$ cathode. The power density of the cell for Ca-free cathode (Figure 4-9(b)), $LaSr_3Fe_3O_{10-\delta}$, (227 $mWcm^{-2}$), was improved by Ca substitution and the highest power density was achieved at the composition of x = 0.3 (301 $mWcm^{-2}$). However, the power density of the cell of Ca concentration of x ≥ 0.5 was decreased from that of $LaSr_{0.7}Ca_{0.3}Fe_3O_{10-\delta}$ cathode.

The effect of temperature on the electrochemical performance was also investigated. All single cells for $LaSr_{3-x}Ca_xFe_3O_{10-\delta}$ cathodes provided the decrease in electrochemical performance with decreasing operating temperature because the ORR decreased at low temperature..[6] The terminal voltage and power density as a function of current density of the cell using $LaSr_{2.7}Ca_{0.3}Fe_3O_{10-\delta}$ cathode was selectively represented in Figure 4-10 and the maximum power densities of the single cells for $LaSr_{3-x}Ca_xFe_3O_{10-\delta}$ (x = 0-0.7) cathodes were summarized in Table 4-4. The electrochemical performance was affected by the operating temperature.

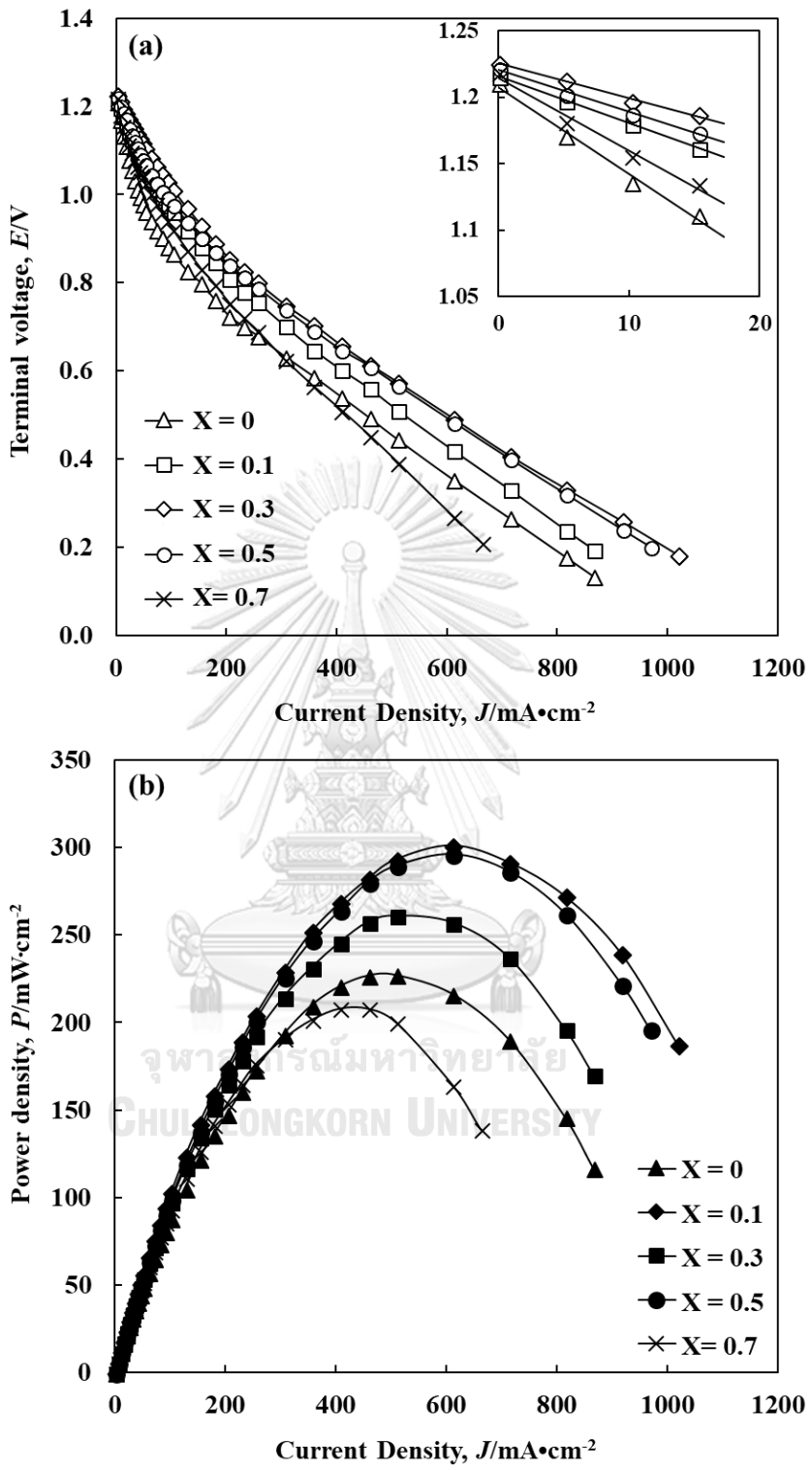

Figure 4-9 *(a)* Terminal voltage and *(b)* power densities as a function of current density of the $LaSr_{3-x}Ca_xFe_3O_{10-\delta}$ *(x = 0-0.7)* cathodes at 800 °C.

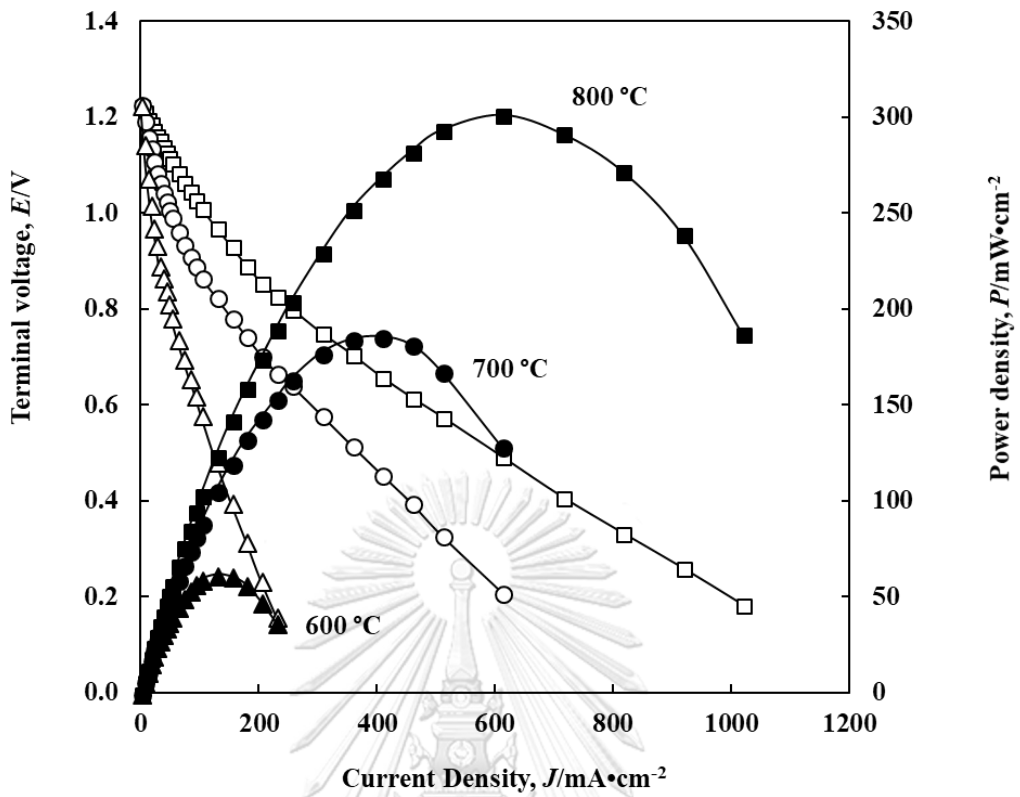

Figure 4-10 Terminal voltage *(open symbols)* and power densities *(closed symbols)* as a function of current density of the $LaSr_{2.7}Ca_{0.3}Fe_3O_{10-\delta}$ cathodes at 600-800 °C.

Table 4- 4 The maximum power density of the single cells for the $LaSr_{3-x}Ca_xFe_3O_{10-\delta}$ cathodes *(x = 0-0.7)* at 600-800 °C in H_2 fuel.

x in $LaSr_{3-x}Ca_xFe_3O_{10-\delta}$	Maximum Powder density ($mW \cdot cm^{-2}$)		
	800 °C	700 °C	600 °C
0	227	102	34
0.1	261	134	43
0.3	301	186	61
0.5	296	188	64
0.7	208	142	49

4.1.7.2 Resistance of the single cells for $LaSr_{3-x}Ca_xFe_3O_{10-\delta}$ cathode

To investigated the resistance of the cell, the impedance spectra of single cells for $LaSr_{3-x}Ca_xFe_3O_{10-\delta}$ cathodes (x = 0-0.7) were analyzed in the temperature range of 600-800 °C. The impedance spectra of the cell for $LaSr_{3-x}Ca_xFe_3O_{10-\delta}$ cathodes showed the similar trend in various operating temperature. Therefore, only the spectra at 800 °C was demonstrated in Figure 4-11 in order to compare the effect of Ca substitution in $LaSr_{3-x}Ca_xFe_3O_{10-\delta}$. The difference between the two intercepts at the real axis, Re(Z), of the semicircle at high frequency and low frequency were the area specific resistance (ASR) of the cell. Generally, several semicircles of impedance could be observed, corresponded to the several reactions on the surface of the electrodes, such as gas dissociation (surface activity) and bulk diffusion, which related to the ionic and electronic conductivity of the electrodes. For roughly observation, there are two semicircles, belonged to the cathode (at lower frequency) and the anode (at higher frequency). Since the single cell fabrication was identically prepared, the ohmic and anodic polarization resistance of the cells were thus assumed to be constant and the resistance of the cells was dominated from the cathodes. In this case, the particle size of the $LaSr_{3-x}Ca_xFe_3O_{10-\delta}$ cathodes was not significantly different, as the SEM result, therefore the gas diffusion to the cathode should not significantly different. Thus, the minimize ASR was depended on the oxidation reduction reaction (ORR) of cathode, which was considerate as the oxidation of oxygen molecule (surface exchange), oxide ion diffusion in cathode bulk, and electron transportation, which depended on the Ca concentration substituted in $LaSr_{3-x}Ca_xFe_3O_{10-\delta}$ cathodes.

With increasing Ca concentration, the ASR decreased and the lowest value was observed for the composition of x = 0.3. The lower the ASR values, the higher the cell performance obtained. In this study, the resistance of the $LaSr_{2.7}Ca_{0.3}Fe_3O_{10-\delta}$ cathode was the lowest, whichwas accorded with the increase in total conductivity as discussed in the previous section. The increasing of conductivity facilitated the electron transformation, the oxidation of oxygen molecules to oxide ions, equation (2-2), and decreased ASR. Compared to the composition of x = 0.3, the

ASR value of the composition of x = 0.5 was slightly increasedbecause the conductivity of $LaSr_{2.5}Ca_{0.5}Fe_3O_{10-\delta}$ was slightly reduced. A slightly drop of conductivity possibly obstructed the electron migration, retarded the ORR and raised the resistance of the cell. For the composition of x = 0.7, the ASR was dramatically increased implied that the rate of ORR was decreased as a result poor conductivity. Even the oxygen vacancy could promote the oxide ion migration, too high oxygen vacancy in Ca content x = 0.7 could also blocked the electron transformation, resulting in high ASR. Therefore, the proper concentration of oxygen vacancies in $LaSr_{3-x}Ca_xFe_3O_{10-\delta}$ could be controlled by the proper amount of Ca substitution to facilitate both oxide and electron transportation, minimize the ASR and promote cell performance.

At various temperatures, the impedance spectra of all samples showed the increase in ASR with reducing temperature because the kinetics of the electrochemical reaction and ionic transportation of the cells were reduced with decreasing temperature.[6] Figure 4-12 showed the impedance spectra of $LaSr_{2.7}Ca_{0.3}Fe_3O_{10-\delta}$. The ASR value of $LaSr_{3-x}Ca_xFe_3O_{10-\delta}$ (x = 0-0.7) at different operating temperatures was summarized in Table 4-5.

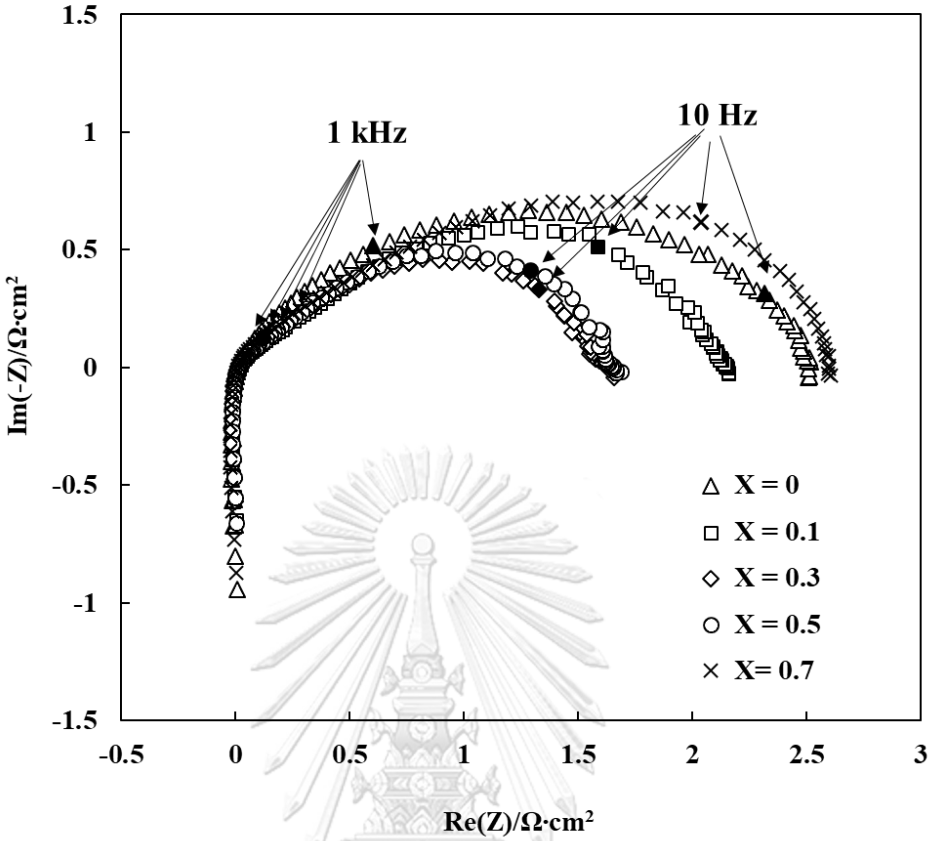

Figure 4-11 Impedance spectra of the $LaSr_{3-x}Ca_xFe_3O_{10-\delta}$ (x = 0-0.7) cathodes at 800 °C.

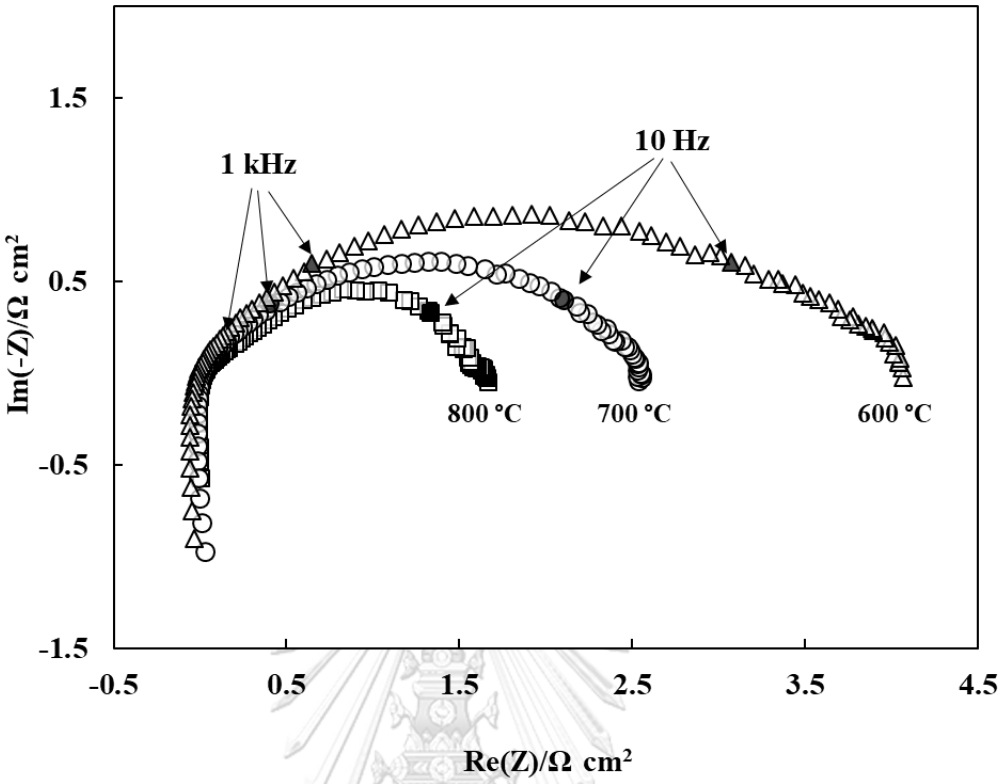

Figure 4-12 Impedance spectra of the cell for $LaSr_{2.7}Ca_{0.3}Fe_3O_{10-\delta}$ (x = 0-0.7) cathodes at 600-800 °C.

Table 4- 5ASR of the single cells for the $LaSr_{3-x}Ca_xFe_3O_{10-\delta}$ cathodes *(x = 0-0.7)* at 600-800 °C in H_2 fuel.

x in $LaSr_{3-x}Ca_xFe_3O_{10-\delta}$	Area specific resistance, ASR (Ω cm^2)		
	800 °C	700 °C	600 °C
0	2.50	2.95	99.57
0.1	2.15	2.93	133.69
0.3	1.64	2.54	161.19
0.5	1.66	2.56	165.78

4.2 Effect of lanthanide ion in $LnSr_{2.7}Ca_{0.3}Fe_3O_{10-\delta}$ (Ln = La, Pr, and Sm) Ruddlesden-Popper phases as Cathodes for Intermediate Temperature Solid Oxide Fuel Cells

4.2.1 Crystal structure and phase identification of $LnSr_{2.7}Ca_{0.3}Fe_3O_{10-\delta}$

XRD patterns of $LnSr_{2.7}Ca_{0.3}Fe_3O_{10-\delta}$ (Ln = La, Pr, and Sm) after fired at 900 °C, were illustrated in Figure 4-12. With Pr and Sm substitution, the diffraction peaks of both samples remained the tetragonal structure of RP n = 3 corresponded to $LaSr_3Fe_3O_{9.9}$ (JCPDS no. 81-1234) with the perovskite co-existed phase. However, other impurity phase, $(Sm,Sr)FeO_4$, was also found and refined based on the $LaSrFeO_4$ structure (JCPDS no. 71-1744), RP n= 1, due to the phase instability as the previous discussed (equation (4-1)).[84, 87, 88] No Pr- and Sm-oxide phase was observed in the spectrumindicating that Pr and Sm were incorporated in the $LnSr_{2.7}Ca_{0.3}Fe_3O_{10}$ structure. To identified the ratio of impurities in the structure, the ratio of perovskite impurity to the RP n = 3 structure was calculated from the peak area of 202 lattice plane of perovskite structure and the 217 lattice plane of RP n = 3 structure because the main peaks of both phases were overlapped. While the ratio of $(Sm,Sr)FeO_4$ impurity to the RP n = 3 phase was calculated from the peak area of the main diffraction peak of each phase (the 103 lattice plane of RP n = 1 phase and the 107 lattice plane of $LnSr_{2.7}Ca_{0.3}Fe_3O_{10-\delta}$). These ratios were as summarized in Table 4-6. The perovskite ratio was lower than 5% in $LnSr_{2.7}Ca_{0.3}Fe_3O_{10-\delta}$ (Ln = Pr, La)and increased almost 10 % by Sm substitution while the $(Sm,Sr)FeO_4$ impurity phase was ~6%, which indicated that the RP structure of Sm substituted sample was transformed. Since the amount of impurity phases (perovskite in $PrSr_{2.7}Ca_{0.3}Fe_3O_{10-\delta}$ and $(Sm,Sr)FeO_4$ in $SmSr_{2.7}Ca_{0.3}Fe_3O_{10-\delta}$) were quite low, the effect of these impurities was thus negligible. However, the effect of $(Sm,Sr)FeO_3$ would be further discussed.

Table 4- 6 Peak area and impurity to RP ratio in $LnSr_{2.7}Ca_{0.3}Fe_3O_{10-\delta}$ (Ln = La, Pr, and Sm)

Ln in $LnSr_{2.7}Ca_{0.3}Fe_3O_{10-\delta}$	Peak area				Perovskite to RP n = 3 ratio	RP n = 1 to RP n = 3 ratio
	2 0 2 of perovskite	2 1 7 of RP n = 3	1 0 3 of RP n = 1	1 0 7 of RP n = 3		
La	65	4496	-	17721	0.01	-
Pr	223	5428	-	19197	0.04	-
Sm	670	6176	718	12113	0.11	0.06

With Pr and Sm substitution (Figure 4-1(b-c)), the XRD patterns were shifted to the higher angle, which was easily seen in Figure 4-13 (inset), indicating the shrinkage and distortion of the unit cell. The lattice parameters, *a* and *c*, and the unit cell volumes of $LnSr_{2.7}Ca_{0.3}Fe_3O_{10-\delta}$, calculated from the main lattice plane of 107 using a Scherrer equation, were shown in Figure 4-14(a)-(c). By replacing La with Pr, the parameters (*a* and *c*) and unit cell volume decreased because the ionic radius of Pr^{3+} (1.32 Å) and Pr^{4+} (1.13 Å) were smaller than that of La^{3+} (1.36 Å), [122] resulting in the decreasing of bond length between (Ln, Sr, Ca)–O which leads to the unit cell distortion along *a*-and *c*-axes. Once Ln = Sm, the parameter *a* was increased, the parameter *c* was not significantly changed, resulting the increase in unit cell volume, which was because Sm ion had the mixed oxidation state of +2 and +3, providing a longer (Ln. Sr, Ca)-O bond and the expansion of unit cell volume from Pr to Sm.[123]

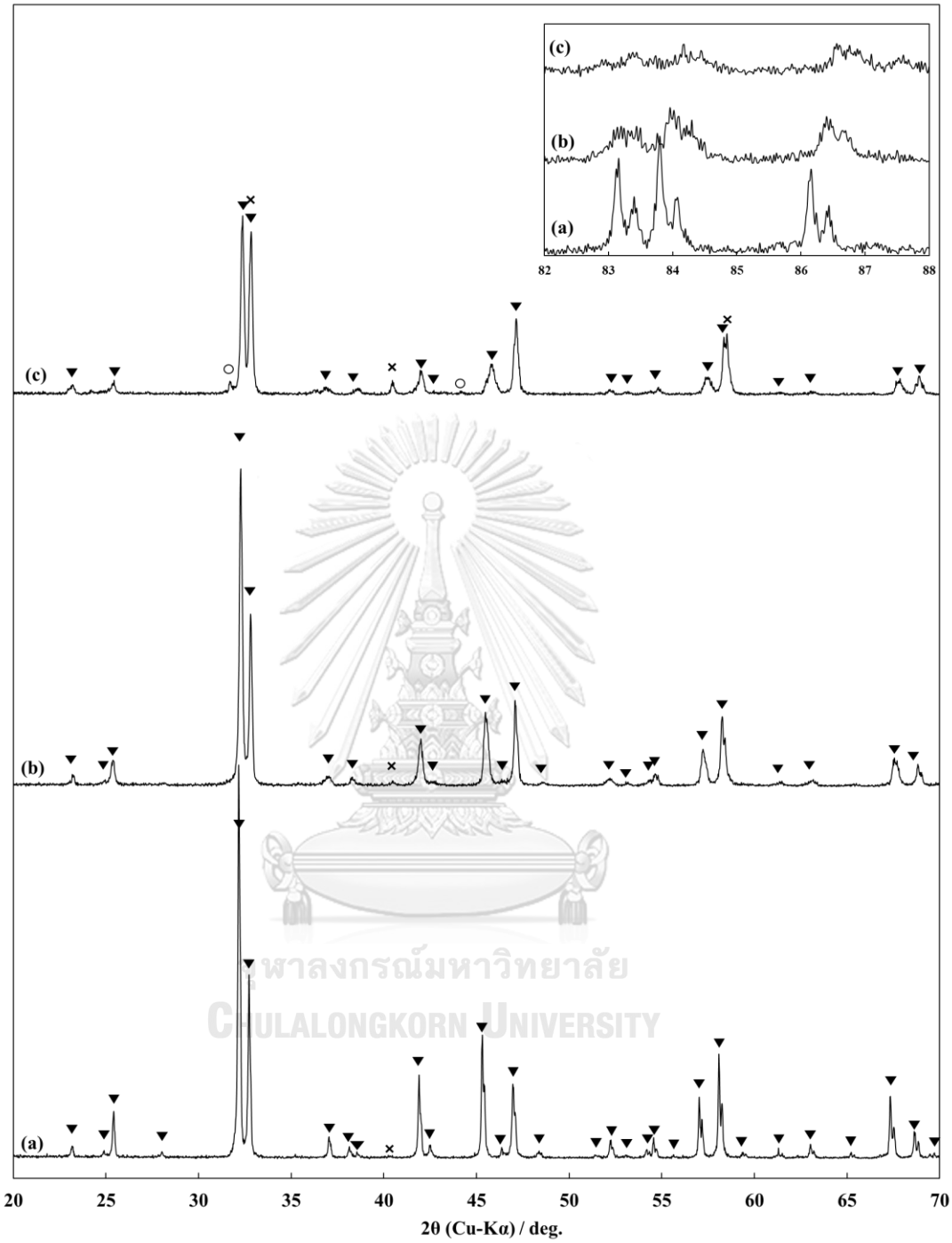

Figure 4-13 XRD pattern of the various $LnSr_{2.7}Ca_{0.3}Fe_3O_{10-\delta}$ after sintered at 1400°C for 12 h and annealed at 900°C for 30 min with *(*▼ = $LaSr_{3-x}Ca_xFe_3O_{9.9}$, **x** = $SrFeO_3$, and ○ = $(Ln,Sr)FeO_4$*)*; *(a)* Ln = La, *(b)* Ln = Pr and *(c)* Ln = Sm

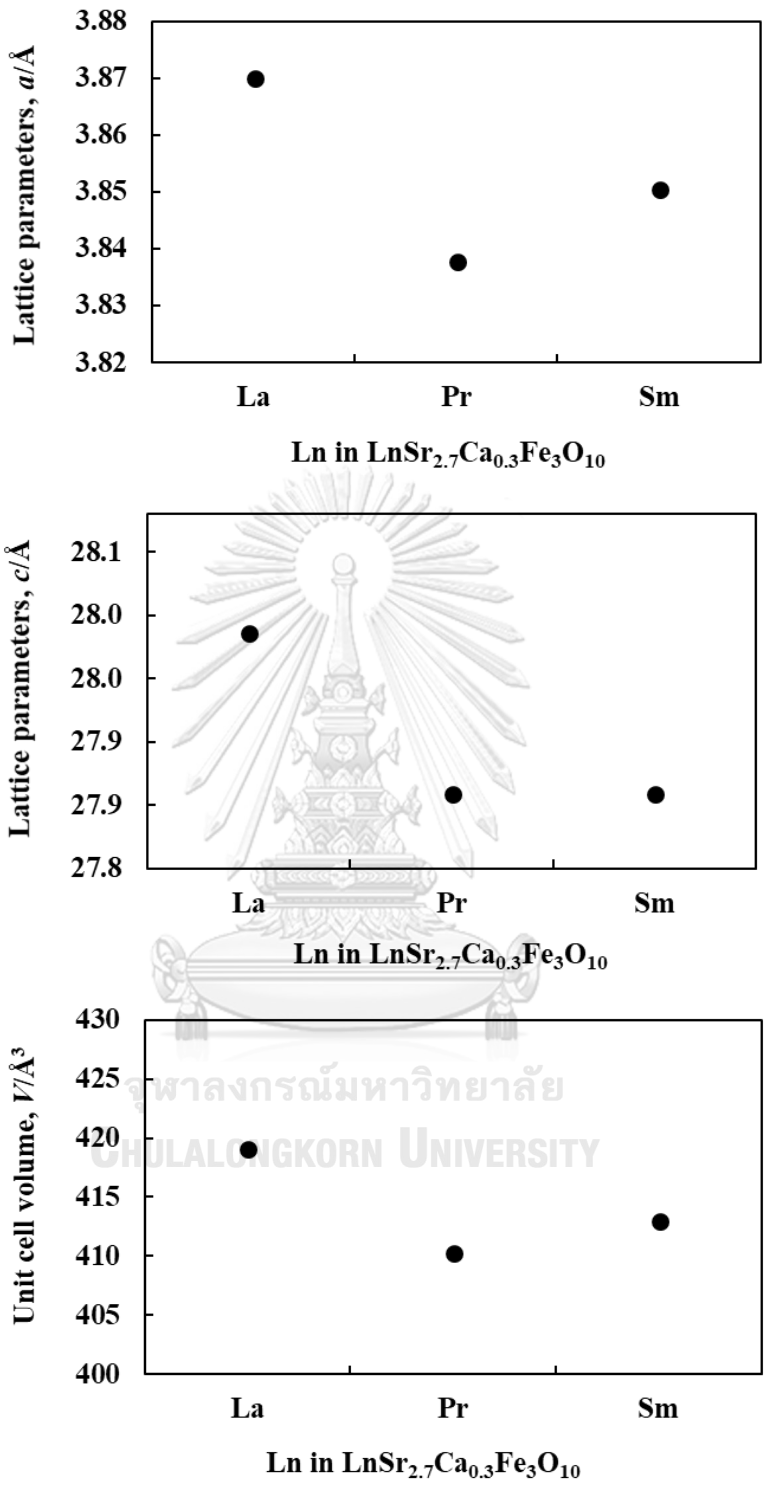

Figure 4-14 *(a)* Lattice parameter a, *(b)* and lattice parameters c, and *(c)* unit cell volume of the $LnSr_{2.7}Ca_{0.3}Fe_3O_{10-\delta}$ (Ln = La, Pr, and Sm*)*

4.2.2 TG analysis of $LnSr_{2.7}Ca_{0.3}Fe_3O_{10-\delta}$

The weight loss of $LnSr_{2.7}Ca_{0.3}Fe_3O_{10-\delta}$ (Ln = La, Pr, and Sm) samples were recorded in air in the temperatures between 25-800 °C as presented in Figure 4-15. The thermogram showed the weight loss increased from $LaSr_{2.7}Ca_{0.3}Fe_3O_{10-\delta}$ to $SmSr_{2.7}Ca_{0.3}Fe_3O_{10-\delta}$, implying that the substitution of smaller ionic radii increased the oxygen vacancy in the structure. With Pr substitution, the present of Pr^{4+} possibly caused the increasing of the bending of bond angle and distorted the structure, resulting in the loss of oxygen from the strucuture in order to maintain the RP structure. This phenomenon was also observed by Kim *et al.* who investigated the effect of *A*-site size through the comparison between $LaSr_3Fe_3O_{10-\delta}$ and $NdSr_3Fe_3O_{10-\delta}$ and found that the smaller *A*-site of $NdSr_3Fe_3O_{10-\delta}$ generated more oxygen loss, compared with $LaSr_3Fe_3O_{10-\delta}$ due to the decreasing of binding energy between Ln-O bond in the lattice with decreasing the ionic radii of Ln.[89] In case of Sm substitution, the existing of Sm^{2+} decreased the total positive charge in the structure and possibly caused the elimination of oxygen for the charge compensation. In addition, the high value of oxygen loss in Sm substituted sample might be relate with the loss of oxygen in the impurity phases such as perovskite, $(Sm,Sr)FeO_3$. Demont *et al.*investigated the oxygen loss in perovskites, $La_{0.6}Sr_{0.4}FeO_3$-δ and $La_{0.6}Sr_{0.4}CoO_3$-δ, and in the RP, $LaSrFeO_4$ and $LaSrCoO_4$, in Ar atmosphere and found that the perovskite structures provided higher oxygen loss than the RP structures because the oxidation state of metal at *B*-site in perovskite was greater than RP structure.[124]

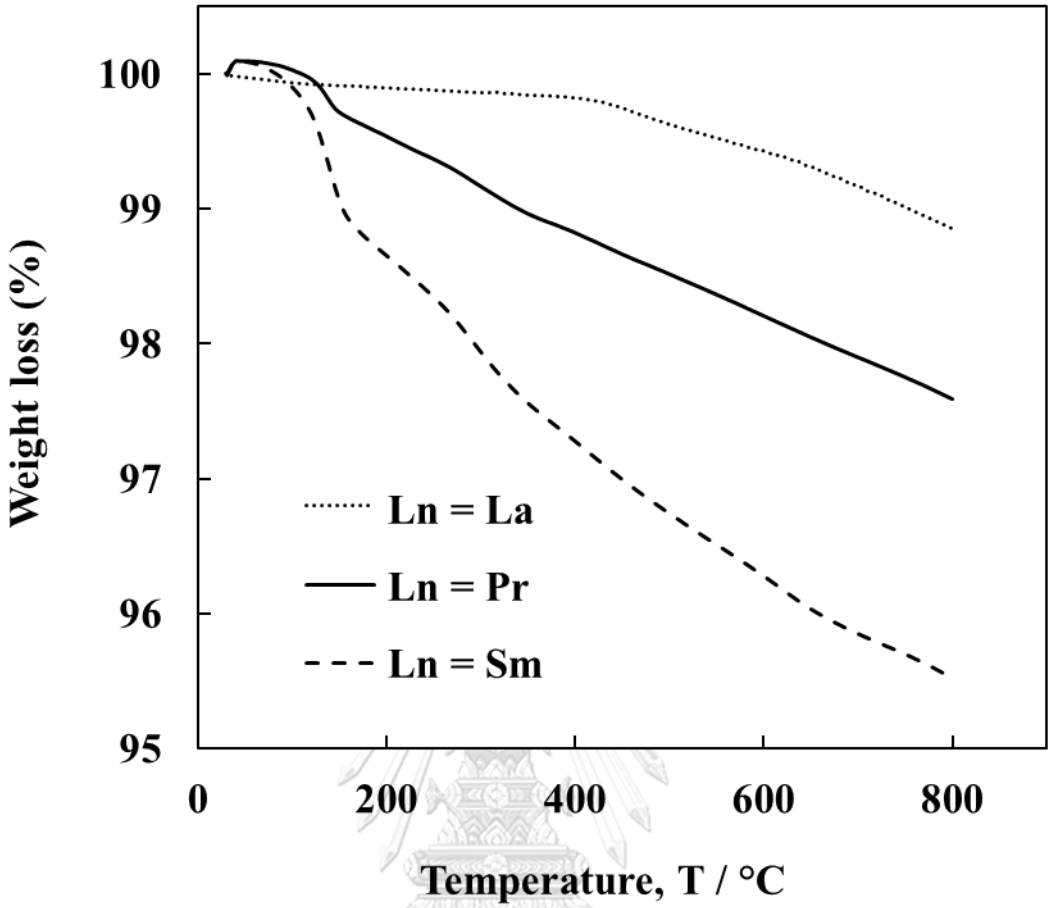

Figure 4-15 TGA plots of the $LnSr_{2.7}Ca_{0.3}Fe_3O_{10-\delta}$ (Ln = La, Pr, and Sm) measured in air at 25-800 °C.

4.2.3 Thermal expansion behavior of $LnSr_{2.7}Ca_{0.3}Fe_3O_{10-\delta}$

Figure 4-16 exhibited the thermal expansion behaviors of the $LnSr_{2.7}Ca_{0.3}Fe_3O_{10-\delta}$ (Ln = La, Pr, and Sm) specimens operated at 25-800 °C in air. $LaSr_{2.7}Ca_{0.3}Fe_3O_{10-\delta}$ and $PrSr_{2.7}Ca_{0.3}Fe_3O_{10-\delta}$ showed a linear degree of thermal expansion ($\Delta L/L_0$) at the temperature lower than 400 °C, while $SmSr_{2.7}Ca_{0.3}Fe_3O_{10-\delta}$ showed a linear thermal expansion until 300 °C. However, the slopes were non-linearly increased at higher temperature due to the loss of oxygen from the lattice. Table 4-7 showed the calculated average thermal expansion coefficient (TEC) values at two different temperature ranges of 25–400 °C and 400–800 °C. The average TEC value of the samples slightly decreased from substitution on La by Pr but increased by Sm substitution. The decrease in TEC by Pr substitution was possibly caused by the strong interaction of the shorten Pr-O and Fe-O bond length, and a smaller unit cell, which made the unit cell difficulty to expand.[112] However, the oxygen loss of Pr substituted sample also had an influence on reducing the total negative charge in the structure, causing the reduction of Fe, decreasing the electrostatic attraction of Fe-O bond, and resulting in the increased TEC .[98] In this case, the TEC value of Pr substituted sample was thus slightly decreased, indicating the interaction with shorten bond length was dominated the effect of oxygen loss. For Sm substitution, the increasing of TEC was caused by a large concentration of oxygen vacancies in $SmSr_{2.7}Ca_{0.3}Fe_3O_{10-\delta}$ structure. As a result, the TEC was significantly higher than that of LSGM (18.82 x $10^{-6}K^{-1}$ at 25-800 °C), thus the delamination of $SmSr_{2.7}Ca_{0.3}Fe_3O_{10-\delta}$ was concerned.

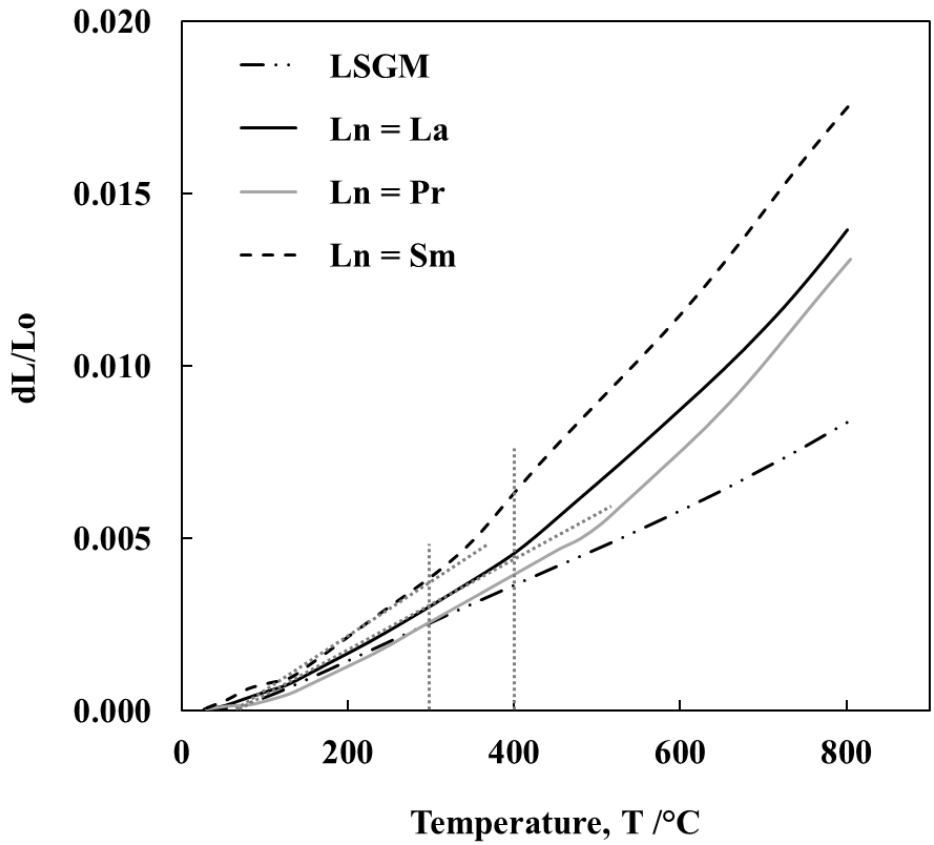

Figure 4-16 Thermal expansion ($\Delta L/L_o$) curves of $LnSr_{2.7}Ca_{0.3}Fe_3O_{10-\delta}$ (Ln = La, Pr, and Sm) in air in a temperature range of 25-800 °C compared to LSGM electrolyte

Table 4-7 TECs of $LnSr_{2.7}Ca_{0.3}Fe_3O_{10-\delta}$ (Ln = La, Pr, and Sm) samples

La in $LnSr_{2.7}Ca_{0.3}Fe_3O_{10-\delta}$	TEC ($10^{-6}K^{-1}$)	
	25-400 °C	400-800 °C
La	11.48	34.92
Pr	10.56	32.72
Sm	16.98	44.02

4.2.4 Total conductivity of $LnSr_{2.7}Ca_{0.3}Fe_3O_{10-\delta}$

The total conductivity of $LnSr_{2.7}Ca_{0.3}Fe_3O_{10-\delta}$ (Ln = La, Pr, and Sm) samples was investigated in air at 200-800 °C, as shown in Figure 4-17. With Pr and Sm substitution, the sample provided a similar behavior as $LaSr_{2.7}Ca_{0.3}Fe_3O_{10-\delta}$, which was a semiconducting behavior. The conductivity increased as increasing temperature and decreased after 400 °C due to the oxygen loss .[98, 106, 109] The total conductivity of $LnSr_{2.7}Ca_{0.3}Fe_3O_{10-\delta}$ decreased from La (~198 Scm^{-1} at 400 °C) to Pr (~150 Scm^{-1} at 400 °C) and Sm (83 Scm^{-1} at 500 °C), suggesting the electron mobility was decreased with decreasing size of Ln^{3+}. This result was well-related to the oxygen loss from TGA (Figure 4-15). The oxygen vacancy blocked the electron transformation between 2*p* orbital of oxygen and 3*d* orbital of Ln and Fe, consequently decreased the electron mobility of $PrSr_{2.7}Ca_{0.3}Fe_3O_{10-\delta}$ and $SmSr_{2.7}Ca_{0.3}Fe_3O_{10-\delta}$. In the case of Pr substitution, even the mixed oxidation state of $Pr^{3+/4+}$ could generate the electron-hole and promote the electron migration, the effect of oxygen vacancy, which prohibit the electron transformation, was dominant the effect of oxidation state.

For Sm substitution, the decrease in conductivity might be caused by the impurity phases, such as perovskite. The $Pr_{0.8}Sr_{0.2}FeO_3$ had the conductivity around 78 Scm^{-1} at 800 °C [125] and the conductivity of $Ln_{0.5}Sr_{0.5}FeO_{3-\delta}$ was decreased in the sequence La > Pr > Nd > Sm. The mismatch in size of *A*-site cation distorted the structurelowered the overlapping between oxygen and Fe, and perturbed the electron transportation.[95] Thus, in this study, it was concluded that $(Sm,Sr)FeO_3$ might provide a low conductivity which influenced the conductivity of $SmSr_{2.7}Ca_{0.3}Fe_3O_{10-\delta}$.

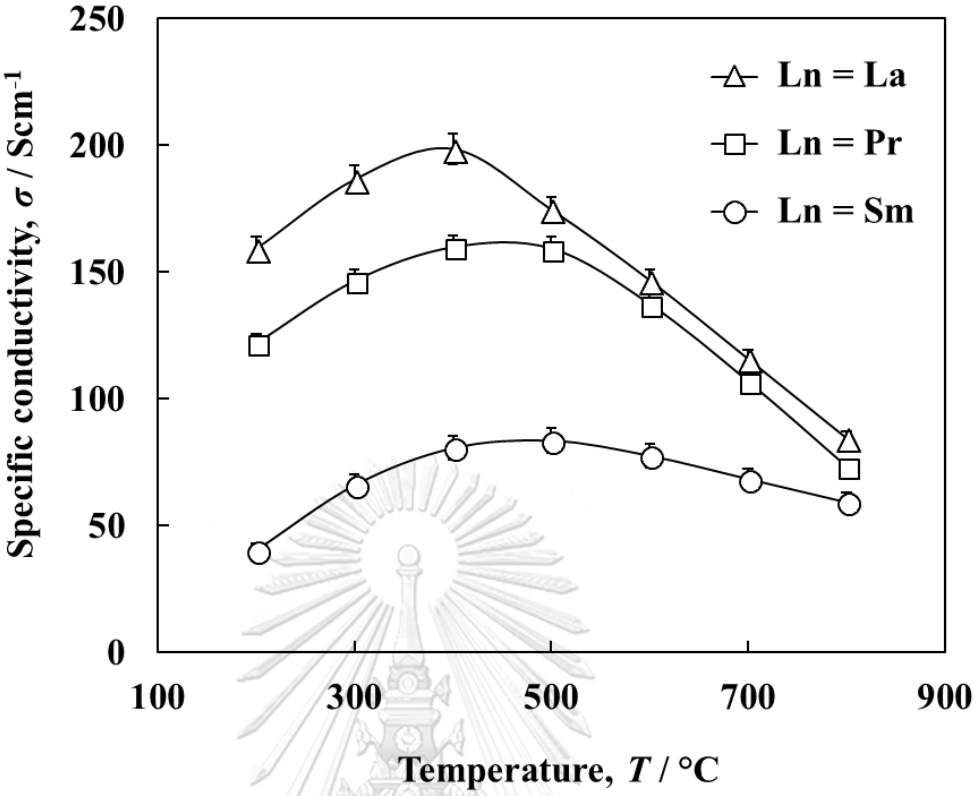

Figure 4-17 The total conductivity of $LnSr_{2.7}Ca_{0.3}Fe_3O_{10-\delta}$ (Ln = La, Pr, and Sm) at 200-800 °C in air

4.2.5 Microstructure of $LnSr_{3-x}Ca_xFe_3O_{10-\delta}$

Figure 4-18 presented the cross-section SEM images of $LnSr_{3-x}Ca_xFe_3O_{10-\delta}$ (Ln = La, Pr, and Sm) cathodes after fired on the LSGM electrolyte at 1000 °C in air. The porous top area was $LnSr_{3-x}Ca_xFe_3O_{10-\delta}$ cathodes. No significantly difference in microstructure and particle size between the samples The samples were homogeneous and the average particle size was approximately 5-7 μm. Thus, the electrochemical performance was possibly not affected by the microstructure.

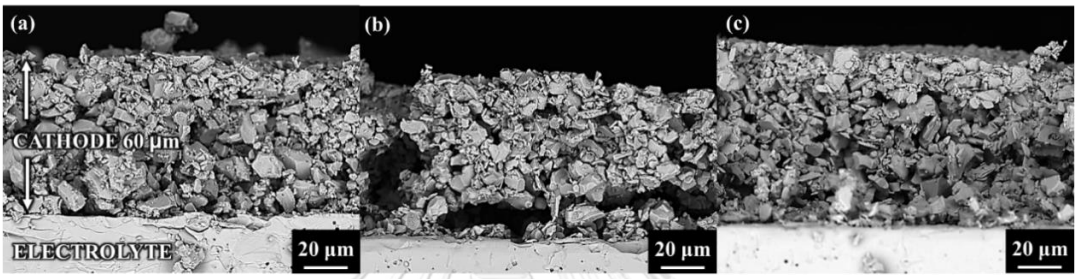

Figure 4-18 SEM images of crossed section of the $LnSr_{2.7}Ca_{0.3}Fe_3O_{10-\delta}$ samples*: (a)* Ln = La, *(b)* Ln = Pr, and *(c)* Ln = Sm

4.2.6 X-ray Photoelectron Spectroscopy (XPS)

4.2.6.1 Lanthanum spectra for $LaSr_{2.7}Ca_{0.3}Fe_3O_{10-\delta}$

Figure 4-19 exhibited the XPS spectra of La 3*d* core level for $LaSr_{2.7}Ca_{0.3}Fe_3O_{10-\delta}$. The band spectra of 3*d* core level showed the splitting of La 3*d* 5/2 and La 3*d* 3/2 caused by the effect of spin-orbit coupling with the separated energy of ~17 eV. Each splitting peak was deconvoluted to four peaks, which were $4f^0$ (the main core level without electrons in the 4*f* orbital and no charge transfer from ligand), $4f^1$L-bonding, $4f^1$L-antibonding (the satellites with charge transfer from ligand, L, for bonding and antibonding with the final state to 4*f* orbitals) and the plasmon peak.[126, 127] However, all peaks were corresponded to La^{3+}, suggesting the oxidation state of La in $LaSr_{2.7}Ca_{0.3}Fe_3O_{10-\delta}$ was 3+.

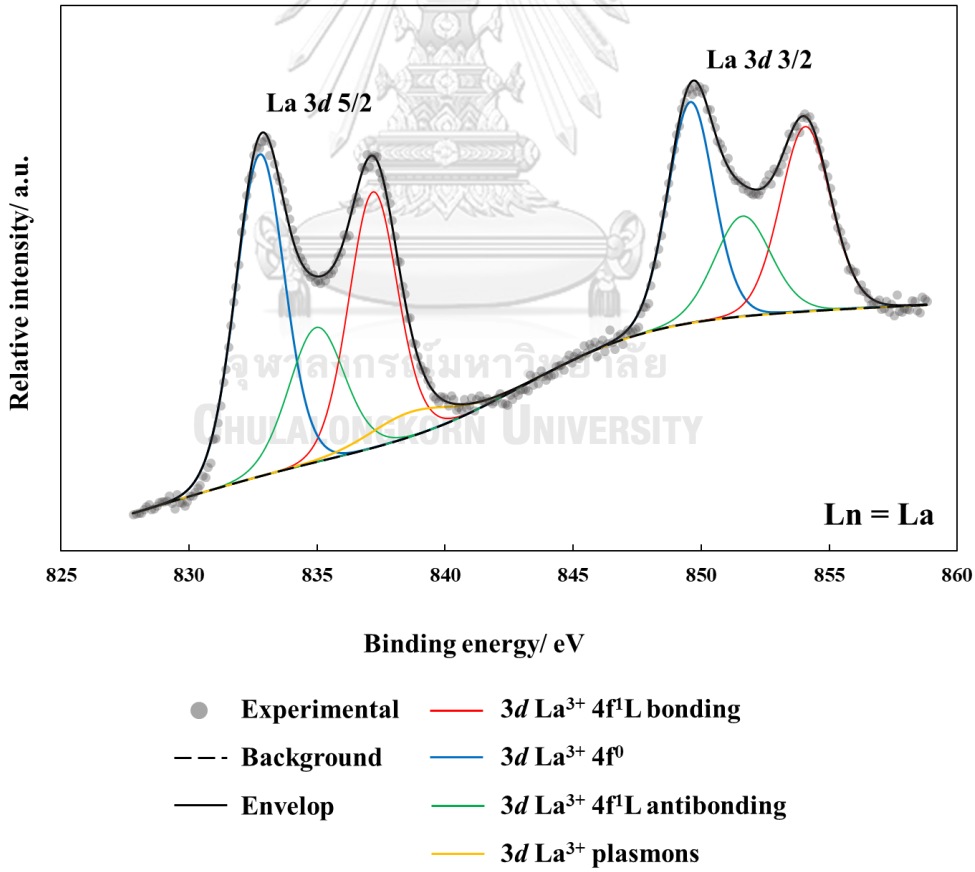

Figure 4-19 XPS spectra of La 3*d* core–level of $LaSr_{2.7}Ca_{0.3}Fe_3O_{10-\delta}$

4.2.6.2 Praseodymium spectra for $PrSr_{2.7}Ca_{0.3}Fe_3O_{10-\delta}$

The XPS spectra of Pr 3*d* core – level spectra for $PrSr_{2.7}Ca_{0.3}Fe_3O_{10-\delta}$ was illustrated in Figure 4-20. The deconvolution exhibited the characteristics of Pr 3*d* 5/2 and Pr 3*d* 3/2 with the separated energy approximately ~20 eV. Each splitting peak was deconvoluted to the main core peak without charge transfer of 3*d* 5/2 and 3*d* 3/2, the spin-split doublets of 3*d* 5/2 and 3*d* 3/2 and the satellite peak of 3*d* 3/2. The peak of Pr^{4+} was found, which belonged to the electronic configuration state of $3d^9 4f^1$. Thus, Pr for $PrSr_{2.7}Ca_{0.3}Fe_3O_{10-\delta}$ provided the mixed oxidation states of 3+ and 4+ [123] The peak position of Pr 3*d* for $PrSr_{2.7}Ca_{0.3}Fe_3O_{10-\delta}$ was summarized in Table 4-8.

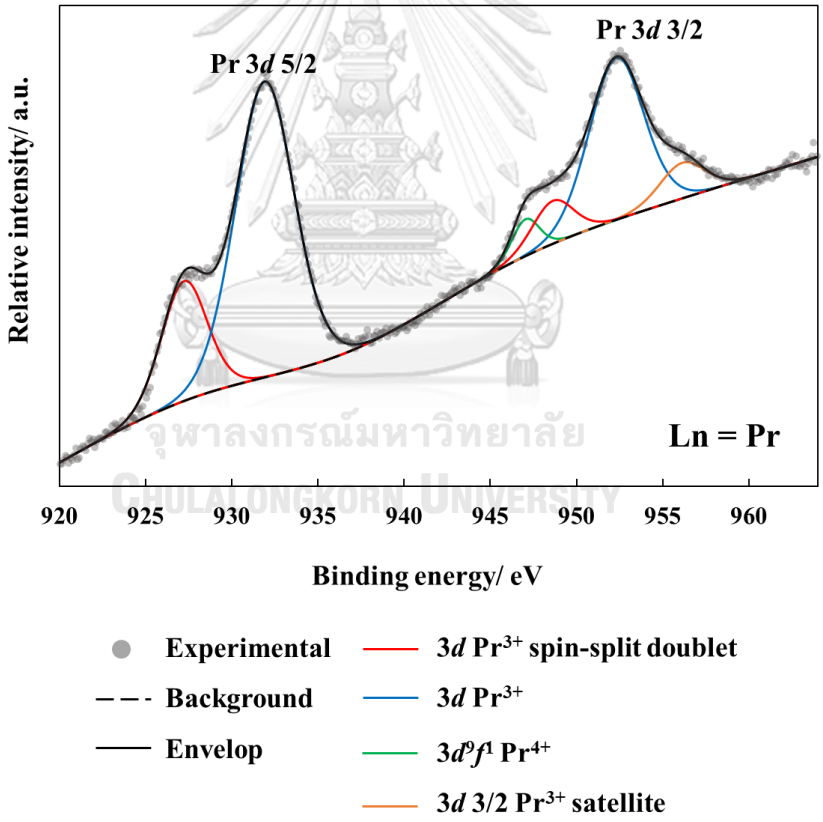

Figure 4-20 XPS spectra of Pr 3*d* core – level of $PrSr_{2.7}Ca_{0.3}Fe_3O_{10-\delta}$

Table 4-8 Chemical states of Pr 3*d* for $PrSr_{2.7}Ca_{0.3}Fe_3O_{10-\delta}$.

Peak Designation	Peak position (eV)
3*d* 5/2 Pr^{3+}	932
3*d* 5/2 Pr^{3+} spin-split doublet	927
$3d^9f^1$ for Pr^{4+}	947
3*d* 3/2 Pr^{3+}	952
3*d* 3/2 Pr^{3+} spin-split doublet	948
3*d* 3/2 Pr^{3+} satellites	956

4.2.6.3 Samarium spectra for $SmSr_{2.7}Ca_{0.3}Fe_3O_{10-\delta}$

The XPS spectra of Sm 3*d* core – level for $SmSr_{2.7}Ca_{0.3}Fe_3O_{10-\delta}$ was exhibited in Figure 4-21. The influence of spin-orbit caused the splitting of Sm 3*d* core – level to Sm^{3+} 3*d* 5/2 and 3*d* 3/2 at the binding energy of 1083 eV and 1108 eV, respectively, while the Sm^{2+} 3*d* 5/2 and 3*d* 3/2 at the binding energy of 1081 eV and 1105 eV, respectively, thus Sm was mixed oxidation state of 2+ and 3+. In addition, the additional peak at 1076 eV for Sm^{2+} and the broad peak of Sm Auger at 1110.5 eV were found, which generally appeared in the metal oxide. *[128, 129]*

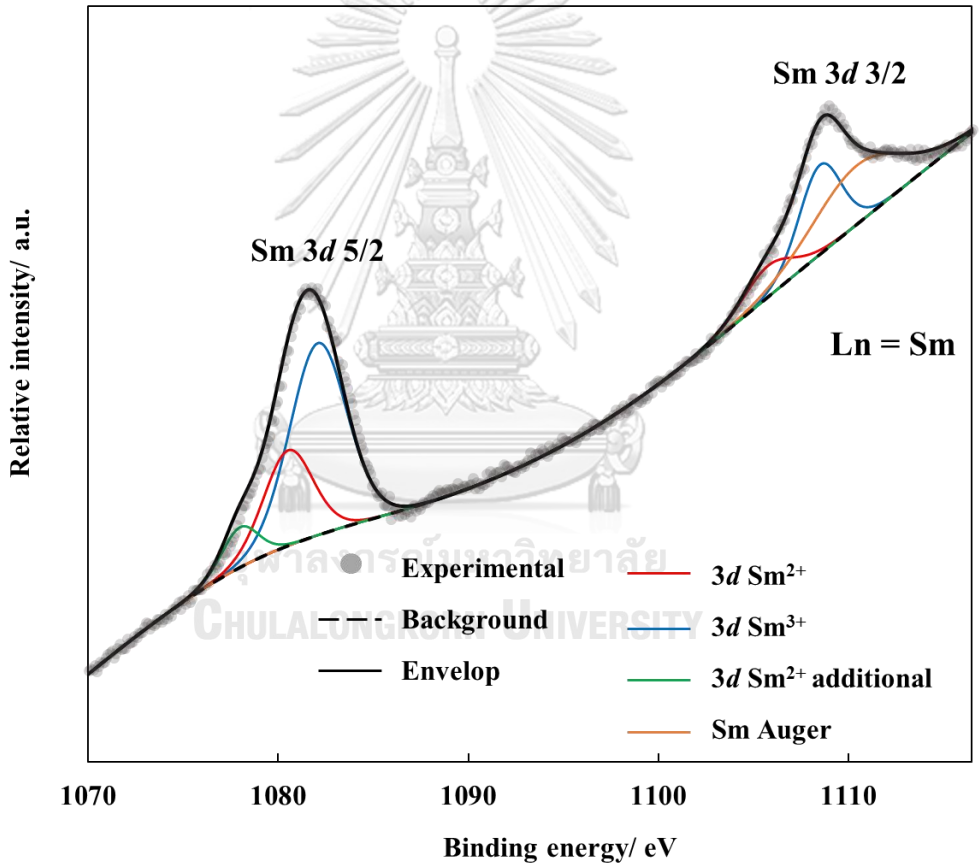

Figure 4-21 XPS spectra of Sm 3*d* core – level of $SmSr_{2.7}Ca_{0.3}Fe_3O_{10-\delta}$

4.2.6.4 Iron spectra of $LnSr_{2.7}Ca_{0.3}Fe_3O_{10-\delta}$

The XPS spectra of Fe 2*p* core level for $LnSr_{2.7}Ca_{0.3}Fe_3O_{10-\delta}$ (Ln = La, Pr, and Sm) samples showed the splitting of 2*p* 3/2 and 2p ½ peaks, which was influenced by the spin-orbit coupling in Figure 4-22. The deconvolution of each 2*p* core – level showed the three main signals of Fe^{2+}, Fe^{3+}, and Fe^{4+}. The peaks with the binding energy of ~708, ~709.2 and ~711.5 eV were associated with Fe^{2+} 2*p* 3/2, Fe^{3+} 2*p* 3/2 and Fe^{4+} 2*p* 3/2, respectively. The peaks at binding energy about ~721.5, ~722.6 and 723.9 eV were also associated with Fe^{2+} 2*p* 1/2, Fe^{3+} 2*p* 1/2 and Fe^{4+} 2*p* 1/2, respectively.[116, 117, 130] Even the spectra of Fe 2*p* core level was not significantly shifted by the reducing size of La to Sm, the amount of each iron species was different.

The percentage for each chemical state of Fe 2*p* in $LnSr_{2.7}Ca_{0.3}Fe_3O_{10-\delta}$ were summarized in Table 4-9. Upon the substitution of Pr, the peak areas and percentages of Fe^{4+} was decreased while that of Fe^{2+} and Fe^{3+} was increased, compared to those of $LaSr_{2.7}Ca_{0.3}Fe_3O_{10-\delta}$, indicating the reduction of Fe occurred. The occur ofPr^{4+} in the structure promoted the reduction of Fe in order to compensate the charge in the structure.

With the substitution of Sm, the peak area and percentage of Fe^{2+} was not significantly changed while Fe^{3+} were decreased and Fe^{4+} was increased, compared to those of $LaSr_{2.7}Ca_{0.3}Fe_3O_{10-\delta}$, indicating the oxidation of Fe^{3+} to Fe^{4+} occurred. The oxidation of Fe in Sm substituted material was explained by the mixed oxidation stated of Sm^{2+} and Sm^{3+} in $SmSr_{2.7}Ca_{0.3}Fe_3O_{10-\delta}$ structure in order to compensate the charge in the structure.

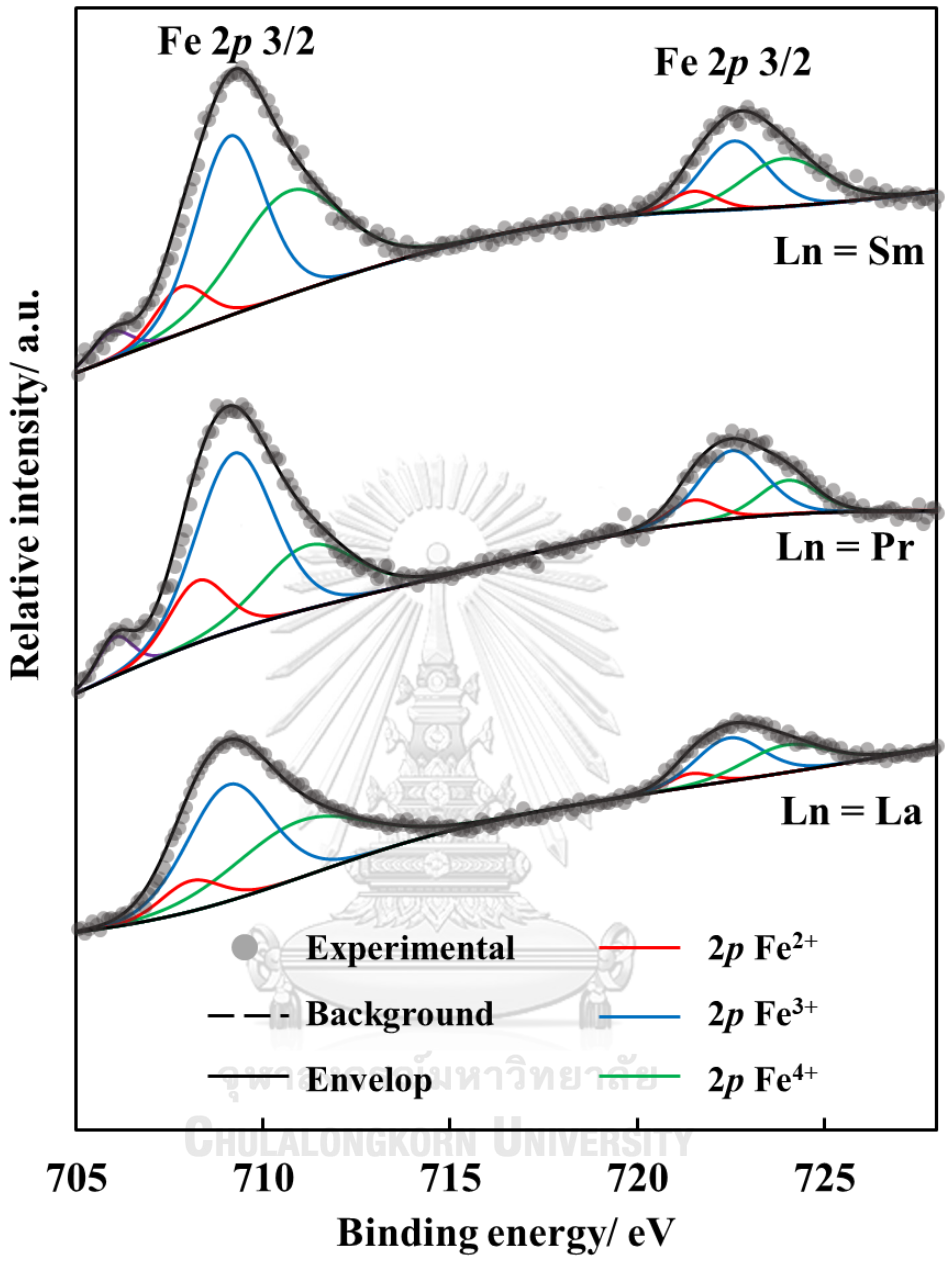

Figure 4-22 XPS spectra of Fe 2p core – level spectra in $LnSr_{2.7}Ca_{0.3}Fe_3O_{10-\delta}$ (Ln = La, Pr, and Sm)

Table 4-9 Percentage for each chemical state of Fe 2*p* in $LnSr_{2.7}Ca_{0.3}Fe_3O_{10-\delta}$ δ (Ln = La, Pr, and Sm)

Oxidation State	Ln in $LnSr_{2.7}Ca_{0.3}Fe_3O_{10-\delta}$		
	La	Pr	Sm
Fe^{2+}	9.63	14.93	9.56
Fe^{3+}	50.82	59.16	50.41
Fe^{4+}	39.55	25.91	40.03

4.2.7 Electrochemical performance of $LnSr_{2.7}Ca_{0.3}Fe_3O_{10-\delta}$

4.2.7.1 Single cell performance for $LnSr_{2.7}Ca_{0.3}Fe_3O_{10-\delta}$ cathodes

The electrochemical performance of the cells for $LnSr_{2.7}Ca_{0.3}Fe_3O_{10-\delta}$ (Ln = La, Pr, and Sm) cathodes was performed under 3% humidified H_2 fuel. The terminal voltage and power density as a function of current density were collected using potentiostatic measurement in the temperature range of 600-800 °C. The slopes of activation polarization (Figure 4-23(a) (inset)) and ohmic polarization of $LaSr_{3-x}Ca_xFe_3O_{10-\delta}$ (Figure 4-23(a)) were in the order from high to low values as follows, $SmSr_{2.7}Ca_{0.3}Fe_3O_{10-\delta}$ > $LaSr_{2.7}Ca_{0.3}Fe_3O_{10-\delta}$ > $PrSr_{2.7}Ca_{0.3}Fe_3O_{10-\delta}$, indicating the kinetics of the electrochemical reaction and the electrical and ionic transportation of the cells increased by the Pr substitution but decreased by the Sm substitution, compared to La substitution.

The power density of the cells at 800 °C for $LnSr_{2.7}Ca_{0.3}Fe_3O_{10-\delta}$ (Ln = La, Pr, and Sm) cathodes were illustrated in Figure 4-23(b). $PrSr_{2.7}Ca_{0.3}Fe_3O_{10-\delta}$ gave the maximum power density of 356 $mWcm^{-2}$, which was higher than that of $LaSr_{2.7}Ca_{0.3}Fe_3O_{10-\delta}$ (301 $mWcm^{-2}$), while $SmSr_{2.7}Ca_{0.3}Fe_3O_{10-\delta}$ gave a lower maximum power density at 242 $mWcm^{-2}$. The maximum power densities of the single cells for

$LnSr_{2.7}Ca_{0.3}Fe_3O_{10-\delta}$ cathodes at different operating temperature were summarized in Table 4-10 and showed that the electrochemical performance was also promoted at high temperature.

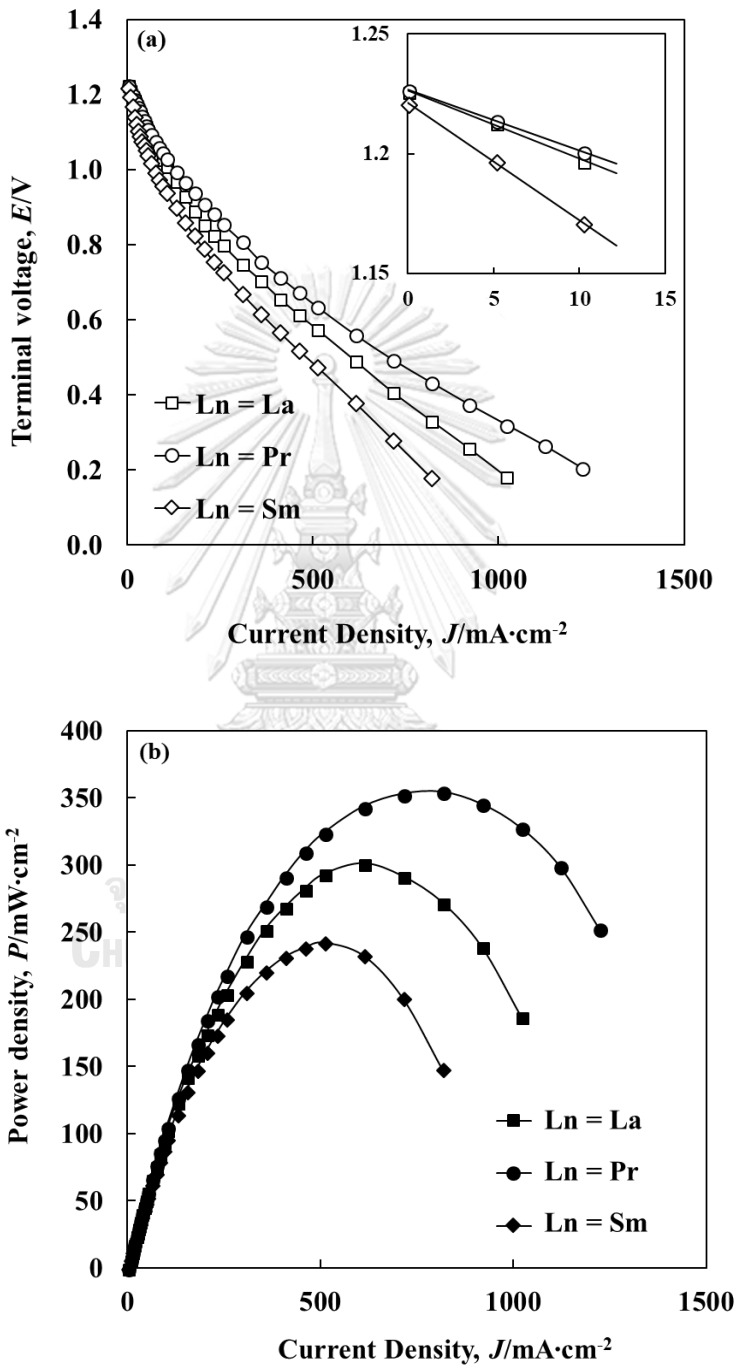

Figure 4-23. *(a)* Terminal voltage and *(b)* power densities as a function of current density of the $LnSr_{2.7}Ca_{0.3}Fe_3O_{10-\delta}$ *(*Ln = La, Pr, and Sm*)* cathodes at 800 °C.

Table 4- 10 The maximum power density of the single cells for the $LnSr_{2.7}Ca_{0.3}Fe_3O_{10-\delta}$ *(*Ln = La, Pr, and Sm*)* cathodes at the temperature range of 600-800 °C in H_2 fuel.

Ln in $LaSr_{3-x}Ca_xFe_3O_{10-\delta}$	Maximum Powder density ($mW \cdot cm^{-2}$)		
	800 °C	750 °C	700 °C
La	301	186	61
Pr	354	233	88
Sm	242	138	80

4.2.7.2 Resistance of the single cells for $LnSr_{2.7}Ca_{0.3}Fe_3O_{10-\delta}$ cathodes

The impedance spectra of single cells for $LnSr_{2.7}Ca_{0.3}Fe_3O_{10-\delta}$ (Ln = La, Pr, and Sm) cathodes were analyzed in the temperature range of 600-800 °C. Since the impedance curve corresponded to the reactions that taking place on the surface, in this case, the particle sizes of $LnSr_{2.7}Ca_{0.3}Fe_3O_{10-\delta}$ were not significantly different, , therefore the gas diffusion rate from cathode to electrolyte should not significantly different. As a result, the different in ASR depended on the oxidation-reduction reaction (ORR) of cathode, which could be depended on the size of Ln substituted in $LnSr_{2.7}Ca_{0.3}Fe_3O_{10-\delta}$ cathodes.

The impedance spectra of Pr substitution sample, $PrSr_{2.7}Ca_{0.3}Fe_3O_{10-\delta}$ at 800 °C, Figure 4-24, showed the lowest ASR which was in agreement with the highest cell performance. Even the conductivity of $PrSr_{2.7}Ca_{0.3}Fe_3O_{10-\delta}$ was lower than that of $LaSr_{2.7}Ca_{0.3}Fe_3O_{10-\delta}$, the ASR of Pr was lower and the cell performance was better that could be related to the oxygen vacancy in the material structure. As previously discussed, the ASR could relate to both electronic and ionic transportation in the cathode structure. In $PrSr_{2.7}Ca_{0.3}Fe_3O_{10-\delta}$, the cathode had higher oxygen vacancy than $LaSr_{2.7}Ca_{0.3}Fe_3O_{10-\delta}$ cathode, therefore it would

enhance the migration of oxide ions through the oxygen vacancies in the structure easier and consequently promoted the ORR rate, and reduced ASR. Moreover, the previous research found that the Pr substitution for Sr showed a higher catalytic activity for oxygen dissociation on the surface than $LaSr_3Fe_3O_{10-\delta}$ cathode due to the mixed valence state of Pr^{+3} and Pr^{+4}.

However, $SmSr_{2.7}Ca_{0.3}Fe_3O_{10-\delta}$ showed the higher ASR than $LaSr_{2.7}Ca_{0.3}Fe_3O_{10-\delta}$, which was corresponded to the cell performance, impling that the resistance of the cell was increased. This could be related to the high concentration of oxygen vacancies of $SmSr_{2.7}Ca_{0.3}Fe_3O_{10-\delta}$ which could block the electron transportation between the metal-O bonds and significantly reduced the conductivity of the sample and delayed the rate of ORR. Even the oxygen vacancy was important for the oxide ion transportation of SOFC cathode, too high concentration of oxygen vacancies was not able to compensate the poor conductivity and thus decreased the ORR of $SmSr_{2.7}Ca_{0.3}Fe_3O_{10-\delta}$. Therefore, the proper concentration of oxygen vacancies in $LnSr_{2.7}Ca_{0.3}Fe_3O_{10-\delta}$ could be controlled by the substitution of suitable ionic radii to facilitate both oxide and electron transportation, maximize the ORR and enhance cell performance. The ASR value of the cell for $LnSr_{2.7}Ca_{0.3}Fe_3O_{10-\delta}$ (Ln = La, Pr, and Sm) cathodes at different operating temperatures were summarized in Table 4-11.

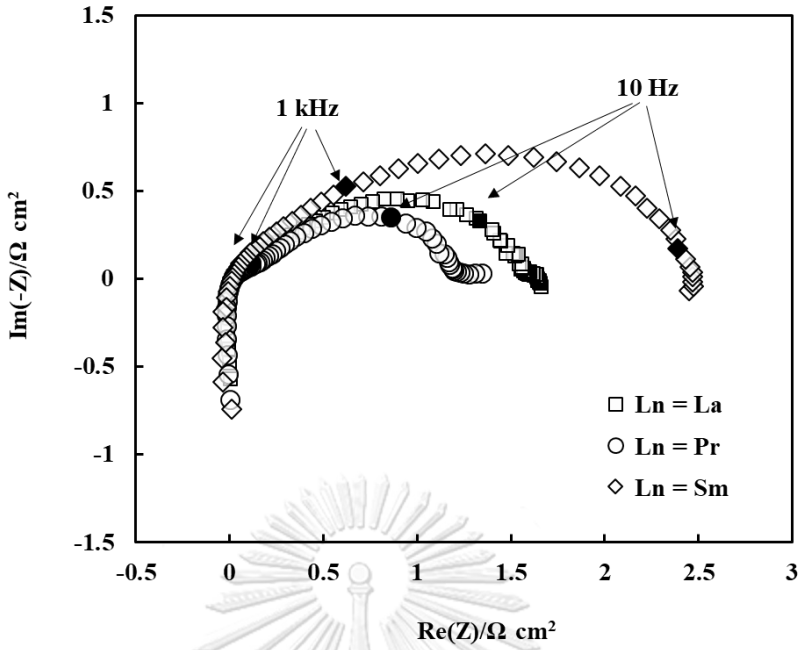

Figure 4-24 ASR of the $LnSr_{2.7}Ca_{0.3}Fe_3O_{10-\delta}$ (Ln = La, Pr, and Sm) cathodes at 800 °C.

Table 4-11 ASR of the single cells for the $LnSr_{2.7}Ca_{0.3}Fe_3O_{10-\delta}$ (Ln = La, Pr, and Sm) cathodes at 600-800 °C in H_2 fuel.

Ln in	Area specific resistance, ASR (Ω cm^2)		
$LnSr_{2.7}Ca_{0.3}Fe_3O_{10-\delta}$	800 °C	700 °C	600 °C
La	1.64	2.54	4.05
Pr	1.34	1.98	3.23
Sm	2.46	5.33	7.24

4.3 Effect of transition metal in $PrSr_{2.7}Ca_{0.3}Fe_{2.5}B_{0.5}O_{10-\delta}$ (B = Fe, Ni, Co, and Cu) Ruddlesden-Popper phases as Cathodes for Intermediate Temperature Solid Oxide Fuel Cells

4.3.1 Crystal structure and phase identification of $PrSr_{2.7}Ca_{0.3}Fe_{2.5}B_{0.5}O_{10-\delta}$

XRD patterns of $PrSr_{2.7}Ca_{0.3}Fe_{2.5}B_{0.5}O_{10-\delta}$ (B = Fe, Ni, Co, and Cu) after fired at 900 °C, were illustrated in Figure 4-25. With Ni, Co, and Cu substitution for Fe in $PrSr_{2.7}Ca_{0.3}Fe_{2.5}B_{0.5}O_{10-\delta}$, the tetragonal structure corresponding to $LaSr_3Fe_3O_{9.9}$ (JCPDS no. 81-1234) was remained with the perovskite coexisting phase. Besides that, the RP with n = 1 of $(Pr,Sr,Ca)(Fe,M)O_{4-\delta}$, corresponded to $LaSrFeO_4$ (JCPDS no. 71-1744), was also detectedbecause of phase instability as previously mentioned.[84, 87, 88] No Ni-, Co-, and Cu-oxide phases were found indicating Ni, Co, and Cu were incorporated in the $PrSr_{2.7}Ca_{0.3}Fe_{2.5}B_{0.5}O_{10-\delta}$ structure. The calculated ratio of impurities to the PR n = 3, was shown in Table 4-12 and the perovskite impurity in all sample was lower than 6% while the RP n = 1 impurity phase was ~12-14 % in the Ni and Cu substituted sample. Since the amount of impurity was quite low, it had not affectes physical and electrochemical performance of these samples. However, the unknown impurity phase was also detected in the Ni substitution sample, thus $PrSr_{2.7}Ca_{0.3}Fe_{2.5}Ni_{0.5}O_{10-\delta}$ was not thus further investigated.

Table 4-12 Peak area and impurity to RP ratio in $PrSr_{2.7}Ca_{0.3}Fe_{2.5}B_{0.5}O_{10-\delta}$ (B = Fe, Ni, Co, and Cu)

B in $PrSr_{2.7}Ca_{0.3}Fe_{2.5}B_{0.5}O_{10-\delta}$	Peak area				Perovskite to RP n = 3 ratio	RP n = 1 to RP n = 3 ratio
	2 0 2 of perovskite	2 1 7 of RP n = 3	1 0 3 of RP n = 1	1 0 7 of RP n = 3		
Fe	223	5428	-	-	0.04	-
Co	233	3996	224	14517	0.06	0.02
Cu	1113	7680	941	16369	0.14	0.06
Ni	747	6383	732	11564	0.12	0.06

With Co substitution, $PrSr_{2.7}Ca_{0.3}Fe_{2.5}Co_{0.5}O_{10-\delta}$, the XRD pattern was shifted to the higher angle, indicating the contraction of the unit cell. It was because the ionic radius of Co^{3+} (0.545 Å) is smaller than that of Fe^{3+} (0.55 Å) [83]

Upon Cu substitution, the XRD pattern of Cu content sample was slightly shifted to the higher angle indicating the shrinkage of the unit cell because the ionic radii of Cu^{3+} (0.54 Å) was smaller than the Fe^{3+}. However, when compared to the Co content sample, the XRD pattern of Cu contained sample was shifted to the lower angle, indicating the unit cell of $PrSr_{2.7}Ca_{0.3}Fe_{2.5}Cu_{0.5}O_{10-\delta}$ was larger than that of $PrSr_{2.7}Ca_{0.3}Fe_{2.5}Co_{0.5}O_{10-\delta}$. Since the ionic size of Cu^{3+} was smaller than the Co^{3+}, it could provide a smaller unit cell and the XRD pattern should shift to the higher angle. [104] However, this phenomenon was not observed in this work which could be due to the mixed oxidation state of $Cu^{2+/3+}$ in $PrSr_{2.7}Ca_{0.3}Fe_{2.5}Cu_{0.5}O_{10-\delta}$ structure. The mixed oxidation state of Cu was commonlyfound in perovskite and double perovskite structure, such as $Pr_{0.7}Sr_{0.3}Co_{1-y}Cu_yO_{3+\delta}$, $LnBaCo_{2-x}Cu_xO_{5+\delta}$, and

$SmBa_{0.5}Sr_{0.5}Co_{1.5}Cu_{0.5}O_{5+\delta}$.[118, 131, 132] The ionic radii of Cu^{2+} (0.73 Å) was larger than the Co^{3+} and Fe $^{3+}$, resulting in the larger unit cell than Co contained sample and slightly smaller unit cell than the Cu-free sample. The intensity of perovskite impurity phase (2θ of 40.3 degree) was increased and the ratio of characteristic peaks of RP n = 3 at 2θ of 32.4 and 32.9 degree was significantly changed. In addition, the diffraction peak of RP structure at 2θ of 32.8 degree was also overlapped with the characteristic peak of perovskite phase.. Thus, it was suggested that the phase of RP n = 3 of $PrSr_{2.7}Ca_{0.3}Fe_{2.5}Cu_{0.5}O_{10-\delta}$ was transformed to the perovskite phase

For Ni substitution, $PrSr_{2.7}Ca_{0.3}Fe_{2.5}Ni_{0.5}O_{10-\delta}$, the XRD pattern was shifted to the higher angle and no NiO phase was observed, indicating the unit cell was expanded and Ni was partially substituted in the structure. Since the ionic radii of Ni^{3+} (5.6 Å) was not different from that of Fe^{3+}, the expansion of the unit cell which could be a result of the mixed oxidation state of Ni^{2+} and Ni^{3+} in the structure.[104, 133] The ionic size of Ni^{2+} (0.69 Å) which was larger than that of Fe^{3+}, would affect the expansion of unit cell. [104] The intensity of the perovskite peak at 2θ of 40.4 degree was increased and the drastically change in the ratio of the RP structure at 2θ of ~32.2 and ~32.8 degree was clearly observed, indicating the $PrSr_{2.7}Ca_{0.3}Fe_{2.5}Ni_{0.5}O_{10-\delta}$ phase transformation occurred, as previous described in the Cu substitution sample.

The impurity ratios of perovskite and $(Pr,Sr,Ca)_2(Fe,B)O_4$ to $PrSr_{2.7}Ca_{0.3}Fe_{2.5}B_{0.5}O_{10-\delta}$ were calculated and found that the ratios of perovskite in all samples were lower than 6% while the RP n = 1 phase was ~12-14 % in the Ni and Cu substituted samples (Appendix A-6). Moreover, the unknown phase was also detected. Thus, $PrSr_{2.7}Ca_{0.3}Fe_{2.5}Ni_{0.5}O_{10-\delta}$ was not further investigated.

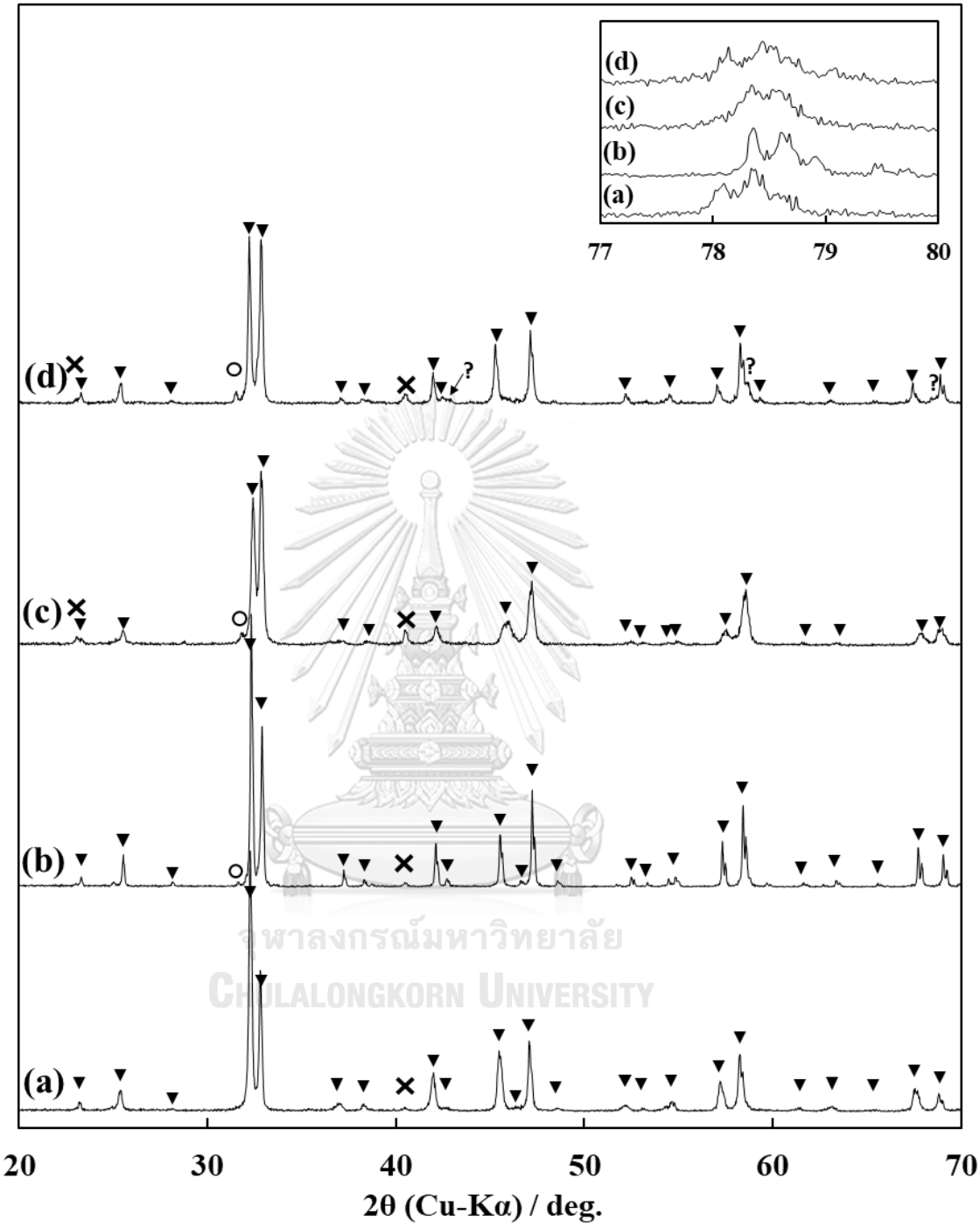

Figure 4-25 XRD pattern of the various $PrSr_{2.7}Ca_{0.3}Fe_{2.5}B_{0.5}O_{10-\delta}$ (B = Fe, Ni, Co, and Cu) after annealed at 900°C for 30 min with (▼ = $LnSr_3Fe_3O_{10-\delta}$, x = $(Ln,Sr)FeO_3$, ○ = $(Ln,Sr)FeO_4$, and ? = unknown); (a) B = Fe, (b) B = Co, (c) B = Cu, and (d) B = Ni

4.3.2 TG analysis of $PrSr_{2.7}Ca_{0.3}Fe_{2.5}B_{0.5}O_{10-\delta}$

The weight losses of the $PrSr_{2.7}Ca_{0.3}Fe_{2.5}B_{0.5}O_{10-\delta}$ (B = Fe, Co, and Cu) samples were carried out in air at 25-800 °C as presented in Figure 4-26. All samples showed a similar trend of thermogram in the variation of weight decreasing with the increasing of temperature which was humidity loss, surface oxygen loss, and bulk oxygen loss at the temperature of 100-200 °C, 200-400 °C, and above 400 °C, respectively. The substitution of Cu for Fe provided the higher weight loss but the substitution of Co for Fe gave the reduction in weight loss, compared to $PrSr_{2.7}Ca_{0.3}Fe_3O_{10-\delta}$. This result was because the unit cell of Co substitution had a stronger interaction between the metal-O bonds thus the oxygen in the structure was maintained.

For the Cu substituted sample, a rapid increasing of weight loss was observed compared to other samples, which could be caused by the distortion of the RP structure and the loss of oxygen by the charge compensation in $PrSr_{2.7}Ca_{0.3}Fe_{2.5}Cu_{0.5}O_{10-\delta}$ due to the presence of Co^{2+}.

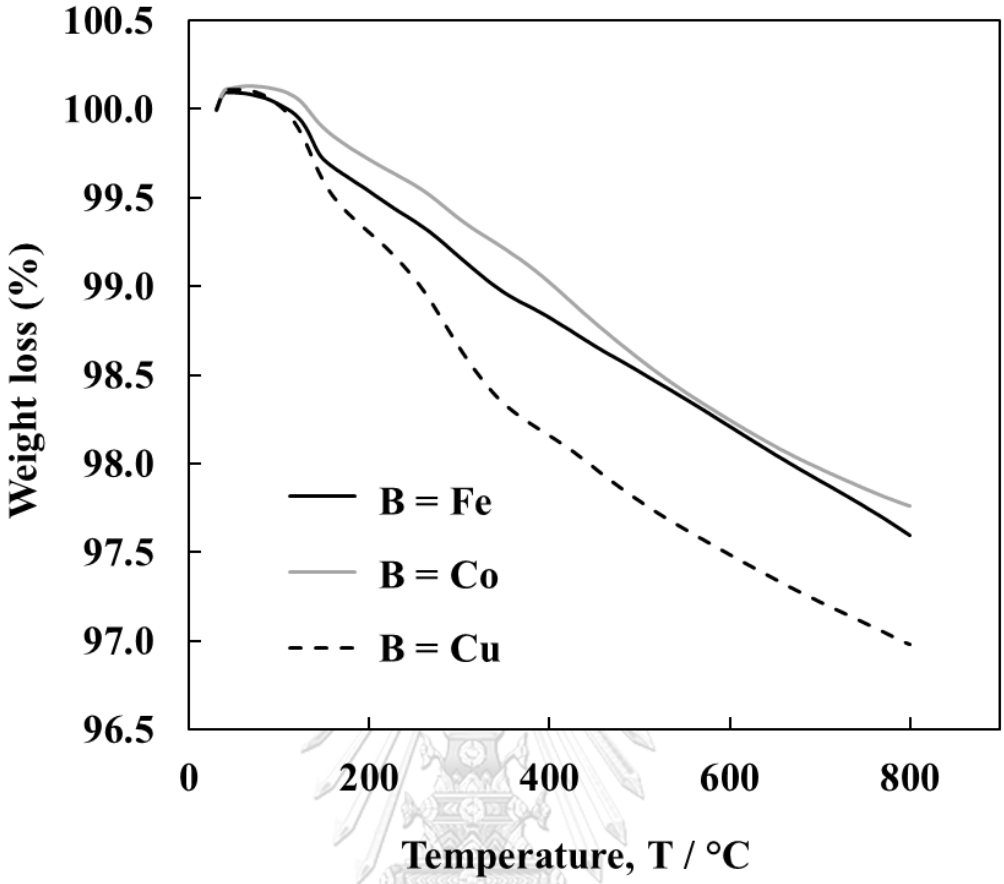

Figure 4-26 TGA plots of the $PrSr_{2.7}Ca_{0.3}Fe_{2.5}B_{0.5}O_{10-\delta}$ (B = Fe, Co, and Cu) samples measured in air at the temperature range of 25-800 °C.

4.3.3 Thermal expansion behavior $PrSr_{2.7}Ca_{0.3}Fe_{2.5}B_{0.5}O_{10-\delta}$

Figure 4-27 exhibited the thermal expansion behaviors of the $PrSr_{2.7}Ca_{0.3}Fe_{2.5}B_{0.5}O_{10-\delta}$ (B = Fe, Co, and Cu) specimens operated at 25-800 °C in air. All samples provided a linear degree of thermal expansion ($\Delta L/L_0$) at a temperature lower than 400 °C, indicating the oxygen loss was negligible at low temperature. However, the non-linear slopes were increased at higher temperatures (T>400 °C). Table 4-13 showed the average TEC values calculated at two different temperature ranges, 25–400 °C and 400–800 °C. With Co substitution, at a temperature below 400 °C, the TEC value was not significantly different, compared to the Co-free sample. While at high temperature, the TEC value was drastically increased compared to others because Co^{3+} ions changed the spin state from low spin ($t_{2g}^6eg^0$) to high spin ($t_{2g}^4eg^2$) and the ionic radius of low spin Co^{3+} was 0.545 Å whereas that of high spin Co^{3+} was 0.61 Å. Thus, the strength of metal –O bond was reduced, as a result, the materials easily expanded at high temperature, as reported by Raccah *et al*. [134] For the Cu contained sample, $PrSr_{2.7}Ca_{0.3}Fe_{2.5}Cu_{0.5}O_{10-\delta}$ showed a large TEC value in both temperatures ranges, which could be a result of oxygen loss from the structure.

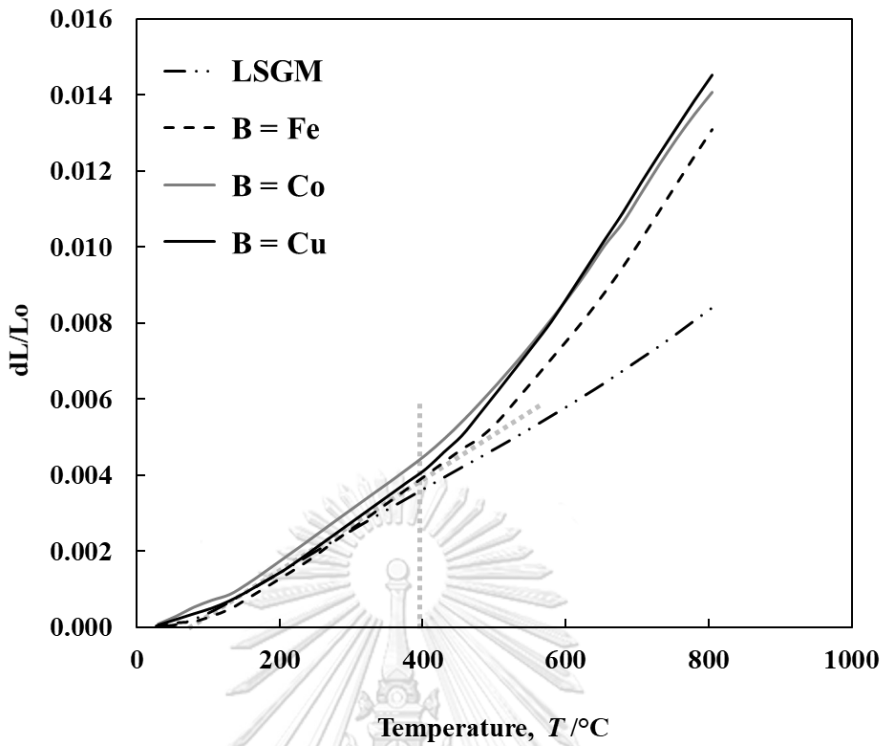

Figure 4-27 Thermal expansion ($\Delta L/L_o$) curves of $PrSr_{2.7}Ca_{0.3}Fe_{2.5}B_{0.5}O_{10-\delta}$ (B = Fe, Co, and Cu) in air at a temperature range of 25-800 °C compared to LSGM electrolyte

Table 4- 13 Average TECs of $PrSr_{2.7}Ca_{0.3}Fe_{2.5}B_{0.5}O_{10-\delta}$ (B = Fe, Co, and Cu) samples at 25–800 °C

B in $PrSr_{2.7}Ca_{0.3}Fe_{2.5}B_{0.5}O_{10-\delta}$	TEC ($10^{-6}K^{-1}$)	
	25-400 °C	400-800 °C
Fe	10.56	32.72
Cu	11.22	42.73
Co	10.15	43.41

4.3.4 Total conductivity characterization of $PrSr_{2.7}Ca_{0.3}Fe_{2.5}B_{0.5}O_{10-\delta}$

Figure 4-28 showed the total conductivity of $PrSr_{2.7}Ca_{0.3}Fe_{2.5}B_{0.5}O_{10-\delta}$ (B = Fe, Co, and Cu) samples evaluated in air at 200-800 °C. All samples provided the semiconducting behavior at low temperature (T ≤ 400 °C) but the conductivity decreased at high temperature (T > 400 °C) due to the generation of oxygen vacancies on the structure, as previously described. [85, 98, 106, 109] Compared to $PrSr_{2.7}Ca_{0.3}Fe_3O_{10-\delta}$, the total conductivity of Co-substituted sample was increased while the Cu substituted sample was decreased. This result was well-related to the oxygen loss in the structure determined by TGA analysis. $PrSr_{2.7}Ca_{0.3}Fe_{2.5}Co_{0.5}O_{10-\delta}$ had higher oxygen concentration in the structure which facilitated the electron transportation between the 2*p* orbitals of oxygen and the 3*d* orbitals of Fe and Co, similar to the works related perovskite structure, e.g. $La_{1-x}Sr_xFe_{1-y}Co_yO_3$ and $Nd_{0.7}Sr_{0.3}Fe_{1-x}Co_xO_3$. [135, 136] On the contrary, $PrSr_{2.7}Ca_{0.3}Fe_{2.5}Cu_{0.5}O_{10-\delta}$ showed a high oxygen loss, high oxygen vacancy, which could block the electron transportation and consequently decreased the conductivity.

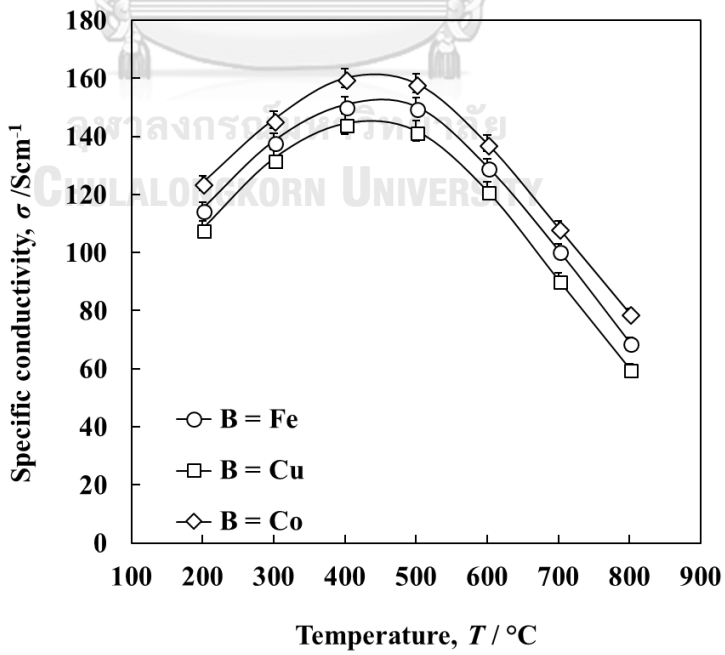

Figure 4-28 The total conductivity of $PrSr_{2.7}Ca_{0.3}Fe_{2.5}B_{0.5}O_{10-\delta}$ (B = Fe, Co and Cu) at 200-800 °C in air

4.3.5 Microstructure of $PrSr_{2.7}Ca_{0.3}Fe_{2.5}B_{0.5}O_{10-\delta}$ (B = Fe, Co and Cu)

Figure 4-29 presented the cross-section SEM image of $PrSr_{2.7}Ca_{0.3}Fe_{2.5}B_{0.5}O_{10-\delta}$ (B = Fe, Co and Cu) cathodes after fired on the LSGM electrolyte at 1000 °C in air. The dense bottom part and the porous upper part represent LSGM electrolyte and $PrSr_{2.7}Ca_{0.3}Fe_{2.5}B_{0.5}O_{10-\delta}$ cathodes, respectively. The microstructure of Cu and Co substituted samples showed larger particle size than that of $PrSr_{2.7}Ca_{0.3}Fe_3O_{10-\delta}$, which could be due to CuO and Co_3O_4 form during the material preparation. Since the metal nitrate, raw materials, was combusted at 800 °C and turned to the metal oxide before sintered into the RP n=3 strucutre at 1000°C, CuO and Co_3O_4 were formed after calcination of $Cu(NO_3)_2{\cdot}3H_2O$ and $Co(NO_3)_3{\cdot}6H_2O$. Thus, the melting point of CuO (1024 °C), which was much lower than that of FeO (~1300 °C) and Fe_3O_4 (~1600 °C promoted the sintering ability of the oxide sample and enlarged the particle size of $PrSr_{2.7}Ca_{0.3}Fe_{2.5}Cu_{0.5}O_{10-\delta}$ sample.[137-139] For Co substitution sample, Co_3O_4 could be transformed to CoO at 900 °C.[140] At this temperature, Co_3O_4 coated around the particles of metal oxides and acted as a sintering aid via liquid phase sintering.[141] This effect was found in Co substitution for NiO, reported by *Bošković et al*. [S. Bošković, M. Stevanović, Sintering of cobalt-doped nickel oxide, J. Mater. Sci. 10 (1975) 25-31] At higher temperature, these CuO and Co_3O_4 were incorporated in the $PrSr_{2.7}Ca_{0.3}Fe_{2.5}B_{0.5}O_{10-\delta}$ structure.

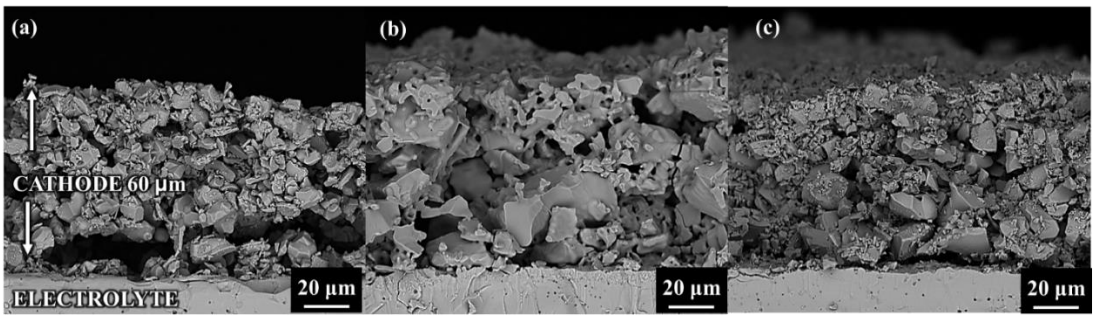

Figure 4-29 SEM images of crossed section of the $PrSr_{2.7}Ca_{0.3}Fe_{2.5}B_{0.5}O_{10-\delta}$: (a) B = Fe, (b) B = Cu, and (c) B= Co

4.3.6 Electrochemical performance of $PrSr_{2.7}Ca_{0.3}Fe_{2.5}B_{0.5}O_{10-\delta}$

4.3.6.1 Single cell performance for $PrSr_{2.7}Ca_{0.3}Fe_{2.5}B_{0.5}O_{10-\delta}$ cathodes

The electrochemical performance of the cells for $PrSr_{2.7}Ca_{0.3}Fe_{2.5}B_{0.5}O_{10-\delta}$ (B = Fe, Co, and Cu) cathodes were performed under 3% humidified H_2 fuel. The terminal voltage and power density as a function of current density were recorded in the temperature range of 600-800 °C. The slopes of activation polarization (Figure 4-30(a) (inset)) of all sample were not significantly different, suggesting that there was no difference in kinetics of the electrochemical reaction. However, the ohmic polarization of $PrSr_{2.7}Ca_{0.3}Fe_{2.5}B_{0.5}O_{10-\delta}$ (Figure 4-30(a)) was in the order from high to low values as follows, $PrSr_{2.7}Ca_{0.3}Fe_3O_{10-\delta}$ > $PrSr_{2.7}Ca_{0.3}Fe_{2.5}Cu_{0.5}O_{10-\delta}$ > $PrSr_{2.7}Ca_{0.3}Fe_{2.5}Co_{0.5}O_{10-\delta}$, indicating the electrical and ionic transportation of the cells increased by the Co and Cu substitution for Fe.

Figure 4-30(b) exhibited the power density of the cells for $PrSr_{2.7}Ca_{0.3}Fe_{2.5}B_{0.5}O_{10-\delta}$ cathodes at 800 °C. The maximum power density of $PrSr_{2.7}Ca_{0.3}Fe_3O_{10-\delta}$ was improved from 354 $mWcm^{-2}$ to 406 $mWcm^{-2}$ and 480 $mWcm^{-2}$ by Cu and Co substitution, respectively. The summarization of maximum power densities of the single cells for $PrSr_{2.7}Ca_{0.3}Fe_{2.5}B_{0.5}O_{10-\delta}$ cathodes at different operating temperature was shown in Table 4-14.

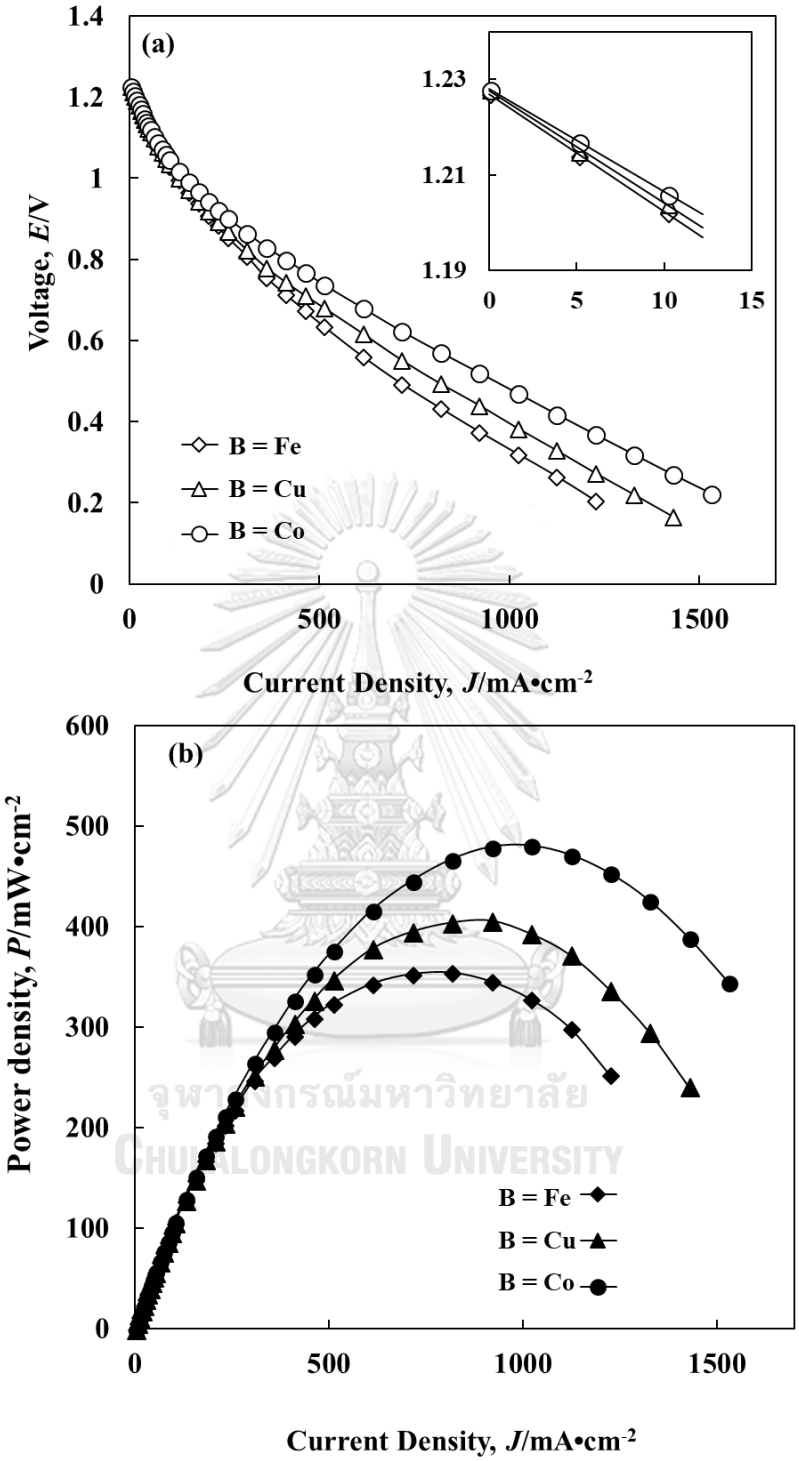

Figure 4-30 (a*)* Terminal voltage and *(*b*)* power densities as a function of current density of the cell for $PrSr_{2.7}Ca_{0.3}Fe_{2.5}B_{0.5}O_{10-\delta}$ (B = Fe, Co, and Cu) cathodes at 800 °C.

Table 4-14 The maximum power density of the single cells for the $PrSr_{2.7}Ca_{0.3}Fe_{2.5}B_{0.5}O_{10-\delta}$ (B = Fe, Co, and Cu) cathode at 600-800 °C in H_2 fuel.

B in $PrSr_{2.7}Ca_{0.3}Fe_{2.5}B_{0.5}O_{10-\delta}$	Maximum Powder density ($mW \cdot cm^{-2}$)		
	800 °C	750 °C	700 °C
Fe	354	233	88
Cu	406	256	88
Co	481	304	156

4.3.6.2 Resistance of the single cells

The impedance spectra of single cells for $PrSr_{2.7}Ca_{0.3}Fe_{2.5}B_{0.5}O_{10-\delta}$ (B = Fe, Co, and Cu) cathodes were evaluated in the temperature range of 600-800 °C. The impedance spectra of the cell for $PrSr_{2.7}Ca_{0.3}Fe_{2.5}B_{0.5}O_{10-\delta}$ cathodes at 800 °C was demonstrated in Figure 4-31. $PrSr_{2.7}Ca_{0.3}Fe_{2.5}Co_{0.5}O_{10-\delta}$ showed the lowest ASR and the highest cell performance which could be a result of the increase in conductivity of materials, as reported in the conductivity section (Figure 4-28). The higher the conductivity, the higher the number of electrons in the materials promoted the ORR. However, for $PrSr_{2.7}Ca_{0.3}Fe_{2.5}Cu_{0.5}O_{10-\delta}$, it showed lower ASR and higher cell performance compared to Cu-free sample, indicating the ORR was promoted by Cu substitution. Even the electron migration of Cu substituted sample was lower than that of Cu-free sampleas a result of low conductivity, the ORR could be promoted by the increase in oxygen migration, which correlated to the number of oxygen vacancies and the weight loss of the Cu-substituted sample. Therefore, it can be summarized that the addition of Cu and Co can promote the electrochemical performance of the cell by reducing the ASR values. The ASR value of the cell for $PrSr_{2.7}Ca_{0.3}Fe_{2.5}B_{0.5}O_{10-\delta}$ (B = Fe, Co, and Cu) cathodes at different operating temperatures was summarized in Table 4-15.

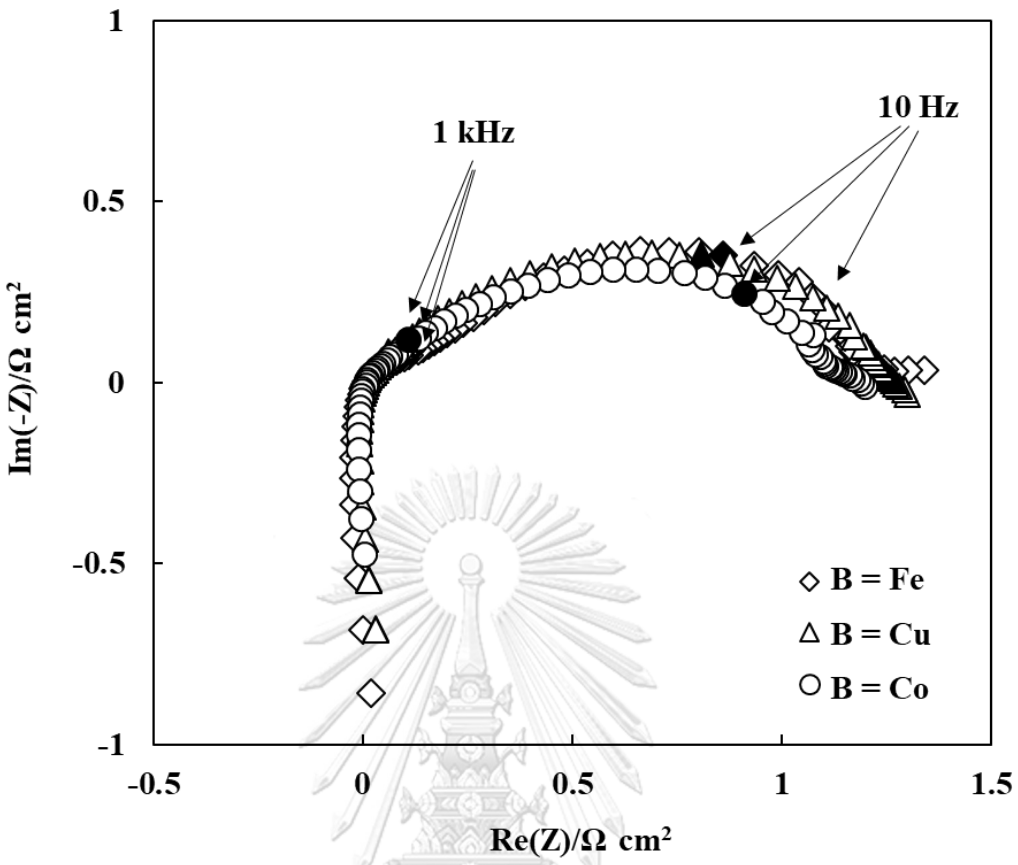

Figure 4-31 ASR of the cell for $PrSr_{2.7}Ca_{0.3}Fe_{2.5}B_{0.5}O_{10-\delta}$ (B = Fe, Co and Cu) cathodes at 800 °C

Table 4-15 ASR of the single cells for the $PrSr_{2.7}Ca_{0.3}Fe_{2.5}B_{0.5}O_{10-\delta}$ (B = Fe, Co and Cu) cathodes at 600-800 °C in H_2 fuel

B in $PrSr_{2.7}Ca_{0.3}Fe_{2.5}B_{0.5}O_{10-\delta}$	Area specific resistance, ASR (Ω cm^2)		
	800 °C	700 °C	600 °C
Fe	1.34	1.98	3.23
Cu	1.27	1.51	3.11
Co	1.18	1.20	1.74

4.4 Effect of Co concentration in $PrSr_{2.7}Ca_{0.3}Fe_{3-y}Co_yO_{10-\delta}$ (y = 0.5-1.5) Ruddlesden-Popper phases as Cathodes for Intermediate Temperature Solid Oxide Fuel Cells

4.4.1 Crystal structure and phase identification of $PrSr_{2.7}Ca_{0.3}Fe_{3-y}Co_yO_{10-\delta}$

XRD patterns of $PrSr_{2.7}Ca_{0.3}Fe_{3-y}Co_yO_{10-\delta}$ (y = 0.5-1.5) after fired at 900 °C, were illustrated in Figure 4-32. With increasing Co concentration, the tetragonal structure of RP n=3, the $(Pr,Sr,Ca)(Fe,Co)O_3$ perovskite impurity and the $(Pr,Sr,Ca)_2(Fe,Co)O_4$, RP n =1 impurity which related to $LaSr_3Fe_3O_{9.9}$ (JCPDS no. 81-1234), $La_{0.3}Sr_{0.7}FeO_3$ (JCPDS no. 82-1964) and $LaSrFeO_4$ (JCPDS no. 71-1744), respectively, were remained.The XRD patterns of Co compositon of y =0.5 to y = 1.0 (Figure 4-32(b)) were shifted to the higher angle, indicating the contraction of the unit cell due to the substitution of smaller Co^{3+} ion, as the previous discussed.[83] Moreover, the phase of $(Pr,Sr,Ca)_3(Fe,Co)_2O_4$,RP n = 2, corresponded to $Sr_3Fe_2O_7$ (JCPDS no. 82-0415), was detected in the composition of y = 1.0 while there was no trace of this phase in the composition of y = 0.5. To evaluate the amount of impurity in the structure when increased Co concentration from y = 0.5 to y = 1.0, the ratios of impurites to RP n = 3 phase were calculated as followed;

- The ratio of perovskite to RP n = 3, calculated from the peak area of 202 perovskite lattice plane and 217 RP n = 3 lattice plane due to the overlapping of the main diffraction peak, as the previous described, was increased from 1.5% to 13% with increasing Co concentration.

- The ratio RP n = 1 to RP n = 3, evaluated by the peak area of the lattice plane of 103 of RP n = 1 and 107 of RP n = 3, was also increased from 2% to 15% with increasing Co content.

- The ratio of RP n = 2 to RP n = 3 in composition y = 1.0 was calculated by 106 RP n = 2 lattice plane and 118 RP n = 3 lattice plane because the main

lattice plane 1010 of RP n = 2 was overlapped with the main lattice plane 107 of RP n = 3. Thus, the RP n = 2 impurity was around 20% in the structure.

These evidences indicated that the phase of RP n = 3 of $PrSr_{2.7}Ca_{0.3}Fe_{2.0}Co_{1.0}O_{10-\delta}$ was transformed with increasing of Co concentration. Moreover, at y = 1.5, not only the intensity of RP n = 3 of $PrSr_{2.7}Ca_{0.3}Fe_{1.5}Co_{1.5}O_{10-\delta}$ was hardly observed but the impurity phases *e.g.* Fe_3O_4, SrO and unknown phase, were also detected. These evidences indicated that the structure of $PrSr_{2.7}Ca_{0.3}Fe_{1.5}Co_{1.5}O_{10-\delta}$ was collapsed. Thus, $PrSr_{2.7}Ca_{0.3}Fe_{1.5}Co_{1.5}O_{10-\delta}$ was not further investigated. Additionally, it would be noted that $PrSr_{2.7}Ca_{0.3}Fe_{1.5}Co_{1.0}O_{10-\delta}$ had more impurity than $PrSr_{2.7}Ca_{0.3}Fe_{1.5}Co0_{.5}O_{10-\delta}$ which could affect the material properties.

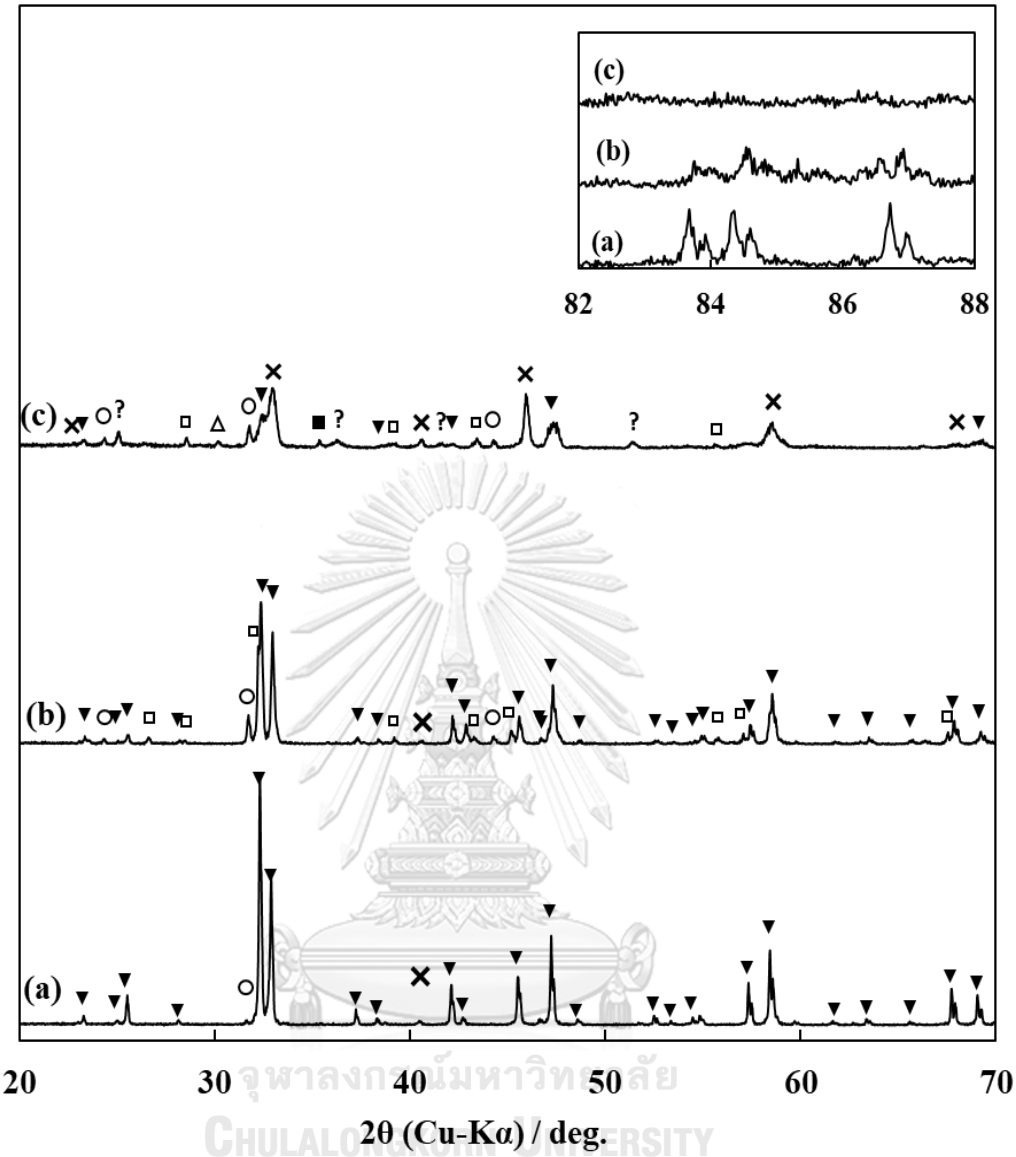

Figure 4-32 XRD pattern of $PrSr_{2.7}Ca_{0.3}Fe_{3-y}Co_yO_{10-\delta}$ *(y = 0.5-1.5)* after annealed at 900°C for 30 min with *(*▼ = $PrSr_{2.7}Ca_{0.3}Fe_{3-y}Co_yO_{10-\delta}$, **x** = perovskite, ○ = $(Pr,Sr,Ca)_2(Fe,Co)O_4$, □ = $(Pr,Sr,Ca)_3(Fe,Co)_2O_7$, △ = Fe_3O_4, ■ = SrO, and **?** = unknown*)*; *(a)* y = 0.5, *(b)* y = 1.0, and *(c)* y =1.5.

4.4.2 TG analysis $PrSr_{2.7}Ca_{0.3}Fe_{3-y}Co_yO_{10-\delta}$

The weight losses of the $PrSr_{2.7}Ca_{0.3}Fe_{3-y}Co_yO_{10-\delta}$ (y = 0.5, and 1.0) samples were carried out in air at 25-800 °C as presented in Figure 4-33. With increasing of Co concentration, the weight loss was decreased. This result was possibly because increasing Co content in the materials increased the bond strength between the metal-O bonds, as a result, the unit cell was contracted and then reduced of the oxygen loss in the structure. Even the composition of y = 1.0 contained the impurity phases, such as perovskite and RP n = 1 and 2, the perovskite was reported to have larger weight loss than the RP phase. Demont *et al*. investigated the oxygen loss of perovskite, $La_{0.6}Sr_{0.4}FeO_3$, and $La_{0.6}Sr_{0.4}CoO_3$, and RP $LaSrFeO_4$ and $LaSrCoO_4$, in Ar atmosphere and found that the perovskite structures provided higher weight loss than the RP structures because the oxidation state of metal at *B*-site in perovskite was greater than RP structure. [124] Amow *et al*. compared the oxygen loss of $La_{n+1}Ni_nO_{3n+1}$ RP structure with n = 1, 2, and 3 in air, and found that oxygen loss of RP n = 3 was larger than that of n = 1 and 2. [19] Thus, as our result, it was possibly concluded that the impurity phases was not significantly affected the oxygen loss in the $PrSr_{2.7}Ca_{0.3}Fe_{2.0}Co_{1.0}O_{10-\delta}$ structure.

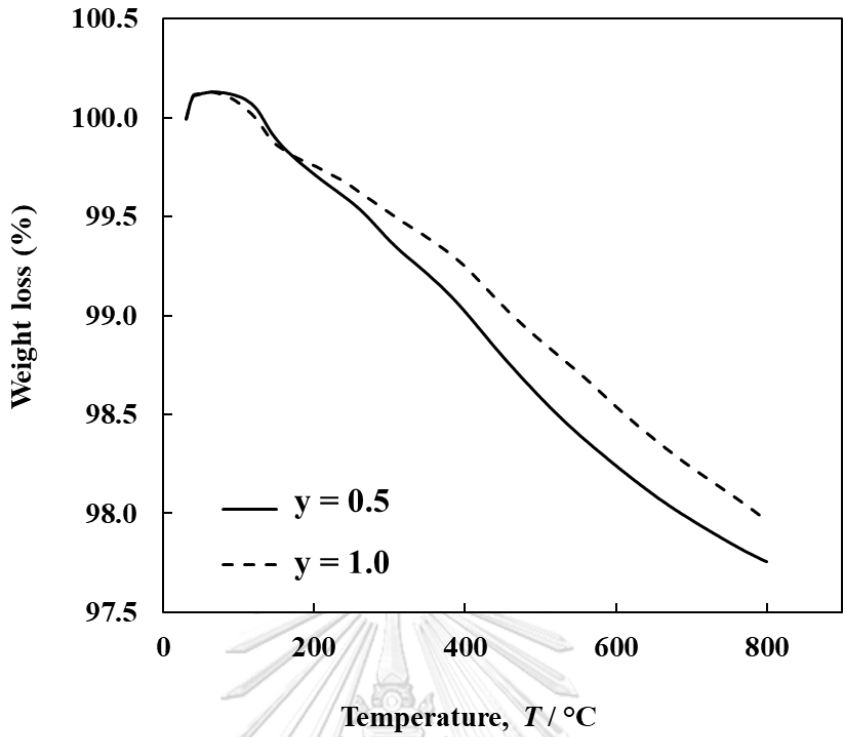

Figure 4-33 TGA plots of the $PrSr_{2.7}Ca_{0.3}Fe_{3-y}Co_yO_{10-\delta}$ *(*y = 0.5, and 1.0*)* samples measured in air at 25-800 °C

4.4.3 Thermal expansion behavior $PrSr_{2.7}Ca_{0.3}Fe_{3-y}Co_yO_{10-\delta}$

Figure 4-34 exhibited the thermal expansion behaviors of the $PrSr_{2.7}Ca_{0.3}Fe_{3-y}Co_yO_{10-\delta}$ (y = 0.5, and 1.0) specimens observed at 25-800 °C in air. Both samples showed a linear degree of thermal expansion ($\Delta L/L_0$) at temperature lower than 400 °C and non-linear behavior at high temperature. The TEC value was increased with increasing of Co content because increasing of Co content increased the number of Co that changed the spin state from low spin to high spin. The change in spin state played role in the expansion of Co-doped materials as reported by Kim *et al*.[142] In addition, the large expansion of $PrSr_{2.7}Ca_{0.3}Fe_{12.0}Co_{1.0}O_{10-\delta}$ might be caused by the expansion of impurities in the materials. However, Amow *et al*. reported that the TEC of was increased with $La_{n+1}Ni_nO_{3n+1}$ RP structure was increased with decreased the number of perovskite layer. [19] Thus, it possibly implied that the impurity phases had not significantly influenced the TEC of $PrSr_{2.7}Ca_{0.3}Fe_{3-y}Co_yO_{10-\delta}$ samples. Table 4-16

showed the calculated average TEC values at two different temperature ranges, 25–400 °C and 400–800 °C.

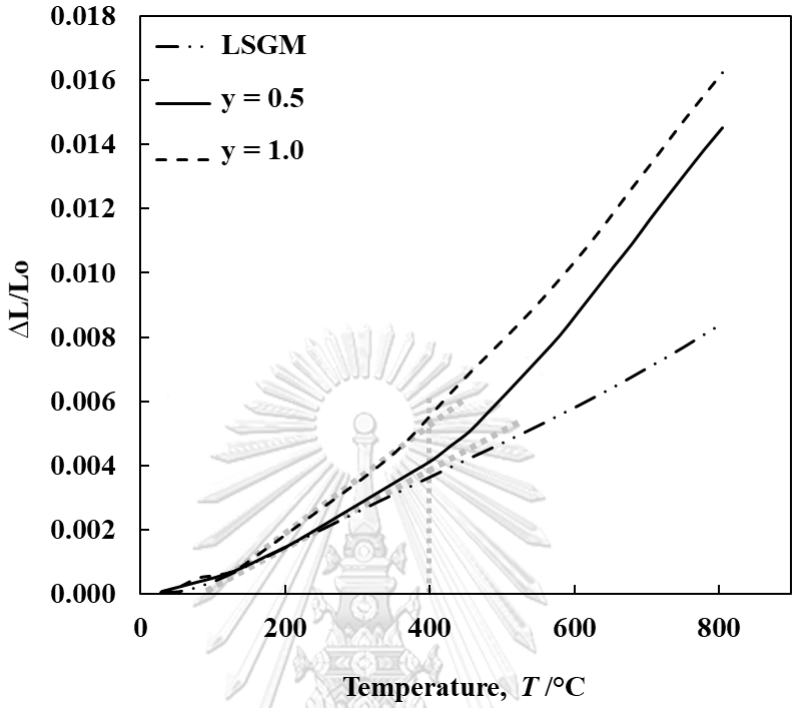

Figure 4-34 Thermal expansion *(ΔL/L$_o$)* curves of $PrSr_{2.7}Ca_{0.3}Fe_{3-y}Co_yO_{10-\delta}$ *(*y = 0.5, and 1.0*)* in air with a temperature range of 25-800 °C compared to LSGM electrolyte

Table 4-16 Average TECs values of $PrSr_{2.7}Ca_{0.3}Fe_{3-y}Co_yO_{10-\delta}$ *(*y = 0.5, and 1.0*)* samples recorded in air at 25-800 °C

y in $PrSr_{2.7}Ca_{0.3}Fe_{3-y}Co_yO_{10-\delta}$	TEC ($10^{-6}K^{-1}$)	
	25-400 °C	400-800 °C
0.5	10.15	43.41
1.0	12.56	44.33

4.4.4 Total conductivity characterization of $PrSr_{2.7}Ca_{0.3}Fe_{3-y}Co_yO_{10-\delta}$

Figure 4-35 exhibited the total conductivity of $PrSr_{2.7}Ca_{0.3}Fe_{3-y}Co_yO_{10-\delta}$ (y = 0.5, and 1.0) samples evaluated in air at 200-800 °C. All samples provided the semiconducting behavior at a temperature below 400 °C but the conductivity decreased at a temperature above 400 °C due to the generation of the oxygen vacancies on the structure, as previously described. [85, 98, 106, 109] The total conductivity increased with the increase in Co concentration, indicating the increase in electronic conductivity which facilitates the electron migration. In addition, increasing of Co content reduced the weight loss, which was presumably the loss of oxygen, in the materials. The lower the number of oxygen loss in the structure, the more electron facilitated between the 2*p* orbitals of oxygen and the 3*d* orbitals of Fe and Co. This result was also in similar trend with other Co-doped materials such as perovskites, $La_{1-x}Sr_xFe_{1-y}Co_yO_3$ and $Nd_{0.7}Sr_{0.3}Fe_{1-x}Co_xO_3$. [135, 136] Besides, the enhancein conductivity of $PrSr_{2.7}Ca_{0.3}Fe_{12.0}Co_{1.0}O_{10-\delta}$ might be influenced by the conductivity of impurities in the materials. However, Velinov *et al.* reported that the conductivity of $(LaSr)_{n+1}Fe_nO_{3n+1}$ RP structure can be enhanced by increasing the number of perovskite layer (n).[84] Thus, it suggested that the impurity of RP n = 1 and 2 had not significantly affected the conductivity of $PrSr_{2.7}Ca_{0.3}Fe_{12.0}Co_{1.0}O_{10-\delta}$. On the other hand, Chiu et al. reported that $LaNiO_3$ provided a higher conductivity than La_2NiO_4. [143] Thus, the perovskite impurity phase might enhance the conductivity of $PrSr_{2.7}Ca_{0.3}Fe_{12.0}Co_{1.0}O_{10-\delta}$.

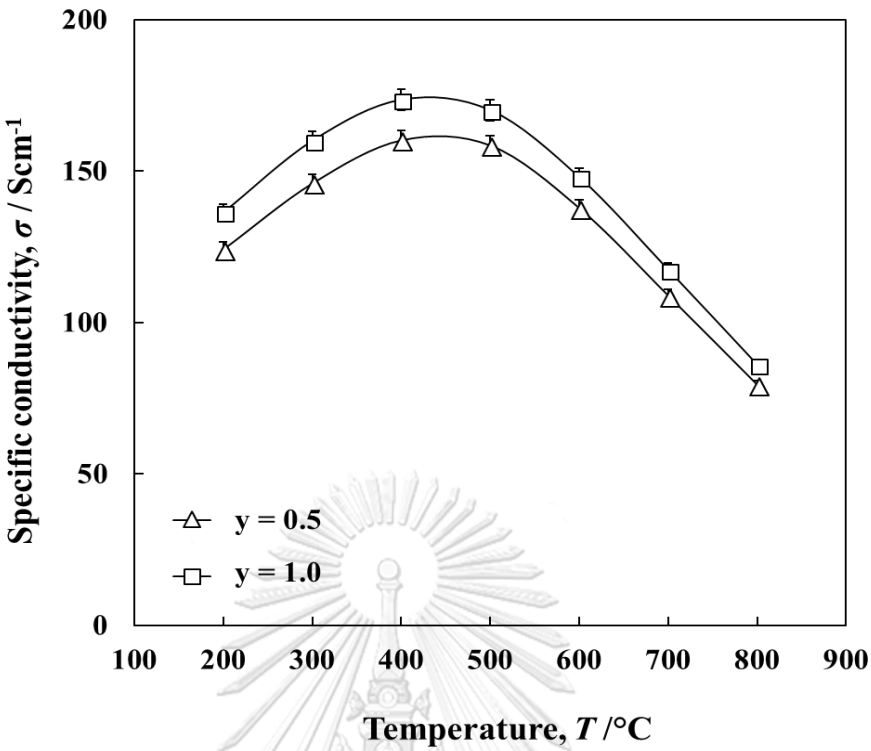

Figure 4-35 The total conductivity of $PrSr_{2.7}Ca_{0.3}Fe_{3-y}Co_yO_{10-\delta}$ *(*y = 0.5, and 1.0*)* at 200-800 °C in air

4.4.5 Microstructure of $PrSr_{2.7}Ca_{0.3}Fe_{3-y}Co_yO_{10-\delta}$ (y = 0.5, and 1.0)

Figure 4-36 presented the cross-section SEM image of $PrSr_{2.7}Ca_{0.3}Fe_{3-y}Co_yO_{10-\delta}$ (y = 0.5, and 1.0) cathodes after fired on the LSGM electrolyte at 1000 °C in air. Notice at the porous area of $PrSr_{2.7}Ca_{0.3}Fe_{3-y}Co_yO_{10-\delta}$ cathodes, the size of particles was enlarged from 8-15 μm to 15-20 μm with increasing Co concentration from y = 0.5 to y = 1.0. This result was caused by the transformation of Co_3O_4 to CoO at 900 °C, which Co_3O_4 acted as sintering aids and provided larger particles, as previous described. [140] With increasing of Co concentration, the sintering ability on the sample was increased.

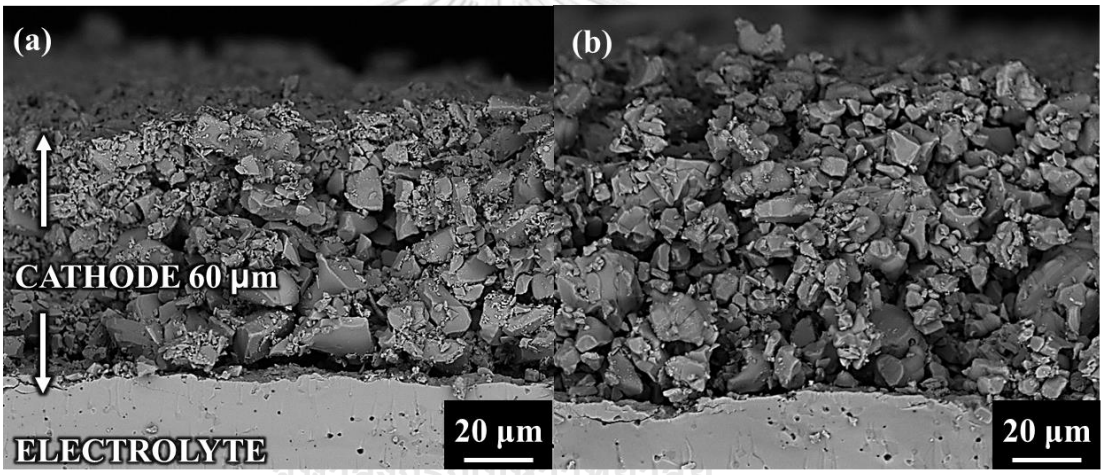

Figure 4-36 SEM images of crossed section of the $PrSr_{2.7}Ca_{0.3}Fe_{3-y}Co_yO_{10-\delta}$ cathodes; *(a)* y = 0.5, and *(b)* y = 1.0.

4.4.6 Electrochemical performance of $PrSr_{2.7}Ca_{0.3}Fe_{3-y}Co_yO_{10-\delta}$

4.4.6.1 Single cell performance for $PrSr_{2.7}Ca_{0.3}Fe_{3-y}Co_yO_{10-\delta}$ cathodes

The electrochemical performance of the cells for $PrSr_{2.7}Ca_{0.3}Fe_{3-y}Co_yO_{10-\delta}$ (y = 0.5, and 1.0) cathodes were operated with 3% humidified H_2 fuel. The terminal voltage and power density were recorded as a function of current in the temperature range of 600-800 °C. At 800 °C, the slopes of activation polarization (Figure 4-37(a) (inset)) of both cells were not significantly different, suggesting there was no difference in kinetics of the electrochemical reaction. However, the slope ohmic polarization range was increased with increasing of Co content, indicating the electrical and ionic transportation of the cells increased.

The power density of the cells at 800 °C, Figure 4-37(b), slightly decreased from 481 $mWcm^{-2}$ to 451 $mWcm^{-2}$ by increasing Co concentration from y = 0.5 to y = 1.0. The summarization of maximum power densities of the single cells for $PrSr_{2.7}Ca_{0.3}Fe_{2.5}B_{0.5}O_{10-\delta}$ cathodes at different operating temperature was shown in Table 4-17.

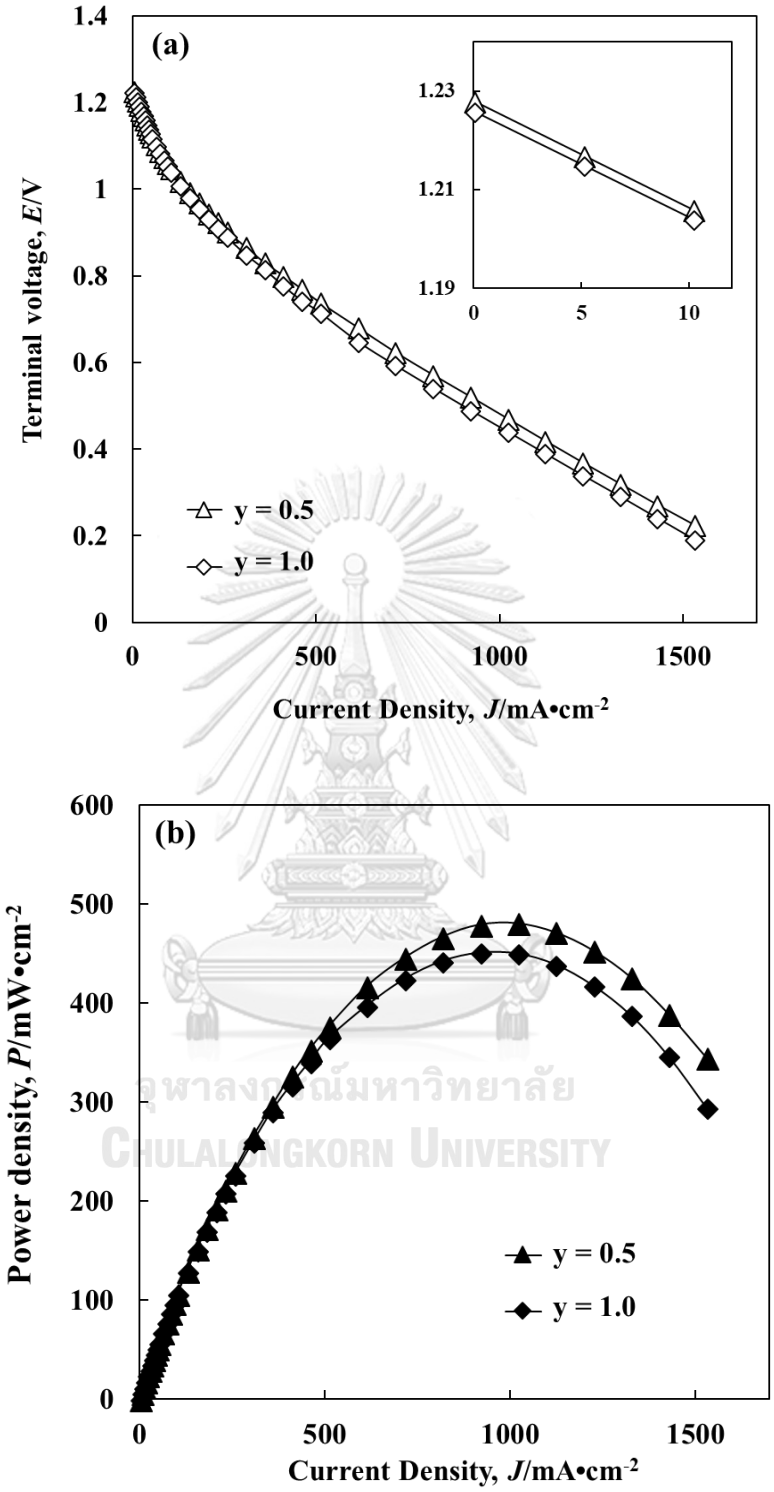

Figure 4-37 *(a)* Terminal voltage and *(b)* power density as a function of current density of the cell for $PrSr_{2.7}Ca_{0.3}Fe_{3-y}Co_yO_{10-\delta}$ *(y* = 0.5, and 1.0*)* cathodes at 800 °C.

Table 4-17 The maximum power density of the single cells for the $PrSr_{2.7}Ca_{0.3}Fe_{3-y}Co_yO_{10-\delta}$ *(y = 0.5, and 1.0)* cathodes at the temperature range of 600-800 °C in H_2 fuel.

y in $PrSr_{2.7}Ca_{0.3}Fe_{3-y}Co_yO_{10-\delta}$	Maximum Powder density ($mW \cdot cm^{-2}$)		
	800 °C	700 °C	600 °C
0.5	481	304	156
1.0	451	273	113

4.4.6.2 Resistance of the single cells for $PrSr_{2.7}Ca_{0.3}Fe_{3-y}Co_yO_{10-\delta}$ cathodes

The impedance spectra of single cells for $PrSr_{2.7}Ca_{0.3}Fe_{3-y}Co_yO_{10-\delta}$ (y = 0.5, and 1.0) cathodes were evaluated at 600-800 °C. At 800 °C (Figure 4-38), the ASR was slightly increased with the increasing of Co concentration, indicating the resistance of the cell was increased. This result could be related to the low oxygen vacancy in Co concentration y = 1.0, compared to that of y = 0.5. Since the ORR required the oxygen vacancy to migrate oxide ion, the low oxygen vacancy in $PrSr_{2.7}Ca_{0.3}Fe_{2.0}Co_{1.0}O_{10-\delta}$ obstructed the oxide ion migration, retarded the ORR, and increased ASR. The summarization of ASR values of the cells for $PrSr_{2.7}Ca_{0.3}Fe_{3-y}Co_yO_{10-\delta}$ (y = 0.5, and 1.0) cathodes at different operating temperatures was shown in Table 4-18.

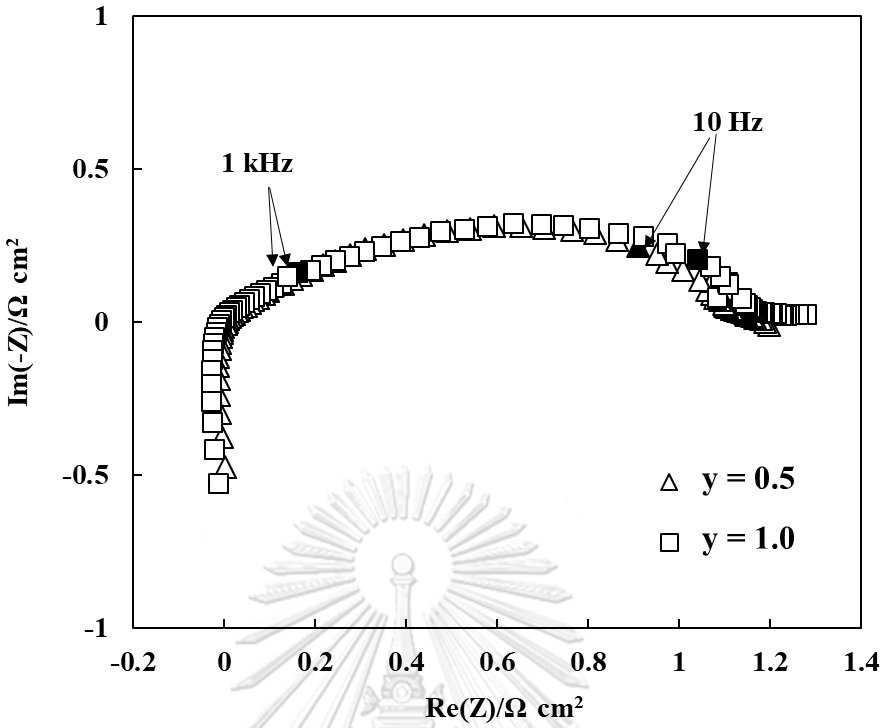

Figure 4-38 ASR of the cell for $PrSr_{2.7}Ca_{0.3}Fe_{3-y}Co_yO_{10-\delta}$ *(y = 0.5, and 1.0)* cathodes at 800 °C

Table 4-18 ASR of the single cells for the $PrSr_{2.7}Ca_{0.3}Fe_{3-y}Co_yO_{10-\delta}$ *(y = 0.5, and 1.0)* cathodes at 600-800 °C in H_2 fuel

y in $PrSr_{2.7}Ca_{0.3}Fe_{3-y}Co_yO_{10-\delta}$	Area specific resistance, ASR (Ω cm^2)		
	800 °C	700 °C	600 °C
0.5	1.18	1.20	1.74
1.0	1.23	1.37	2.41

CHAPTER V
CONCLUSION

In this work, a development of new cathode in H_2-fuel SOFC was reported to enhance the electrochemical performance of $LaSr_3Fe_3O_{10-\delta}$, various concentration of Ca was substituted for Sr in the $LaSr_3Fe_3O_{10-\delta}$ structure as $LaSr_{3-x}Ca_xFe_3O_{10-\delta}$ with x = 0-1.5. The electrochemical performance of single cell using $LaSr_{3-x}Ca_xFe_3O_{10-\delta}$ cathode was improved to approximately 32% in $LaSr_{2.7}Ca_{0.3}Fe_3O_{10-\delta}$ and $LaSr_{2.5}Ca_{0.5}Fe_3O_{10-\delta}$ at 800 °C. At low concentration of Ca substitution for Fe (x = 0-0.3), the power density of cell using $LaSr_3Fe_3O_{10-\delta}$ cathode was promoted while the ASR was reduced. The conductivity was enhanced by small Ca^{2+} substitution that shortened metal-O bond length, promoted the bond interaction, maintained oxygen in the structure, and facilitated the electron transportation in the structure to promote the ORR. At higher concentration of Ca (x = 0.5), the electrochemical performance and the ASR were not significantly different from at x=0.3 because $LaSr_{2.5}Ca_{0.5}Fe_3O_{10-\delta}$ has high content of oxygen vacancy in the structure. The oxygen vacancy facilitated the oxide ion migration in $LaSr_{2.5}Ca_{0.5}Fe_3O_{10-\delta}$ and consequently promoted the ORR and reduced ASR. In addition, the high Ca^{2+} substitution also influenced the contraction and distortion of the unit cell, the phase transformation, and the weight loss relating to the oxygen vacancy in the structure. On the contrary, the microstructure of $LaSr_{3-x}Ca_xFe_3O_{10-\delta}$ had not affected by the Ca^{2+} substitution.

With Pr and Sm substitution for Sr in $LaSr_{2.7}Ca_{0.3}Fe_3O_{10-\delta}$, the electrochemical performance of Pr-doped cell was improved with the reduction on ASR due to the increase in oxygen diffusivity via oxygen vacancy in the structure and the decreasing of Fe reduction. For Sm substituted cell, the electrochemical performance was increased with the increasing of ASR because the conductivity of Sm-doped material was poor by a large number of oxygen vacancies. Even the oxygen vacancies facilitated the oxide ion migration, too high concentration of oxygen vacancies in the structure could obstruct the electron transportation reduced ORR. The TEC study showed the increase

in TEC value from Ln = La to Sm which could relate to the increase in oxygen loss in the structure and the distortion of the unit cell as the ionic size of Ln^{3+} ions decreased.

The effect of Ni, Co, and Cu substitution for Fe in $PrSr_{2.7}Ca_{0.3}Fe_{2.5}M_{0.5}O_{10-\delta}$ showed the shrinkage of the unit cell due to the small ionic size of Co^{3+} and $Cu^{2+/3+}$ while the unit cell of Ni substituted material expanded due to the mixed oxidation state of $Ni^{2+/3+}$ and the unknown impurity phase. The electrochemical performance of the cell for $PrSr_{2.7}Ca_{0.3}Fe_{2.5}M_{0.5}O_{10-\delta}$ cathodes was improved with the reducing in ASR by the Co and Cu substitution because Co substitution provided high conductivity in the materials and Cu substitution stimulated weight loss which related to the oxygen vacancy in the structure. The increase in conductivity with Co substitution might be a result of the unit cell contraction that possibly increased the interaction between metal-O bonds and promoted electron transportation in the structure. While the Cu substitution improved the bulk oxygen migration by the increase in oxygen vacancy.

With increasing of Co concentration, the shrinkage of unit cell was increased due to the increasing number of the small Co^{3+} ion. However, the Ruddlesden-Popper structure was collapsed with Co concentration of y = 1.5. The electrochemical performance was decreased whereas the ASR was increased with increasing of Co concentration. Even the conductivity was promoted by high Co concentration, which possibly due to the increase in the interaction between (Fe,Co)-O by the smaller unit cell, the oxide ion migration could be obstructed by oxygen in the structure, reducing ASR. In addition, electrochemical performance had also been influenced by the particle size of materials. Increasing Co content promoted sintering aids of Co3O4 and consequently enlarged the particle size and reduced active surface area; besides, the TEC value was affected by the spin state transformation from low spin to high spin of Co.

In conclusion, to improve the electrochemical performance of $LaSr_3Fe_3O_{10-\delta}$ in H_2 fuel, the proper amount of Ca, Pr, and Co should be concerned for improving of conductivity and oxygen vacancy. In this work, $PrSr_{2.7}Ca_{0.3}Fe_{2.5}Co_{0.5}O_{10-\delta}$ provided

the highest improvement in the properties than others. Thus $PrSr_{2.7}Ca_{0.3}Fe_{2.5}Co_{0.5}O_{10-\delta}$ can be a potential alternative cathode for intermediate temperature SOFC.

REFERENCES

[1] Mearns, E. Energy, Environment and Policy [Online]. 2015. Available from: http://euanmearns.com/global-energy-trends-bp-statistical-review-2015/

[2] Gonzalez, E.R. and Srinivasan, S. Electrochemistry of fuel cells for transportation applications. International Journal of Hydrogen Energy 9(3) (1984): 215-218.

[3] Minh, N.Q. Ceramic Fuel-Cells. Journal of the American Ceramic Society 76(3) (1993): 563-588.

[4] Minh, N.Q. High-Temperature Fuel Cells Part 1. Chemtech 21 (1991): 6.

[5] Minh, N.Q. Solid oxide fuel cell technology—features and applications. Solid State Ionics 174(1) (2004): 271-277.

[6] Minh, N.Q. and Takahashi, T. Science and Technology of Ceramic Fuel Cells Elesevier Science BV Amsterdam. 1995, Netherlands.

[7] Tuller, H.L. and Moon, P.K. Fast ion conductors: future trends. Materials Science and Engineering: B 1(2) (1988): 171-191.

[8] Riess, I., van der Put, P.J., and Schoonman, J. Solid oxide fuel cells operating on uniform mixtures of fuel and air. Solid State Ionics 82(1) (1995): 1-4.

[9] Hens, R. Solid Electrolytes. General Principles, Characterization, Materials, Applications. Herausgegeben von P. Hagenmuller und W. van Gool. Academic Press, New York 1978. XVII, 549 S. Angewandte Chemie 91(11) (1979): 947-947.

[10] Subbarao, E.C. and Maiti, H.S. Solid electrolytes with oxygen ion conduction. Solid State Ionics 11(4) (1984): 317-338.

[11] Kawada, T., Sakai, N., Yokokawa, H., Dokiya, M., and Anzai, I. Reaction between solid oxide fuel cell materials. Solid State Ionics 50(3) (1992): 189-196.

[12] Labrincha, J.A., Frade, J.R., and Marques, F.M.B. $La_2Zr_2O_7$ formed at ceramic electrode/YSZ contacts. Journal of Materials Science 28(14) (1993): 3809-3815.

[13] Ruddlesden, S.N. and Popper, P. The compound $Sr_3Ti_2O_7$ and its structure. Acta Crystallographica 11(1) (1958): 54-55.

[14] Ruddlesden, S.N. and Popper, P. New compounds of the K_2NiF_4 type. Acta Crystallographica 10(8) (1957): 538-539.

[15] Dann, S.E., Weller, M.T., and Currie, D.B. Structure and oxygen stoichiometry in $Sr_3Fe_2O_{7-y}$, $0 \leq y \leq 1.0$. Journal of Solid State Chemistry 97(1) (1992): 179-185.

[16] Dann, S.E. and Weller, M.T. Structure and Oxygen Stoichiometry in $Sr_3Co_2O_{7-y}$ ($0.94 \leq y \leq 1.22$). Journal of Solid State Chemistry 115(2) (1995): 499-507.

[17] Navas, C., Tuller, H.L., and Loye, H.-C.z. New Mixed Conductors Based on Doped Layered Perovskites. MRS Proceedings 548 (1998): 533.

[18] Kim, J.H. and Manthiram, A. Characterization of $Sr_{2.7}Ln_{0.3}Fe_{1.4}Co_{0.6}O_7$ (Ln=La, Nd, Sm, Gd) intergrowth oxides as cathodes for solid oxide fuel cells. Solid State Ionics 180(28) (2009): 1478-1483.

[19] Amow, G., Davidson, I.J., and Skinner, S.J. A comparative study of the Ruddlesden-Popper series, $La_{n+1}Ni_nO_{3n+1}$ (n=1, 2 and 3), for solid-oxide fuel-cell cathode applications. Solid State Ionics 177(13) (2006): 1205-1210.

[20] Weng, X., Boldrin, P., Abrahams, I., Skinner, S.J., Kellici, S., and Darr, J.A. Direct syntheses of $La_{n+1}Ni_nO_{3n+1}$ phases (n=1, 2, 3 and ∞) from nanosized co-crystallites. Journal of Solid State Chemistry 181(5) (2008): 1123-1132.

[21] Grove, W.R. XXIV. On voltaic series and the combination of gases by platinum. Philosophical Magazine Series 3 14(86-87) (1839): 127-130.

[22] Burattin, P., Che, M., and Louis, C. Characterization of the Ni(II) phase formed on silica upon deposition-precipitation. Journal of Physical Chemistry B 101(36) (1997): 7060-7074.

[23] Singhal, S.C. and Kendall, K. Chapter 1 - Introduction to SOFCs. in Singhal, S.C. and Kendall, K. (eds.), High Temperature and Solid Oxide Fuel Cells, pp. 1-22. Amsterdam: Elsevier Science, 2003.

[24] Linda, C., Andreas, F.K., and Ulrich, S. Fuel Cells: Principles, Types, Fuels, and Applications. ChemPhysChem 1(4) (2000): 162-193.

[25] B Stauffer, D., H. Hirschenhofer, J., G. Klett, M., and R. Engleman, R. Fuel Cell Handbook, Fourth Edition. 1998.

[26] Stambouli, A.B. and Traversa, E. Solid oxide fuel cells (SOFCs): a review of an environmentally clean and efficient source of energy. Renewable and Sustainable Energy Reviews 6(5) (2002): 433-455.

[27] Badwal, S.P.S. Stability of solid oxide fuel cell components. Solid State Ionics 143(1) (2001): 39-46.

[28] Jiang, S.P. and Chan, S.H. A review of anode materials development in solid oxide fuel cells. Journal of Materials Science 39(14) (2004): 4405-4439.

[29] Haile, S.M. Fuel cell materials and components. Acta Materialia 51(19) (2003): 5981-6000.

[30] Haile, S.M. Fuel cell materials and components: The Golden Jubilee Issue—Selected topics in Materials Science and Engineering: Past, Present and Future, edited by S. Suresh. Acta Materialia 51(19) (2003): 5981-6000.

[31] Horita, T., et al. Materials and reaction mechanisms at anode/electrolyte interfaces for SOFCs. Solid State Ionics 177(19) (2006): 1941-1948.

[32] Taskin, A.A., Lavrov, A.N., and Ando, Y. Achieving fast oxygen diffusion in perovskites by cation ordering. Applied Physics Letters 86(9) (2005): 091910.

[33] W., S. Fuel Cells and Their Applications. KARL KORDESCH. GÜNTER SIMADER VCH Verlagsgesellschaft, Weinheim, 1996, 320 Seiten, geb., DM 248,–, ISBN 3-527-28579-2. Chemie Ingenieur Technik 69(6) (1997): 852-852.

[34] Badwal, S.P.S. Zirconia-based solid electrolytes: microstructure, stability and ionic conductivity. Solid State Ionics 52(1) (1992): 23-32.

[35] Vincenzo, E., Debora, M., D., W.E., and Enrico, T. A Soft Chemistry Route for the Synthesis of Nanostructured $Pb_2Ru_2O_{6.5}$ with a Controlled Stoichiometry. Journal of the American Ceramic Society 91(2) (2008): 437-443.

[36] Yamamoto, O. Solid oxide fuel cells: fundamental aspects and prospects. Electrochimica Acta 45(15) (2000): 2423-2435.

[37] Goedickemeier, M. and Gauckler, L. Engineering of solid oxide fuel cells with ceria-based electrolytes. Journal of the Electrochemical Society 145(2) (1998).

[38] Tuller, H. and Nowick, A. Doped ceria as a solid oxide electrolyte. Journal of the Electrochemical Society 122(2) (1975): 255-259.

[39] Virkar, A.V. Theoretical Analysis of Solid Oxide Fuel Cells with Two-Layer, Composite Electrolytes: Electrolyte Stability. Journal of the Electrochemical Society 138(5) (1991): 1481-1487.

[40] Eguchi, K., Setoguchi, T., Inoue, T., and Arai, H. Electrical properties of ceria-based oxides and their application to solid oxide fuel cells. Solid State Ionics 52(1) (1992): 165-172.

[41] Tsoga, A., Gupta, A., Naoumidis, A., and Nikolopoulos, P. Gadolinia-doped ceria and yttria stabilized zirconia interfaces: regarding their application for SOFC technology. Acta Materialia 48(18) (2000): 4709-4714.

[42] Kawada, T., et al. Resistance of (La,Sr)CoO_3/YSZ Interface with a Ceria Interlayer. ECS Proceedings Volumes 2005 (2005): 1695-1702.

[43] Singhal, S.C. and Kendall, K. High-temperature solid oxide fuel cells: fundamentals, design and applications. Elsevier, 2003.

[44] Goodenough, J.B., Manthiram, A., Paranthaman, P., and Zhen, Y.S. Fast oxide-ion conduction in intergrowth structures. Solid State Ionics 52(1) (1992): 105-109.

[45] Drennan, J., Zelizko, V., Hay, D., Ciacchi, F.T., Rajendran, S., and P. S. Badwal, S. Characterisation, conductivity and mechanical properties of the oxygen-ion conductor $La_{0.9}Sr_{0.1}Ga_{0.8}Mg_{0.2}O_{3-x}$. Journal of Materials Chemistry 7(1) (1997): 79-83.

[46] Huang, P.n. and Petric, A. Superior oxygen ion conductivity of lanthanum gallate doped with strontium and magnesium. Journal of the Electrochemical Society 143(5) (1996): 1644-1648.

[47] Ishihara, T., Matsuda, H., and Takita, Y. Effects of rare earth cations doped for La site on the oxide ionic conductivity of $LaGaO_3$-based perovskite type oxide. Solid State Ionics 79 (1995): 147-151.

[48] Wan, J., Zhu, J.H., and Goodenough, J.B. $La_{0.75}Sr_{0.25}Cr_{0.5}Mn_{0.5}O_{3-\delta}$+Cu composite anode running on H_2 and CH_4 fuels. Solid State Ionics 177(13) (2006): 1211-1217.

[49] Singhal, S.C. Advances in solid oxide fuel cell technology. Solid State Ionics 135(1) (2000): 305-313.

[50] Dokiya, M. SOFC system and technology. Solid State Ionics 152-153 (2002): 383-392.

[51] Dicks, J.L. Second Edition ed. Fuel Cell Systems Explained. 2003 John Wiley & Sons Ltd,. 2013.

[52] Ringuedé, A., Fagg, D.P., and Frade, J.R. Electrochemical behaviour and degradation of (Ni,M)/YSZ cermet electrodes (M=Co,Cu,Fe) for high temperature applications of solid electrolytes. Journal of the European Ceramic Society 24(6) (2004): 1355-1358.

[53] Lee, S.-I., Vohs, J.M., and Gorte, R.J. A study of SOFC anodes based on Cu-Ni and Cu-Co bimetallics in CeO2 YSZ. Journal of the Electrochemical Society 151(9) (2004): A1319-A1323.

[54] Ringuedé, A., Labrincha, J.A., and Frade, J.R. A combustion synthesis method to obtain alternative cermet materials for SOFC anodes. Solid State Ionics 141-142 (2001): 549-557.

[55] Ringuedé, A., Bronine, D., and Frade, J.R. $Ni_{1-x}Co_x$/YSZ cermet anodes for solid oxide fuel cells. Electrochimica Acta 48(4) (2002): 437-442.

[56] Lu, X.C. and Zhu, J.H. Ni–Fe+SDC composite as anode material for intermediate temperature solid oxide fuel cell. Journal of Power Sources 165(2) (2007): 678-684.

[57] Shi-zhong, W. and Jie, G. High Performance Ni-Fe-Lanthanum Gallate Composite Anodes for Dimethyl Ether Fuel Cells. Electrochemical and solid-state letters 9(9) (2006): A395-A398.

[58] Horita, T., Sakai, N., Kawada, T., Yokokawa, H., and Dokiya, M. Oxidation and steam reforming of CH_4 on ni and fe anodes under low humidity conditions in solid oxide fuel cells. Journal of the Electrochemical Society 143(4) (1996): 1161-1168.

[59] Skinner, S.J. and Kilner, J.A. Oxygen ion conductors. Materials Today 6(3) (2003): 30-37.

[60] Kharton, V.V., Marques, F.M.B., and Atkinson, A. Transport properties of solid oxide electrolyte ceramics: a brief review. Solid State Ionics 174(1) (2004): 135-149.

[61] International Symposium on Solid Oxide Fuel Cells Honolulu, H., 土器屋, 正., Dokiya, M., Electrochemical Society. High Temperature Materials, D., and Japan, S.S.o. Solid oxide fuel cells : (SOFC VI) : proceedings of the Sixth International Symposium. Proceedings ; v. 99-19; Proceedings (Electrochemical Society) ; v. 99-19. Pennington, NJ :: Electrochemical Society, 1999.

[62] Sun, C., Hui, R., and Roller, J. Cathode materials for solid oxide fuel cells: a review. Journal of Solid State Electrochemistry 14(7) (2010): 1125-1144.

[63] Mizusaki, J., et al. Oxygen nonstoichiometry and defect equilibrium in the perovskite-type oxides $La_{1-x}Sr_xMnO_{3+\delta}$. Solid State Ionics 129(1) (2000): 163-177.

[64] Steele, B.C.H. Survey of materials selection for ceramic fuel cells II. Cathodes and anodes. Solid State Ionics 86-88 (1996): 1223-1234.

[65] Hitoshi, T., Keiji, W., Hiroyuki, K., and Hiroshi, Y. Mechanism of Reaction between Lanthanum Manganite and Yttria-Stabilized Zirconia. Journal of the American Ceramic Society 75(2) (1992): 401-405.

[66] Brett, D.J.L., Atkinson, A., Brandon, N.P., and Skinner, S.J. Intermediate temperature solid oxide fuel cells. Chemical Society Reviews 37(8) (2008): 1568-1578.

[67] De Souza, R.A. and Kilner, J.A. Oxygen transport in $La_{1-x}Sr_xMn_{1-y}Co_yO_{3\pm\delta}$ perovskites: Part I. Oxygen tracer diffusion. Solid State Ionics 106(3) (1998): 175-187.

[68] Jiang, S.P. Issues on development of $(La,Sr)MnO_3$ cathode for solid oxide fuel cells. Journal of Power Sources 124(2) (2003): 390-402.

[69] Petric, A., Huang, P., and Tietz, F. Evaluation of La–Sr–Co–Fe–O perovskites for solid oxide fuel cells and gas separation membranes. Solid State Ionics 135(1) (2000): 719-725.

[70] Petrov, A.N., Kononchuk, O.F., Andreev, A.V., Cherepanov, V.A., and Kofstad, P. Crystal structure, electrical and magnetic properties of $La_{1-x}Sr_xCoO_{3-y}$. Solid State Ionics 80(3) (1995): 189-199.

[71] Perry Murray, E., Sever, M.J., and Barnett, S.A. Electrochemical performance of $(La,Sr)(Co,Fe)O_3$–$(Ce,Gd)O_3$ composite cathodes. Solid State Ionics 148(1) (2002): 27-34.

[72] Tai, L.W., Nasrallah, M.M., Anderson, H.U., Sparlin, D.M., and Sehlin, S.R. Structure and electrical properties of $La_{1-x}Sr_xCo_{1-y}Fe_yO_3$. Part 1. The system $La_{0.8}Sr_{0.2}Co_{1-y}Fe_yO_3$. Solid State Ionics 76(3) (1995): 259-271.

[73] Señarís-Rodríguez, M.A. and Goodenough, J.B. Magnetic and Transport Properties of the System $La_{1-x}Sr_xCoO_{3-\delta}$ ($0 < x \leq 0.50$). Journal of Solid State Chemistry 118(2) (1995): 323-336.

[74] Tai, L.W., Nasrallah, M.M., Anderson, H.U., Sparlin, D.M., and Sehlin, S.R. Structure and electrical properties of $La_{1-x}Sr_xCo_{1-y}Fe_yO_3$. Part 2. The system $La_{1-x}Sr_xCo_{0.2}Fe_{0.8}O_3$. Solid State Ionics 76(3) (1995): 273-283.

[75] Teraoka, Y., Zhang, H.M., Okamoto, K., and Yamazoe, N. Mixed ionic-electronic conductivity of $La_{1-x}Sr_xCo_{1-y}Fe_yO_{3-\delta}$ perovskite-type oxides. Materials Research Bulletin 23(1) (1988): 51-58.

[76] Liu, M., Ding, D., Blinn, K., Li, X., Nie, L., and Liu, M. Enhanced performance of LSCF cathode through surface modification. International Journal of Hydrogen Energy 37(10) (2012): 8613-8620.

[77] Manthiram, A., Prado, F., and Armstrong, T. Oxygen separation membranes based on intergrowth structures. Solid State Ionics 152-153 (2002): 647-655.

[78] Prado, F., Mogni, L., Cuello, G.J., and Caneiro, A. Neutron powder diffraction study at high temperature of the Ruddlesden–Popper phase $Sr_3Fe_2O_{6+\delta}$. Solid State Ionics 178(1) (2007): 77-82.

[79] Sayers, R., De Souza, R.A., Kilner, J.A., and Skinner, S.J. Low temperature diffusion and oxygen stoichiometry in lanthanum nickelate. Solid State Ionics 181(8) (2010): 386-391.

[80] Tsvetkov, N., Lu, Q., Chen, Y., and Yildiz, B. Surface Chemistry and Non-Stoichiometry of $Nd_2NiO_{4+\delta}$ Epitaxial Thin Films with Different Orientation and Strain. ECS Transactions 57(1) (2013): 1743-1752.

[81] Skinner, S.J. and Kilner, J.A. Oxygen diffusion and surface exchange in $La_{2-x}Sr_xNiO_{4+\delta}$. Solid State Ionics 135(1) (2000): 709-712.

[82] Bassat, J.M., Odier, P., Villesuzanne, A., Marin, C., and Pouchard, M. Anisotropic ionic transport properties in $La_2NiO_{4+\delta}$ single crystals. Solid State Ionics 167(3) (2004): 341-347.

[83] Armstrong, T., Prado, F., and Manthiram, A. Synthesis, crystal chemistry, and oxygen permeation properties of $LaSr_3Fe_{3-x}Co_xO_{10}$ ($0 \le x \le 1.5$). Solid State Ionics 140(1) (2001): 89-96.

[84] Velinov, N., Brashkova, N., and Kozhukharov, V. Synthesis, structure and conductivity of layered perovskites. Vol. 49, 2005.

[85] Lee, K. and Manthiram, A. Comparison of $Ln_{0.6}Sr_{0.4}CoO_{3-\delta}$ (Ln= La, Pr, Nd, Sm, and Gd) as cathode materials for intermediate temperature solid oxide fuel cells. Journal of the Electrochemical Society 153(4) (2006): A794-A798.

[86] Yoo, S., Choi, S., Shin, J., Liu, M., and Kim, G. Electrical properties, thermodynamic behavior, and defect analysis of $La_{n+1}Ni_nO_{3n+1+\delta}$ infiltrated into YSZ scaffolds as cathodes for intermediate-temperature SOFCs. RSC Advances 2(11) (2012): 4648-4655.

[87] Fossdal, A., Einarsrud, M.-A., and Grande, T. Phase equilibria in the pseudo-binary system SrO–Fe_2O_3. Journal of Solid State Chemistry 177(8) (2004): 2933-2942.

[88] Lee, J.Y., Swinnea, J.S., Steinfink, H., Reiff, W.M., Pei, S., and Jorgensen, J.D. The Crystal Chemistry and Physical Properties of the Triple Layer Perovskite Intergrowths $LaSr_3Fe_3O_{10-\delta}$ and $LaSr_3(Fe_{3-x}Al_x)O_{10-\delta}$. Journal of Solid State Chemistry 103(1) (1993): 1-15.

[89] Kim, J.H., Lee, K.T., Kim, Y.N., and Manthiram, A. Crystal chemistry and electrochemical properties of $Ln(Sr,Ca)_3(Fe,Co)_3O_{10}$ intergrowth oxide cathodes for solid oxide fuel cells. Journal of Materials Chemistry 21(8) (2011): 2482-2488.

[90] Tang, J.P., Dass, R.I., and Manthiram, A. Comparison of the crystal chemistry and electrical properties of $La_{2-x}A_xNiO_4$ (A = Ca, Sr, and Ba). Materials Research Bulletin 35(3) (2000): 411-424.

[91] Choi, S., Park, S., Kim, J., Lim, T.-H., Shin, J., and Kim, G. Electrochemical properties of an ordered perovskite $LaBaCo_2O_{5+\delta}$–$Ce_{0.9}Gd_{0.1}O_{2-\delta}$ composite cathode with strontium doping for intermediate-temperature solid oxide fuel cells. Electrochemistry Communications 34 (2013): 5-8.

[92] Yoo, S., Choi, S., Kim, J., Shin, J., and Kim, G. Investigation of layered perovskite type $NdBa_{1-x}Sr_xCo_2O_{5+\delta}$ (x=0, 0.25, 0.5, 0.75, and 1.0) cathodes for intermediate-temperature solid oxide fuel cells. Electrochimica Acta 100 (2013): 44-50.

[93] Wang, W., et al. The effect of calcium on the properties of $SmBa_{1-x}Ca_xCoCuO_{5+\delta}$ as a cathode material for intermediate-temperature solid oxide fuel cells. Journal of the European Ceramic Society 37(4) (2017): 1557-1562.

[94] Zheng, Y., Zhang, Y., Yu, F., Pan, Z., Yang, H., and Guo, L. Ca and Fe co-doped $SmBaCo_2O_{5+\delta}$ layered perovskite as an efficient cathode for intermediate-

temperature solid oxide fuel cells. Journal of Alloys and Compounds 696 (2017): 964-970.

[95] Kharton, V.V., et al. Oxygen Nonstoichiometry, Mixed Conductivity, and Mössbauer Spectra of $Ln_{0.5}A_{0.5}FeO_{3-\delta}$ (Ln = La–Sm, A = Sr, Ba): Effects of Cation Size. Chemistry of Materials 20(20) (2008): 6457-6467.

[96] Ferkhi, M., Khelili, S., Zerroual, L., Ringuedé, A., and Cassir, M. Synthesis, structural analysis and electrochemical performance of low-copper content $La_2Ni_{1-x}Cu_xO_{4+\delta}$ materials as new cathodes for solid oxide fuel cells. Electrochimica Acta 54(26) (2009): 6341-6346.

[97] Mogni, L.V., Prado, F.D., Cuello, G.J., and Caneiro, A. Study of the Crystal Chemistry of the n = 2 Ruddlesden–Popper Phases $Sr_3FeMO_{6+\delta}$ (M = Fe, Co, and Ni) Using in Situ High Temperature Neutron Powder Diffraction. Chemistry of Materials 21(13) (2009): 2614-2623.

[98] Lee, K.T. and Manthiram, A. $LaSr_3Fe_{3-y}Co_yO_{10-\delta}$ ($0 \leq y \leq 1.5$) Intergrowth Oxide Cathodes for Intermediate Temperature Solid Oxide Fuel Cells. Chemistry of Materials 18(6) (2006): 1621-1626.

[99] Basu, R.N., Pratihar, S.K., Saha, M., and Maiti, H.S. Preparation of Sr-substituted $LaMnO_3$ thick films as cathode for solid oxide fuel cell. Materials Letters 32(4) (1997): 217-222.

[100] Chakraborty, A., Devi, P.S., Roy, S., and Maiti, H.S. Low-temperature synthesis of ultrafine $La_{0.8}4Sr_{0.16}MnO_3$ powder by an autoignition process. Journal of Materials Research 9(4) (1994): 986-991.

[101] Almutairi, G., Ghouse, M., M. Alyousef, Y., and Alenazey, F.S. Synthesis Synthesis and Characterization of Nanocrystalline $La_{0.65}Sr_{0.3}MnO_3$ and $La_{0.8}Sr_{0.2}MnO_3$ Cathode Powders by Auto-ignition Technique for Solid Oxide Fuel Cells (SOFC). 2016.

[102] Inoishi, A., Sakai, T., Ju, Y.-W., Ida, S., and Ishihara, T. Effect of Ni/Fe ratio on the performance and stability of the Fe-air rechargeable battery using a $La_{0.9}Sr_{0.1}Ga_{0.8}Mg_{0.2}O_3$ electrolyte. International Journal of Hydrogen Energy 39(36) (2014): 21352-21357.

[103] Cherepanov, V.A., Gavrilova, L.Y., Volkova, N.E., Urusova, A.S., Aksenova, T.V., and Kiselev, E.A. Phase equilibria and thermodynamic properties of oxide systems on the basis of rare earth, alkaline earth and 3*d*-transition (Mn, Fe, Co) metals. A short overview of. 2015 2(4) (2015): 33.

[104] Shannon, R. Revised effective ionic radii and systematic studies of interatomic distances in halides and chalcogenides. Acta Crystallographica Section A 32(5) (1976): 751-767.

[105] Kharton, V., et al. Oxygen Permeability and Ionic Conductivity of Perovskite-Related $La_{0.3}Sr_{0.7}Fe(Ga)O_{3-\delta}$. Journal of The Electrochemical Society 149(4) (2002): E125-E135.

[106] Zhang, G., Li, Q., Cao, J., and Cui, M. Defect structure and electrical properties of $LaSr_3Fe_3O_{10-\delta}$. Vol. 28, 2010.

[107] Choi, S., Park, S., Shin, J., and Kim, G. The effect of calcium doping on the improvement of performance and durability in a layered perovskite cathode for intermediate-temperature solid oxide fuel cells. Journal of Materials Chemistry A 3(11) (2015): 6088-6095.

[108] Manthiram, A., Kim, J.-H., Kim, Y.N., and Lee, K.-T. Crystal chemistry and properties of mixed ionic-electronic conductors. Journal of Electroceramics 27(2) (2011): 93-107.

[109] Takahashi, H., Munakata, F., and Yamanaka, M. Ab initio study of the electronic structures in $LaCoO_3$-$SrCo_3$ systems. Physical Review B 57(24) (1998): 15211-15218.

[110] Lee, K., Bierschenk, D., and Manthiram, A. $Sr_{3-x}La_xFe_{2-y}Co_yO_{7-\delta}$ (0.3≤ x≤0.6 and 0≤y≤0.6) Intergrowth Oxide Cathodes for Intermediate Temperature Solid Oxide Fuel Cells. Journal of the Electrochemical Society 153(7) (2006): A1255-A1260.

[111] Tomkiewicz, A.C., Tamimi, M., Huq, A., and McIntosh, S. Oxygen transport pathways in Ruddlesden-Popper structured oxides revealed via in situ neutron diffraction. Journal of Materials Chemistry A 3(43) (2015): 21864-21874.

[112] Ruffa, A.R. Thermal expansion in insulating materials. Journal of Materials Science 15(9) (1980): 2258-2267.

[113] Murphy, M., et al. An ex situ study of the adsorption of calcium phosphate from solution onto TiO_2(110) and Al_2O_3(0001). Surface Science 646 (2016): 146-153.

[114] Liu, Q., Li, J., Zhou, Z., Xie, J., and Lee, J.Y. Hydrophilic Mineral Coating of Membrane Substrate for Reducing Internal Concentration Polarization (ICP) in Forward Osmosis. Scientific Reports 6 (2016): 19593.

[115] Pan, X., Wang, Z., He, B., Wang, S., Wu, X., and Xia, C. Effect of Co doping on the electrochemical properties of $Sr_2Fe_{1.5}Mo_{0.5}O_6$ electrode for solid oxide fuel cell. Vol. 38, 2013.

[116] Yamashita, T. and Hayes, P. Analysis of XPS spectra of Fe^{2+} and Fe^{3+} ions in oxide materials. Applied Surface Science 254(8) (2008): 2441-2449.

[117] Dai, N., et al. A new family of barium-doped $Sr_2Fe_{1.5}Mo_{0.5}O_{6-\delta}$ perovskites for application in intermediate temperature solid oxide fuel cells. Journal of Power Sources 268 (2014): 176-182.

[118] Zhang, K., Ge, L., Ran, R., Shao, Z., and Liu, S. Synthesis, characterization and evaluation of cation-ordered $LnBaCo_2O_{5+\delta}$ as materials of oxygen permeation membranes and cathodes of SOFCs. Acta Materialia 56(17) (2008): 4876-4889.

[119] Lim, C., et al. Influence of Ca-doping in layered perovskite $PrBaCo_2O_{5+\delta}$ on the phase transition and cathodic performance of a solid oxide fuel cell. Journal of Materials Chemistry A 4(17) (2016): 6479-6486.

[120] Ni, Q., Chen, H., Ge, L., Yu, S., and Guo, L. Investigation of $La_{1-x}Sm_{x-y}Sr_yCoO_{3-\delta}$ cathode for intermediate temperature solid oxide fuel cells. Journal of Power Sources 349 (2017): 130-137.

[121] Padmasree, K.P., Lai, K.-Y., Kaveevivitchai, W., and Manthiram, A. Effect of Ca substitution on the electrochemical properties of the Ruddlesden-Popper oxides $Sr_{3.2-x}Ca_xLn_{0.8}Fe_{1.5}Co_{1.5}O_{10-\delta}$. Vol. 374, 2018.

[122] Basbus, J.F., Caneiro, A., Suescun, L., Lamas, D.G., and Mogni, L.V. Anomalous X-ray diffraction study of Pr-substituted $BaCeO_{3-\delta}$. Acta Crystallographica Section B 71(4) (2015): 455-462.

[123] Chaianansutcharit, S., Hosoi, K., Hyodo, J., Ju, Y.W., and Ishihara, T. Ruddlesden Popper oxides of $LnSr_3Fe_3O_{10-\delta}$ (Ln = La, Pr, Nd, Sm, Eu, and Gd) as active cathodes for low temperature solid oxide fuel cells. Journal of Materials Chemistry A 3(23) (2015): 12357-12366.

[124] Demont, A., Abanades, S., and Beche, E. Investigation of Perovskite Structures as Oxygen-Exchange Redox Materials for Hydrogen Production from Thermochemical Two-Step Water-Splitting Cycles. The Journal of Physical Chemistry C 118(24) (2014): 12682-12692.

[125] Piao, J., Sun, K., Zhang, N., Chen, X., Xu, S., and Zhou, D. Preparation and characterization of $Pr_{1-x}Sr_xFeO_3$ cathode material for intermediate temperature solid oxide fuel cells. Journal of Power Sources 172(2) (2007): 633-640.

[126] Oliveira, R., Hammer, P., Guibal, E., Taulemesse, J.-M., and Garcia, O. Characterization of metal–biomass interactions in the lanthanum(III) biosorption

on Sargassum sp. using SEM/EDX, FTIR, and XPS: Preliminary studies. Vol. 239, 2014.

[127] Sunding, M.F., Hadidi, K., Diplas, S., Løvvik, O.M., Norby, T.E., and Gunnæs, A.E. XPS characterisation of in situ treated lanthanum oxide and hydroxide using tailored charge referencing and peak fitting procedures. Journal of Electron Spectroscopy and Related Phenomena 184(7) (2011): 399-409.

[128] Agarwal, M., Garg, S.K., Asokan, K., Kanjilal, D., and Kumar, P. Facile synthesis of KCl:Sm3+ nanophosphor as a new OSL dosimetric material achieved through charge transfer between the defect states. RSC Advances 7(23) (2017): 13836-13845.

[129] Crist, B. Handbook of Monochromatic XPS Spectra. Vol. 2, 1999.

[130] Pan, X., Wang, Z., He, B., Wang, S., Wu, X., and Xia, C. Effect of Co doping on the electrochemical properties of $Sr_2Fe_{1.5}Mo_{0.5}O_6$ electrode for solid oxide fuel cell. International Journal of Hydrogen Energy 38(10) (2013): 4108-4115.

[131] Zhang, X., Hao, H., and hu, X. Electronic transport properties of $YBaCo_{2-x}Cu_xO_{5+\delta}$. Vol. 403, 2008.

[132] Zhang, Y., et al. Effect of Cu doping on $YBaCo_2O_{5+\delta}$ as cathode for intermediate-temperature solid oxide fuel cells. Electrochimica Acta 134 (2014): 107-115.

[133] Chaianansutcharit, S., Ju, Y.W., Ida, S., and Ishihara, T. Ni doped $PrSr_3Fe_3O_{10-\delta}$ Ruddlesden-Popper oxide for active oxygen reduction cathode for solid oxide fuel cell. Electrochimica Acta 222 (2016): 1853-1860.

[134] Raccah, P.M. and Goodenough, J.B. First-Order Localized-Electron ⇌ Collective-Electron Transition in $LaCo_3$. Physical Review 155(3) (1967): 932-943.

[135] Matsumoto, Y., Yamada, S., Nishida, T., and Sato, E. Oxygen Evolution on $La_{1-x}Sr_xFe_{1-y}Co_yO_3$ Series Oxides. Journal of The Electrochemical Society 127(11) (1980): 2360-2364.

[136] Dasgupta, N., Krishnamoorthy, R., and Jacob, K.T. Crystal structure, thermal expansion and electrical conductivity of $Nd_{0.7}Sr_{0.3}Fe_{1-x}Co_xO_3$ ($0 \leq x \leq 0.8$). Materials Science and Engineering: B 90(3) (2002): 278-286.

[137] Fagg, D.P., Mather, G.C., and Frade, J.R. Cu-Ce0.8Gd0.2O2−δ materials as SOFC electrolyte and anode. Ionics 9(3) (2003): 214-219.

[138] Park, J.-S., Lee, J.-H., Lee, H.-W., and Kim, B.-K. Low temperature sintering of BaZrO3-based proton conductors for intermediate temperature solid oxide fuel cells. Solid State Ionics 181(3) (2010): 163-167.

[139] Nicholas, J.D. and De Jonghe, L.C. Prediction and evaluation of sintering aids for Cerium Gadolinium Oxide. Solid State Ionics 178(19) (2007): 1187-1194.

[140] Żyła, M., Smoła, G., Knapik, A., Rysz, J., Sitarz, M., and Grzesik, Z. The formation of the Co3O4 cobalt oxide within CoO substrate. Corrosion Science 112 (2016): 536-541.

[141] Silva, G.C.T. and Muccillo, E.N.S. Electrical conductivity of yttria-stabilized zirconia with cobalt addition. Solid State Ionics 180(11) (2009): 835-838.

[142] Kim, Y.N., Kim, J.H., and Manthiram, A. Effect of Fe substitution on the structure and properties of $LnBaCo_{2-x}Fe_xO_{5+\delta}$ (Ln=Nd and Gd) cathodes. Journal of Power Sources 195(19) (2010): 6411-6419.

[143] Chiu, T.-W., Lin, Y.-T., Yen, I.-F., Hsieh, H.-H., and Wang, S.-F. Properties and Performance of $La_2NiO_{4+\delta}$-$LaNiO_3$ Composite Cathodes for Intermediate-Temperature Solid Oxide Fuel Cells. Vol. 457, 2013.

[144] Li, X. and Ihara, M. Ionic conduction and power generation characteristics of Pr-doped $Ba_2In_2O_5$ for proton-conducting SOFCs. Journal of The Electrochemical Society 162(8) (2015): F927-F938.

APPENDIX

Table A-1 Ionic radius of related metal ions with their corresponding coordination numbers [104] [a] [144]

Metal	Oxidation State	Coordination Number	Ionic Radius (Å)
La	3+	6	1.032
		12	1.360
Sr	2+	6	1.180
		12	1.440
Ca	2+	6	1.000
		12	1.34
Pr	3+	6	0.990
		8	1.126
		12	1.320 [a]
	4+	6	0.850
		12	1.130[a]
Sm	2+	8	1.270
		12	1.240
	3+	6	0.958
		12	1.240
Fe	3+	6 (LS)	0.550
		6 (HS)	0.645
	4+	6	0.585
Co	2+	6 (LS)	0.650
		6 (HS)	0.745
	3+	6 (LS)	0.545
		6 (HS)	0.610
Ni	2+	6	0.690
	+3	6 (LS)	0.560
		6 (HS)	0.600

Table A-2 Relative density of $LnSr_{3-x}Ca_xFe_{3-y}B_yO_{10-\delta}$ (x = 0-0.7; Ln = La, Pr, and Sm; B = Co, Cu and y = 0-1.0)

Sample	Relative density
$LaSr_3Fe_3O_{10-\delta}$	93.60
$LaSr_{2.9}Ca_{0.1}Fe_3O_{10-\delta}$	93.51
$LaSr_{2.7}Ca_{0.3}Fe_3O_{10-\delta}$	93.17
$LaSr_{2.5}Ca_{0.5}Fe_3O_{10-\delta}$	94.58
$LaSr_{2.3}Ca_{0.7}Fe_3O_{10-\delta}$	95.64
$PrSr_{2.7}Ca_{0.3}Fe_3O_{10-\delta}$	93.13
$SmSr_{2.7}Ca_{0.3}Fe_3O_{10-\delta}$	99.14
$PrSr_{2.7}Ca_{0.3}Fe_{2.5}Cu_{0.5}O_{10-\delta}$	99.90
$PrSr_{2.7}Ca_{0.3}Fe_{2.5}Co_{0.5}O_{10-\delta}$	94.12
$PrSr_{2.7}Ca_{0.3}Fe_{2.0}Co_{1.0}O_{10-\delta}$	95.15

Table A-3 Peak area of Pr 3*d* for $PrSr_{2.7}Ca_{0.3}Fe_3O_{10-\delta}$.

Peak Designation	Peak area (a.u.)
3*d* 5/2 Pr^{3+}	23989
3*d* 5/2 Pr^{3+} spin-split doublet	7606
$3d^9f^1$ for Pr^{4+}	1410
3*d* 3/2 Pr^{3+}	12291
3*d* 3/2 Pr^{3+} spin-split doublet	2463
3*d* 3/2 Pr^{3+} satellites	2214

Table A-4 Summary of peak areas for each chemical state of Fe 2*p* in $LnSr_{2.7}Ca_{0.3}Fe_3O_{10-\delta}$ (Ln = La, Pr, and Sm).

Peak Designation	**Ln in $LnSr_{3-x}Ca_xFe_3O_{10-\delta}$**		
	La	Pr	Sm
2p3/2 Fe^{2+}	605	1183	805
2p3/2 Fe^{3+}	3250	4627	4313
2p3/2 Fe^{4+}	2514	2014	3408
2p1/2 Fe^{2+}	195	360	317
2p1/2 Fe^{3+}	966	1486	1604
2p1/2 Fe^{4+}	768	663	1291

VITA

Miss Nicharee Wongsawatgul,

A Doctor of Philosophy of Petrochemistry at Chulalongkorn University, August 2018 – present. Thesis title: “ELECTROCHEMICAL PROPERTIES OF LnSr3-xCaxFe3-yByO10 (Ln = La, Pr AND Sm; x = 0-1.0; B = Co, Ni AND Cu; y = 0-1.5) FOR INTERMEDIATE TEMPERATURE SOLID OXIDE FUEL CELLS.”

Master of Petrochemical and polymer science at Chulalongkorn University, April 2010. Thesis title: “SYNTHESIS AND CHARACTERIZATION OG ENLARGED-PORE ZEOLITE BETA CATALYST FOR HEAVY FUEL CRACKING.”

Bachelor of Science and technology (May 2009), Thammasart University